FEDERAL UNIVERSITY OF SÃO CARLOS
CENTER OF EXACT SCIENCES AND TECHNOLOGY
GRADUATE PROGRAM IN MATERIALS SCIENCE AND ENGINEERING

WELDABILITY OF AA5083-O/H111 AND NAVAL GL D36 STEEL LAP JOINTS BY FRICTION STIR WELDING

Bruna Fernanda Batistão

São Carlos - SP
2021

FEDERAL UNIVERSITY OF SÃO CARLOS
CENTER OF EXACT SCIENCES AND TECHNOLOGY
GRADUATE PROGRAM IN MATERIALS SCIENCE AND ENGINEERING

WELDABILITY OF AA5083-O/H111 AND NAVAL GL D36 STEEL LAP JOINTS BY FRICTION STIR WELDING

Bruna Fernanda Batistão

Dissertation presented to Graduate Program in Materials Science and Engineering as a partial requirement to obtain the MASTER DEGREE IN MATERIALS SCIENCE AND ENGINEERING

Supervisor: Dr. Piter Gargarella
Co-Supervisor: Dr. Nelson Guedes de Alcântara

Funding Agency: FAPESP – Process no. 2019/04613-3
CAPES – Process no. 88887.334477/2019-00

São Carlos - SP
2021

DEDICATION

To my mother Salete and my grandparents Maria and Francisco, with affection and love.

VITAE

Bachelor degree in Materials Engineering - Federal University of São Carlos (2018).

UNIVERSIDADE FEDERAL DE SÃO CARLOS

Centro de Ciências Exatas e de Tecnologia
Programa de Pós-Graduação em Ciência e Engenharia de Materiais

---

Folha de Aprovação

Defesa de Dissertação de Mestrado da candidata Bruna Fernanda Batistão, realizada em 25/01/2021.

Comissão Julgadora:

Prof. Dr. Piter Gargarella (UFSCar)

Prof. Dr. Guilherme Yuuki Koga (UFSCar)

Prof. Dr. Athos Henrique Plâine (UDESC)

O presente trabalho foi realizado com apoio da Coordenação de Aperfeiçoamento de Pessoal de Nível Superior - Brasil (CAPES) - Código de Financiamento 001.

O Relatório de Defesa assinado pelos membros da Comissão Julgadora encontra-se arquivado junto ao Programa de Pós-Graduação em Ciência e Engenharia de Materiais.

ACKNOWLEDGEMENTS

I would first like to thank my family, especially my mother and my grandparents, for the trust and support during my life, and all the prayers.

I also thank God for giving me health, strength, and knowledge to develop this work.

I wish to express my gratitude to professors Nelson Guedes de Alcântara and Piter Gargarella for the guidance, and all the conversations, suggestions, and advice that made possible the development and improvement of this work. I also thank the professors for the opportunities offered that have been allowing the development of my career.

To Luciano Bergmann and Dr. Jorge Fernandez dos Santos for the opportunity to work at the Holmholtz-Zentrum Geesthacht, and the support and supervision during this period.

To Vitor, and my friends from Geesthacht and São Carlos, especially Jéssica, Fernanda, Giovanna, Janaina, and Michele, who closely followed the development of this research, for the contributions, support, and companionship that somehow facilitated this journey.

To PPGCEM, DEMa, CCDM, and HZG, for providing excellent infrastructure for carrying the experiments related to this research, and for the technical members always friendly and helpful.

To CAPES – Coordenação de Aperfeiçoamento de Pessoal de Nível Superior for the scholarship, process no. 88887.334477/2019-00.

To FAPESP – São Paulo Research Foundation for the scholarship, process no. 2019/04613-3.

This study was financed in part by the Coordenação de Aperfeiçoamento de Pessoal de Nível Superior – Brasil (CAPES) – Finance Code 001.

ABSTRACT

Steel structures welded with aluminum alloys, which combine the low cost and high mechanical strength of steel with the weight reduction and the excellent specific properties of the aluminum alloys, are in great demand. In this context, Friction Stir Welding (FSW) stands out because it reaches lower temperatures during the welding process, reducing the thickness of the Intermetallic Compound (IMC) layers formed. Based on this, the present work proposed the application of the FSW technique to weld AA55083-O/H111 aluminum alloy to Naval GL D36 steel in lap joint configuration. For this, the influence of the welding parameters (welding speed from 5 mm/s to 15 mm/s and rotational speed from 300 rpm to 1100 rpm) on the microstructure, interface, and mechanical properties was analyzed. Joints without voids or defects were produced using low welding speeds (5 mm/s and 7 mm/s) and intermediate rotational speeds (500 rpm, 700 rpm and 900 rpm). It was observed that the decrease in the rotational speed or increase in the welding speed resulted in scattered voids and tunnel defects, a reduction in the grain size of the aluminum stir zone to a minimum of 4.04 μm (5 mm/s and 300 rpm), and, consequently, an increase of the microhardness in this zone to a maximum of 100 $HV_{0.2}$ (5 mm/s and 300 rpm). The maximum microhardness of 662 $HV_{0.2}$ was obtained in the interface, due to the presence of the FeAl and Fe_3Al IMC layers, which increased in thickness with the increasing of the welding speed and rotational speed. A combination of thinner IMC layers, higher steel hooks height, and micro interlocks in the weld interface resulted in better mechanical properties, achieving a maximum average lap shear strength load of 16.98 kN.

Keywords: Aluminum Alloys; Steel; Friction Stir Welding; Shipbuilding; Lap Joint Configuration.

RESUMO

SOLDABILIDADE DE JUNTAS DE SOBREPOSIÇÃO DE AA5083-O/H111 E AÇO NAVAL GL D36 POR SOLDAGEM POR FRICÇÃO E MISTURA

Estruturas de aço soldadas com ligas de alumínio, que combinam o baixo custo e a alta resistência mecânica do aço com a redução de peso e as excelentes propriedades específicas das ligas de alumínio, estão em grande demanda. Nesse contexto, a soldagem por fricção e mistura (FSW - *Friction Stir Welding*) se destaca por atingir menores temperaturas durante o processo de soldagem, reduzindo a espessura das camadas de compostos intermetálicos (IMC - *Intermetallic Compounds*) formadas. Baseado nisso, o presente trabalho propôs a aplicação da técnica de FSW na soldagem da liga de alumínio AA5083-O/H111 ao aço naval GL D36 com configuração de junta sobreposta. Para isso, foi analisada a influência dos parâmetros de soldagem (velocidade de soldagem de 5 mm/s a 15 mm/s e velocidade de rotação de 300 rpm a 1100 rpm) nas propriedades microestruturais, da interface e mecânicas. Juntas sem vazios ou defeitos foram produzidas usando baixas velocidades de soldagem (5 mm/s e 7 mm/s) e velocidades rotacionais intermediárias (500 rpm, 700 rpm e 900 rpm). Observou-se que a diminuição da velocidade de rotação ou aumento da velocidade de soldagem resultaram em vazios e defeitos de túnel, redução no tamanho de grão da zona de mistura do alumínio até um mínimo de 4.04 μm (5 mm/s and 300 rpm) e, consequentemente, aumento da microdureza nessa região até um máximo de 100 $HV_{0.2}$ (5 mm/s and 300 rpm). A microdureza máxima de 662 $HV_{0,2}$ foi obtida na interface, devido à presença de camadas dos IMC FeAl e Fe_3Al, que aumentaram em espessura com o aumento da velocidade de soldagem e velocidade de rotação. A combinação de camadas IMC mais finas, maior altura dos ganchos de aço e micro intertravamentos na interface da solda resultou em melhores propriedades mecânicas, atingindo uma carga de cisalhamento máxima de 16,98 kN.

Palavras-chave: Ligas de Alumínio; Aço; Soldagem por Fricção e Mistura; Construção Naval; Configuração de Junta de Sobreposição.

PUBLICATION

BATISTÃO, B.F.; BERGMANN, L.A.; GARGARELLA, P.; ALCÂNTARA, N.G.; DOS SANTOS, J.F.; KLUSEMANN, B. Characterization of Dissimilar Friction Stir Welded Lap Joints of AA5083 and GL D36 Steel. **Journal of Materials Research and Technology**, vol. 9(6), pp. 15132-15142, 2020. https://doi.org/10.1016/j.jmrt.2020.10.078.

TABLE OF CONTENTS

Pag.

APPROVAL PAGE i
ACKNOWLEDGEMENTS iii
ABSTRACT v
RESUMO vii
PUBLICATION ix
TABLE OF CONTENTS xi
LIST OF TABLES xiii
LIST OF FIGURES xv
SYMBOLS AND ABBREVIATIONS xix
1 INTRODUCTION 1
2 OBJECTIVES 3
3 LITERATURE REVIEW 5
3.1 Welding Aluminum to Steel 5
3.1.1 Intermetallic Compounds 8
3.2 Friction Stir Welding 11
3.2.1 Welding Aluminum to Steel by Friction Stir Welding 14
3.3 AA5083-O/H111 Aluminum Alloy 18
3.4 GL D36 Steel 22
4 MATERIALS AND METHODS 25
4.1 Material 25
4.2 Methods 26
4.2.1 Welding Procedure 26
4.2.2 Welds Characterization 28
4.2.2.1 Microstructural Characterization 28
4.2.2.2 Mechanical Characterization 29
4.2.2.3 Interface Characterization 30
5 RESULTS AND DISCUSSION 31
5.1 Energy Input 31
5.2 Macrostructural Characterization 34
5.3 Microstructural Characterization 42

5.4 Interface Characterization 52
5.5 Mechanical Characterization 60
5.5.1 Hardness Tests 60
5.5.2 Lap Shear Tensile Tests 67
6 CONCLUSIONS 75
7 FUTURE WORKS 77
8 REFERENCES 79
APPENDIX A 93
APPENDIX B 95
APPENDIX C 99
APPENDIX D 103
APPENDIX E 105

LIST OF TABLES

Pag.

Table 3.1 – Hardness and crystal structure of different IMCs of the Al-Fe system [35, 39, 45-49]... 10
Table 3.2 – Energy Dispersive X-Ray Spectroscopy (EDS) at points 4, 5, and 6 indicated in Figure 3.6 [13].. 16
Table 3.3 – Series of treatable and non-heat treatable aluminum alloys and their respective alloying elements. Adapted from [65]. 19
Table 4.1 – Chemical composition of AA5083 and GL D36 steel. 25
Table 4.2 – Welding parameters used to join AA5083 aluminum alloy to steel GL D36 in a lap joint configuration.. 27
Table 5.1 – Average tool torque during FSW with different rotational speeds and welding speeds. 32
Table 5.2 – Average steel hook height for welds produced using different welding speeds and rotational speeds. 40
Table 5.3 – Average grain size for welds varying welding speed and rotational speed. 47

LIST OF FIGURES

Pag.

Figure 3.1 – (a) Front subframe position in the vehicle, (b) hybrid subframe components after FSW, and (c) schematic cross-section of the welding section. Adapted from [25]. 6

Figure 3.2 – Schematic illustration of the Triplate® structural transition joint. Adapted from [28]. 7

Figure 3.3 – Equilibrium phase diagram of the Al-Fe system [38]. 9

Figure 3.4 – (a) Schematic drawing of Friction Stir Welding in butt joint configuration (design developed at the Solid-State Joining Processes Department (WMP) of the Helmholtz-Zentrum Geesthacht (HZG) research institute) [56], and (b) in lap joint configuration. Adapted from [10]. 13

Figure 3.5 – Schematic view of the different welded zones of a joint [10]. 15

Figure 3.6 – An interlaced structure in the interface of a joint produced using a welding speed of 150 mm/min, a rotational speed of 950 rpm, and an insertion depth of 3.2 mm [13]. 16

Figure 3.7 – a) SEM images of the Al-Fe interface under rotational speed of 1800 rpm, tool offset of 1.63 mm, and welding speed of 60 mm/min, and relationships between the thickness of the interlayer (t) and welding speed (v) under different tool offsets and rotational speeds in logarithm scale of b) 1200 rpm and c) 1800 rpm [15]. 17

Figure 3.8 – AA5083 base material microstructure [68]. 21

Figure 3.9 – Transverse section macrograph of two different weld zones, with lines indicating remnants of the weld line, produced using a welding speed of (a) 100 mm/min, and (b) 200 mm/min. The letters a and b in item (b) represent two regions analyzed by the author in tensile tests [69]......... 21

Figure 3.10 – Microstructure of the steel GL D36 base metal [75]. 23

Figure 4.1 – Tool attachment configuration used for welding. 25

Figure 4.2 – Gantry System – Friction Stir Welding machine. 26

Figure 4.3 – Schematic illustration of the lap joint configuration. 27

Figure 5.1 – Tool torque during the production of the joints by FSW, with tool rotational speeds from 300 rpm to 1100 rpm, and welding speeds from 5 mm/s to 15 mm/s. 32

Figure 5.2 – Average energy input during the production of the joints by FSW at a constant (a) welding speed of 5 mm/s, and (b) two different rotational speeds of 700 rpm and 900 rpm. 33

Figure 5.3 – Visual Inspection of the surface of the welds produced by FSW using a welding speed of 5 mm/s and rotational speed of (a) 700 rpm and (b) 1100 rpm.......... 35

Figure 5.4 – Macrostructure of the welds produced by FSW using welding speed and rotational speed of (a) 5 mm/s and 300 rpm, (b) 15 mm/s 700 rpm, (c) 5 mm/s and 700 rpm, and (d) 5 mm/s and 1100 rpm. 36

Figure 5.5 – Welds according to its process parameters and macrostructure features. 37

Figure 5.6 – Macrostructure of the welds produced by FSW using a welding speed of 9 mm/s and rotational speed of (a) 700 rpm, and (b) 900 rpm. 38

Figure 5.7 – Steel hook and particles present in the joints produced using welding speed and rotational speed of (a) 5 mm/s and 500 rpm, (b) 5 mm/s and 700 rpm, (c) 5 mm/s and 900 rpm, (d) 7 mm/s and 700 rpm.......... 39

Figure 5.8 – Lamellar structure with cracks inside formed at the interface of the weld 5, produced using a welding speed of 5 mm/s and rotational speed of 1100 rpm.......... 41

Figure 5.9 – Microstructure of the weld 3, produced using a welding speed of 5 mm/s and rotational speed of 700 rpm, and weld zones.......... 43

Figure 5.10 – (a) Aluminum BM and HAZ, (b) aluminum TMAZ on the RS, (c) aluminum TMAZ on the AS, and (d) aluminum SZ, in the weld 3, produced using a welding speed of 5 mm/s and rotational speed of 700 rpm.......... 44

Figure 5.11 – Transition in the microstructure from the TMAZ to the SZ on the (a) RS, and (b) AS of the weld 8 (13 mm/s and 700 rpm). 45

Figure 5.12 – Microstructure of the Al-SZ of the weld 5 (5 mm/s and 1100 rpm). 45

Figure 5.13 – Grain size variation in the Al-SZ of the welds produced using welding speed and rotational speed of (a) 5 mm/s and 300 rpm, (b) 5 mm/s and 1100 rpm, (c) 15 mm/s and 900 rpm, and (d) 5 mm/s and 900 rpm.47

Figure 5.14 – (a) Steel BM and HAZ, and (b) steel TMAZ, in the weld 3, produced using a welding speed of 5 mm/s and rotational speed of 700 rpm. 48

Figure 5.15 – Microstructure of the St-TMAZ of the welds produced using a welding speed and rotational speed of (a) 5 mm/s and 900 rpm, (b) 5 mm/s and 1100 rpm, and (c) 7 mm/s and 900 rpm. 49

Figure 5.16 – Microstructure of the St-TMAZ of the weld 13, produced using a welding speed of 13 mm/s and rotational speed of 900 rpm. 50

Figure 5.17 – Microstructure of the (a) dispersed steel particles, and (b) steel hook, at the weld interface. 51

Figure 5.18 – SEM backscattered micrograph and EDS line scan results of the interface of joints produced using welding speed and rotational speed of (a) 5 mm/s and 700 rpm, (b) 9 mm/s and 700 rpm, and (c) 9 mm/s and 900 rpm.. 53

Figure 5.19 – EDS chemical maps of the IMC layer showing the Fe, Mg, Mn, Al, Si, and C elements at the interface of the welds produced using a welding speed and rotational speed of (a) 5 mm/s and 700 rpm, (b) 9 mm/s and 700 rpm, and (c) 9 mm/s and 900 rpm. 56

Figure 5.20 – XRD pattern from the interface of the weld 3 produced using a welding speed of 5 mm/s and a rotational speed of 700 rpm. 57

Figure 5.21 – Tongue-like morphology in the interface of SEM backscattered micrograph of the weld 11 produced using a welding speed of 9 mm/s and rotational speed of 900 rpm. 58

Figure 5.22 – Micro interlocks in SEM backscattered micrographs of the interface of welds produced using welding speed and rotational speed of (a) 5 mm/s and 700 rpm, and (b) 9 mm/s and 700 rpm. 59

Figure 5.23 – Horizontal microhardness profile along the aluminum alloy part of the welds at different welding speeds and rotational speeds. 61

Figure 5.24 – Horizontal microhardness profile along the steel part of the welds at different welding speeds and rotational speeds. 63

Figure 5.25 – Vertical microhardness profile perpendicular to the interface of the welds at different welding speeds and rotational speeds. 65

Figure 5.26 – Microhardness indentation in the mixed layers in the interface of the weld 5 produced using a welding speed of 5 mm/s and rotational speed of 1100 rpm. 66

Figure 5.27 – Results of the lap shear tensile tests of welds produced by FSW using different welding speeds and rotational speeds. 68

Figure 5.28 – Average displacement to fracture of the welds at a constant (a) welding speed of 5 mm/s, and (b) two different rotational speeds. ... 69

Figure 5.29 – Samples after lap shear tensile tests produced by FSW using welding speed and rotational speed of (a) 13 mm/s and 900 rpm and (b) 5 mm/s and 700 rpm; and (c) schematic illustration of the maximum stress during the lap shear tensile tests. 70

Figure 5.30 – Average maximum lap shear load of the welds at a constant (a) welding speed of 5 mm/s, and (b) two different rotational speeds. 72

SYMBOLS AND ABBREVIATIONS

at.%	Atomic Percentage
AA	Aluminum Alloy
Al	Aluminum
AS	Advancing Side
BM	Base Material
C	Carbon
CCDM	Center for Characterization and Development of Materials
CDRX	Continuous Dynamic Recrystallization
DEMa	Department of Materials Engineering
DRV	Dynamic Recovery
EDS	Energy Dispersive X-Ray Spectroscopy
Fe	Iron
FSBW	Friction Stir Butt Welding
FSLW	Friction Stir Lap Welding
FSP	Friction Stir Processing
FSW	Friction Stir Welding
HAZ	Heat Affected Zone
HSLA	High-Strength Low-Alloy Steel
HSS	High Strength Steel
HZG	Helmholtz-Zentrum Geesthacht
IMC	Intermetallic Compound
LCE	Laboratory of Structural Characterization
Mg	Magnesium
MIG	Metal Inert Gas
Mn	Manganese
PPGCEM	Graduate Program in Materials Science and Engineering
RS	Retreating Side
SEM	Scanning Electron Microscopy
SFE	Stacking-Fault Energy
Si	Silicon

St	Steel
SZ	Stir Zone
TIG	Tungsten Inert Gas
TMAZ	Thermo-Mechanically Affected Zone
TWI	The Welding Institute
UFSCar	Federal University of São Carlos
XRD	X-Ray Diffraction
WMP	Solid-State Joining Processes Department
wt.%	Weight Percentage

1 INTRODUCTION

The transportation industry is constantly trying to reduce the fuel or energy consumption and improve the load-carrying capacity and velocity through efficiency improvements, which include the vehicle weight reduction. The weight reduction decreases the power propulsion and can be achieved through design optimization to obtain higher performance, and materials substitution, replacing steels with lighter weight materials [1-2]. For example, as one of these lighter weight materials, the average content of aluminum alloys is expected to increase around 30% in cars by 2025 compared to 2016, being that this average content per vehicle increased from 150.6 kg in 2016 to 179.2 kg in 2019, according to the European Aluminium Association [3-4].

The combination of materials such as aluminum alloys and steel in a hybrid structure, using the different properties of the component materials together, can meet both the search for lightweight, high-performance structures and the tendency to integrate more functions into each part, achieving the performance required for the product. This trend is reported in various sectors, such as automotive, aeronautics, marine application, and others [5].

In this situation, studies are being conducted on the application of aluminum to steel welding processes, which range from solid-state to fusion welding processes, such as refill friction stir spot welding, friction stir welding, diffusion welding, explosion welding, resistance spot welding, and laser welding processes [6-7].

Significant differences in mechanical and thermal properties make the bonding between aluminum and steel a challenge. For example, residual stresses and the formation of intermetallic phases by reactions in the solid-state can occur due to differences in thermal properties, which generally causes the mechanical degradation of the joint. These phases are formed by interdiffusion of the compounds and, therefore, are very dependent on time and temperature, which causes the formation of thick Intermetallic Compound (IMC) layers in joining processes with long thermal cycles, such as fusion welding. On the contrary, solid-state welding techniques generally result in reduced formation of these intermetallic phases due to the shorter times and lower temperatures reached during the welding process [7].

Among these techniques, explosion welding has been used to produce aluminum to steel joints for the shipbuilding industry, due to the capacity of the process to join big surfaces, using plates with a wide range of thickness, and with no significant changes in the microstructure of the base materials or porosity in the bond zone. During this process, the top plate is accelerated against the bottom plate through an explosion, and the plastic deformation results in mechanical joining. However, the industrial application of the explosion welding process is limited due to the problems related to the effects of the explosion and the storage of explosive materials [6, 8]. Instead, as another solid-state welding technique, Friction Stir Welding (FSW) has the advantages of using a non-consumable tool and not requiring filler material or post-processing, being environmentally friendly and cost-effective. This process has been studied and was already used in automotive production environments to join aluminum to steel [5].

Different combinations of aluminum alloys with steels are being used in the FSW studies, such as AA5083-H321 to 316L stainless steel [9], AA6181-T4 to HC340LA High-Strength Steel (HSS) [10], pure aluminum to a low carbon zinc-coated steel [11], AA6013-T4 to X5CrNi18-10 stainless steel [12], AA1061 to SUS321 stainless steel [13], AA6060-T5 to mild steel [14], and AA6061-T6 to TRIP780 steel [15]. However, the FSW of AA5083 aluminum alloy and GL D36 steel, both materials used in marine applications, was still not investigated.

In general, these studies are focused on the effects of the welding parameters (welding speed and tool rotational speed, tool positioning, and probe insertion depth) on the microstructure and joint strength [9, 11, 13-14], and there are just a few studies about the influence of the welding parameters in the formation and growth of IMC layers during the FSW process, and the influence of these layers on the mechanical properties of the joint [15-17].

2 OBJECTIVES

The main objective of this master’s project was the study of the Friction Stir Welding (FSW) technique for joining AA5083-O/H111 to Naval GL D36 steel in lap joint configuration. To achieve this objective, the effects of the welding parameters (tool rotational speed and welding speed) on the microstructure and mechanical properties of the joints were evaluated. Besides that, the influence of the welding parameters on the Intermetallic Compounds (IMC) formation and growth, and the influence of these phases on the mechanical properties of the joints was analyzed.

3 LITERATURE REVIEW

3.1 Welding Aluminum to Steel

The continuous search for the reduction of energy consumption and air pollution triggered by concerns about global warming and energy usage is pushing towards the use of new materials or combination of materials in the transport industry. To enhance fuel economy, with the consequent decrease in the exhaust emissions, the transport industry has been replacing materials with high density by materials with a higher strength-to-weight ratio and good corrosion resistance, that is, replacing the steels with materials such as plastics and aluminum alloys. This is happening because the use of lightweight materials contributes to reducing the vehicle weight without affecting the crescent safety, performance, convenience, and luxury demanded by their customers [18-19].

Although the excellent specific tensile strength, the aluminum alloys are being applied in vehicles just in those parts that do not require extreme high strength due to its costs and properties as a structural material. Because of the partial application, there is a great demand for joints of aluminum alloys with steels, such as High-Strength Steel (HSS), which have great potential in weight reduction. Various methods, such as resistance spot welding and arc welding (fusion welding), explosive welding, friction welding and diffusion bonding (solid-state bonding), brazing, self-pierce riveting (mechanical bonding) and adhesive bonding, have been proposed to join material together [20-21].

In an automotive vehicle, for example, secondary structural elements made of aluminum alloys can be joined to main structures made of steel, such as the chassis module [22]. The rear shelf made of aluminum has already been welded to the surrounding steel components using the resistance welding process in the Volkswagen Passat GTE model, making it lighter than the previous model [23]. Furthermore, in the front sub-frame of the Honda Accord 2013 model was used Friction Stir Lap Welding (FSLW) to join aluminum alloy to steel [24-25], as shown in Figure 3.1, replacing the conventional Metal Inert Gas (MIG) welding process and the mechanical coupling by rivets and bolts. As a result, the sub-frame built with the new technique was 25% (6 kg) lighter than that of the previous model with aluminum and steel joined together by bolts, and the weld strength obtained was equal to or greater than in conventional MIG welding. The process also improved the dynamic performance of the car, increasing by 20% the stiffness of the installation points in the suspension system [24-25].

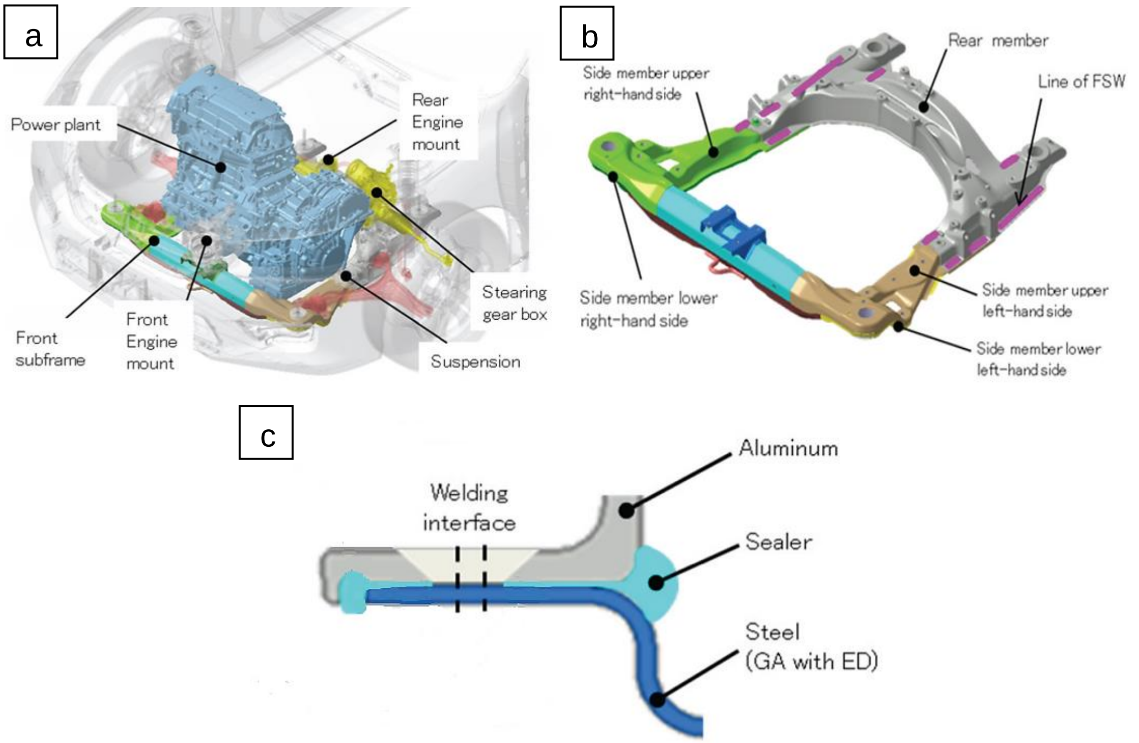
a
Power plant
Rear
Engine
mount
Stearing
gear box
Suspension
Front
subframe
Front
Engine
mount
b
Side member upper
right-hand side
Rear member
Line of FSW
Side member lower
right-hand side
Side member upper
left-hand side
Side member lower
left-hand side
c
Aluminum
Welding
interface
Sealer
Steel
(GA with ED)

Figure 3.1 – (a) Front subframe position in the vehicle, (b) hybrid subframe components after FSW, and (c) schematic cross-section of the welding section. Adapted from [25].

In the shipbuilding industry, the use of aluminum alloys over steel or composites, allows weight savings of 15-20%, due to its low density combined with high strength, toughness and corrosion resistance, and consequently, allows the improvement of speed and load-carrying capacity [26]. For the aquatic vehicles' construction is preferable the use of hulls made of steel and aluminum, being the under-water surface made of steel, and the non-submerged surface made of aluminum alloy. This structure achieves weight reduction and lowers the gravity center of the vehicles [22]. To building these structures, a pre-produced transition joint has been employed to allow welds between aluminum and steel. The transition joints are made with a base of steel, pure aluminum as an intermediate layer, and a corrosion-resistant aluminum alloy upper layer [8, 27-28], as shown in Figure 3.2. This top layer is usually composed of the 6xxx (Al-Mg-Si) and especially 5xxx (Al-Mg) aluminum alloy series, which presents the highest corrosion resistance in seawater among the aluminum alloys [29-30].

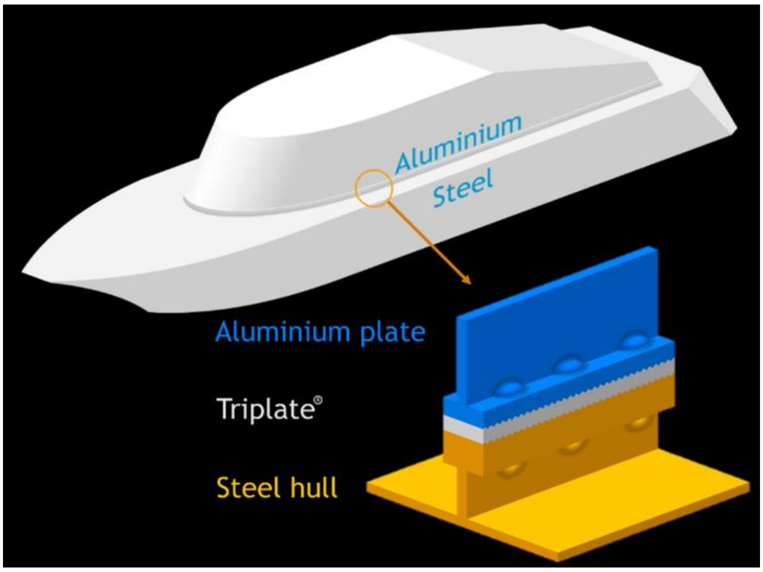

Figure 3.2 – Schematic illustration of the Triplate® structural transition joint. Adapted from [28].

Transition joints are mainly produced by the explosion welding process and can be welded to the parent materials using traditional welding processes, such as MIG, and Tungsten Inert Gas (TIG) [8, 27-28]. The main applications of these joints are to join aluminum superstructures or decks to steel decks or hulls, to fit other components, such as pillars, additional accommodations, and others [27].

The shear strength of transition joints has been studied in some works. The maximum tensile shear strength of about 90 MPa was obtained on 5 mm x 70 mm AA5083 and SS41 explosive welded joints with an AA1050 interlayer plate [31], and 720 MPa of tensile shear strength was achieved on 100 mm x 150 mm explosively welded aluminum and High-Strength Low-Alloy (HSLA) steel joints [32]. In another research, advanced high strength steel and AA6061 were joined by hybrid laser arc welding to a transition joint. The transition joint used was composed of 50.8 mm x 152.4 mm AA5456 and ASTM A516 Grade 55 steel, with an interlayer of AA1100, and was produced by explosive welding. The maximum tensile strength of 220 MPa was obtained, with the fracture occurring at the AA5456-to-AA6061 weld [33]. The interlayer is used in transition joints as resistance to diffusion, minimizing the brittle interfacial zone, and improving the weldability [31, 33].

Significant differences in the physical and metallurgical properties of steel and aluminum make the mechanical bonding between these materials a challenge. For example, differences in thermal properties, such as linear expansion, specific heat and conductivity, and in mechanical properties, such as yield strength and Poisson’s ratio, causes non-uniform heating and inhomogeneous plastic deformation, resulting in weld regions with different mechanical properties and with distortion and residual stress after welding procedure [7, 34].

Metallurgically, differences in the melting points and solubilities of Fe and Al result in the formation of brittle phases and the segregation of high and low melting point phases, making them difficult to join together, especially by conventional fusion welding. Intermetallic compound (IMC) layers are usually formed at the joint in the fusion welding processes due to extended thermal cycles (higher temperatures during longer times), and these layers are frequently considered the cause for the weld strength degradation observed in dissimilar aluminum/steel joints [7, 35-36].

3.1.1 Intermetallic Compounds

The formation of the Intermetallic Compound (IMC) layers occurs by the interdiffusion of the Al and Fe atoms across the welding interface being highly dependent on the specific time and temperature history of the welding process [7]. Because of the low solubility between Al and Fe, as seen in Figure 3.3, the IMC layers are formed, and their growth is controlled by solid-state diffusion of Fe atoms into the Al-richer IMC layer [37].

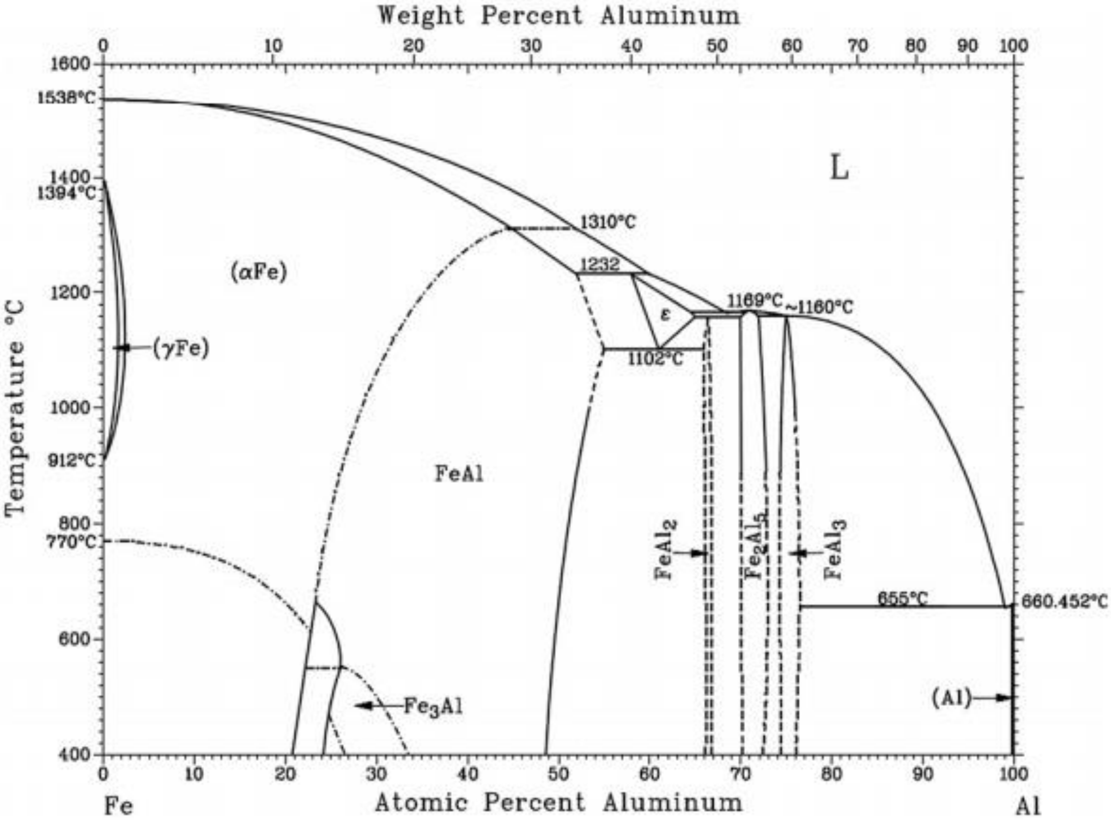

Figure 3.3 – Equilibrium phase diagram of the Al-Fe system [38].

The type and size of the IMC phase formed depend on process conditions and welding parameters, which determine the time, temperature, pressure, and chemical compositions that govern the IMC formation. From Figure 3.3, the nonstoichiometric IMCs formed during the bonding between Al and steel-based alloys can be seen, such as Fe_3Al, FeAl, $FeAl_2$, Fe_2Al_5, and $FeAl_3$. Their hardness and crystal structures are presented in Table 3.1 [39]. The Fe_3Al and FeAl are $D0_3$ (BiF_3 type), and B2 (CsCl type) ordered phases, respectively. In the stoichiometric composition, the FeAl B2-type unit cell is composed of two atoms, the Al atom occupying the center and the Fe atoms occupying the corners of the cube, and the Fe_3Al $D0_3$-type unit cell can be considered as composed of eight B2-type unit cells, with the Fe atoms occupying the corners of the cubes, but alternating Fe and Al in the center of the cubes, maximizing the distance between Al atoms [40-42]. On the other hand, the triclinic $FeAl_2$, orthorhombic Fe_2Al_5, and monoclinic $FeAl_3$ phases are reported by the lack of order and low symmetry of the crystal structure, which affects its mechanical properties, for example, resulting in higher hardness and Young's modulus, compared to the Fe-rich IMCs [43]. Thus, the compounds with high aluminum composition, such as $FeAl_2$, Fe_2Al_5, and $FeAl_3$, present problematic applications due to their brittleness, while the compounds with high iron composition, such as Fe_3Al and FeAl, due to their good wear resistance, oxidation resistance, corrosion resistance, and specific strength properties, can be used as structural materials [44].

Table 3.1 – Hardness and crystal structure of different IMCs of the Al-Fe system [35, 39, 45-49].

IMC	**Fe_3Al**	**FeAl**	**$FeAl_2$**	**Fe_2Al_5**	**$FeAl_3$**
Lattice Parameters **(a,b,c = Å)** **(α,β,γ = °)**	a=b=c= 5.800 α=β=γ=90	a=b=c= 2.9097 α=β=γ=90	a=4.8745 b=6.4545 c=8.7361 α=87.930 β=74.396 γ=83.062	a=7.6559 b=6.4154 c=4.2184 α=β=γ=90	a=15.489 b=8.0831 c=12.476 α=γ=90 β=107.72
Crystal System/ Centering	Cubic Face-Centered	Cubic Primitive	Triclinic Primitive	Orthorhombic Base-Centered	Monoclinic Base-Centered
Space Group	Fm-3m	Pm-3m	P-1	Cmcm	C2/m
Wyckoff Position	Al: 4a Fe: 4b,8c	Al: 1a Fe: 1b	Al: 2i Fe: 1a,2i	Al: 4b,8f,8g Fe:4c (*)	Al: 2d,4g, 4i,8j Fe: 4i,8j (**)
Vickers Hardness (HV1)	330-368	470-667	1058-1070	1000-1158	772-1017

(*) The Wyckoff Positions 4c of the Fe, and 8f and 8g of the Al are the positions (0, 0.8277, 0.25), (0.5, 0.0340, 0.830), and (0.188, 0.1467, 0.25), respectively.

(**) The occupation of the Al in the Wyckoff Position 4g is 70%, and the Wyckoff Positions 4i and 8j are of the type (x, 0, z) and (x, y, z), respectively.

The presence of these IMC layers reduces the tensile strength and the ductility of the joint, and therefore, the control of process parameters is required to produce thin IMC layers. Thin IMC layers, thinner than 1-2 μm, are recommended for strong bond strength [39]. However, sound Al/steel joints can be obtained with a thickness of the IMC layers less than 10 μm [50]. Besides, the growth rate of the IMC layers can be decreased by increasing the carbon content in the steel base material or inhibited by the addition of silicon atoms [44].

Welding processes with less heat input are recommended to make dissimilar Al/steel joints because higher heat input produces a higher amount of IMC layers. This has made very difficult the production of strong Al/steel joints employing conventional fusion welding techniques. The thickness of the IMC layer can be limited through the control of the heat input, creating a liquid/solid-state weld. Another way to eliminate some of the problems inherent in fusion welding is using solid-state welding processes, in which the materials are welded by solid-state coalescence without liquid formation, eliminating issues such as solidification cracking and liquation, and reducing the IMC to a very thin layer [36, 39, 51].

3.2 Friction Stir Welding

Solid-state welding processes consist of bonding of materials through plastic deformation and diffusion due to the application of mechanical, electrical, or thermal energy at a temperature below the melting point of the base materials [52-53].

Since no melting occurs, solid-state welded joints are generally free of all defects that may occur in fusion welding processes, such as porosity, slag inclusion, and hot cracking. In addition, it does not require any shielding gas or filler metal [53].

Solid-state welding processes have the ability to weld different metals that can not be successfully joined using processes involving the melting of the base materials. For example, several solid-state processes are capable of welding aluminum to steel because, in these techniques, the two materials are not melted and mixed, which results in the formation of a thinner layer of brittle intermetallic compounds. Thus, if the steel and the aluminum are welded without melting, an interatomic attraction will be developed, and a joint without the presence of thick and brittle IMC layers will be produced [52].

There are many types of solid-state welding processes, such as forge welding, ultrasonic welding, diffusion welding, explosion welding, and friction stir welding. Each of these welding processes is different from each other in its main characteristics and applications [53].

Friction Stir Welding (FSW) was developed at The Welding Institute (TWI) in the United Kingdom in 1991 as a joining technique in the solid-state initially applied for the welding of aluminum alloys. The FSW process, shown in Figure 3.4a for butt joint configuration, consists of the insertion of a non-consumable rotating tool into the adjacent edges of the plates to be joined and in the traverse movement of the tool along the line of contact between the plates [54-55]. Other joint configurations can be used in the process, being the lap joint configuration, shown in Figure 3.4b, and the butt joint configuration, the most convenient joint configurations [54].

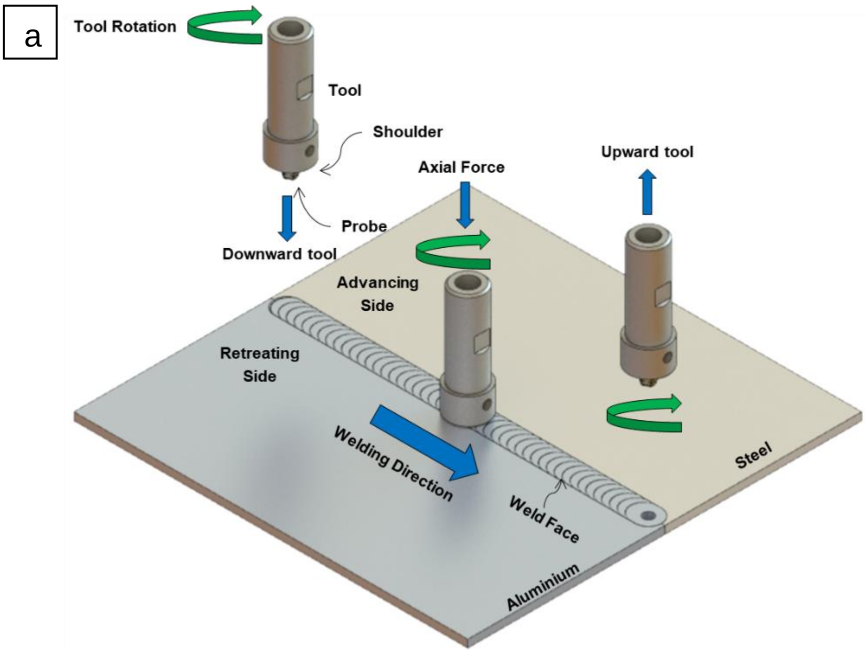
a
Tool Rotation
Tool
Shoulder
Axial Force
Upward tool
Probe
Downward tool
Advancing Side
Retreating Side
Welding Direction
Weld Face
Steel
Aluminium

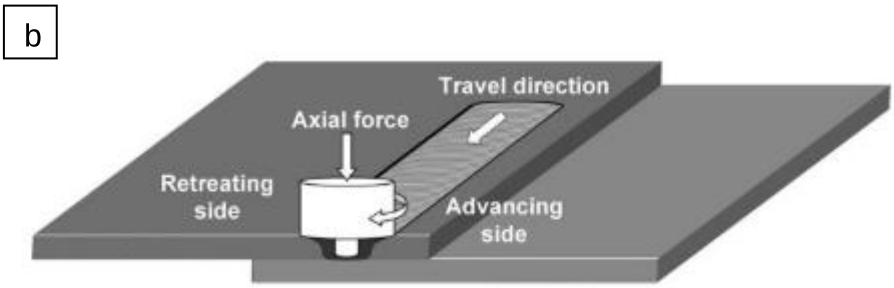

Figure 3.4 – (a) Schematic drawing of Friction Stir Welding in butt joint configuration (design developed at the Solid-State Joining Processes Department (WMP) of the Helmholtz-Zentrum Geesthacht (HZG) research institute) [56], and (b) in lap joint configuration. Adapted from [10].

The tool, composed by the shoulder and the probe, has two main functions, the heating of the base materials and the movement of materials, to produce a joint. The localized heating is achieved by friction between the tool and the base materials, and softens the material around the tool. The movement of material from the front to the backside of the probe is obtained by the combination of tool rotation and translation. As a result, a joint is produced in the solid state with a width approximately equal to the diameter of the shoulder in contact with the surface of the plates [54-55].

The advancing and retreating sides are defined in relation to the direction of tool rotation. The Advancing Side (AS) is the weld side where the tool rotation is in the same direction as the welding, and the Retreating Side (RS) of the tool is the weld side where the tool rotation and welding direction are opposite [55].

Two main parameters that can be varied in the FSW process are the rotational speed and the welding speed of the tool. Selecting these parameters largely controls the heat input. Excessive heat input, due to the high rotational speed and low welding speed, can contribute to the formation of voids in the joint, while the insufficient entry of heat can result in the fracture of the tool. The establishment of an operational window, that is, a set of process parameters that produce acceptable welds, is essential for many applications [54-55].

In addition, other important parameters are the tilt angle with respect to the surface of the plates to be welded, the axial force in the vertical direction applied in the tool, the geometry and dimension of the tool, and the joint design [53-55].

The FSW process has been already successfully used to join aluminum alloys, copper alloys, steels, magnesium alloys, metal matrix composites, and dissimilar material such as dissimilar aluminum alloys, copper alloys, and aluminum alloys to other metals, for many applications, such as aerospace, armor, automotive, and maritime [54, 57].

3.2.1 Welding Aluminum to Steel by Friction Stir Welding

In recent years, the application of the FSW process has been studied for several materials, being the welding of aluminum alloys to steel a small part of these studies. Despite this, FSW has become an important process for joining aluminum to steel. The studies cover different combinations of base materials, tools, process parameters, and joint configurations [9, 39, 58].

For the butt joint configuration, also named Friction Stir Butt Welding (FSBW) process, the steel plate should be placed on the advancing side for effective material flow and enhanced mixing, and there is an additional parameter, the tool probe offset, which is the distance between the side of the probe inserted in the aluminum alloy and the side of the steel plate. The positioning of the probe in the aluminum alloy leads to large plastic deformation of the aluminum alloy while the steel partially deforms, causing the dispersion and mixing of steel particles in the aluminum matrix [39].

Kimapong et al. studied the effects of rotational speed, axis position, and diameter of the probe on the tensile strength and microstructure of AA5083 and SS400 mild steel dissimilar joint friction stir welded, concluding that the increase of the probe offset causes the decrease of the joint tensile strength. Besides that, the effect of probe rotation direction on joint performance was also examined, and the joint with the aluminum plate on the advancing side was not achieved [59].

In the case of the lap joint configuration, also named Friction Stir Lap Welding (FSLW) process, the aluminum plate should be placed above to the steel base material. Similar to the microstructure of the butt joint, there are steel fragments scattered in the aluminum matrix, and the weld presents the Thermo-Mechanically Affected Zone (TMAZ), Heat Affected Zone (HAZ) and Base

Material (BM) in the aluminum and steel sides, and the Stir Zone (SZ) in the aluminum side [39], as shown in Figure 3.5.

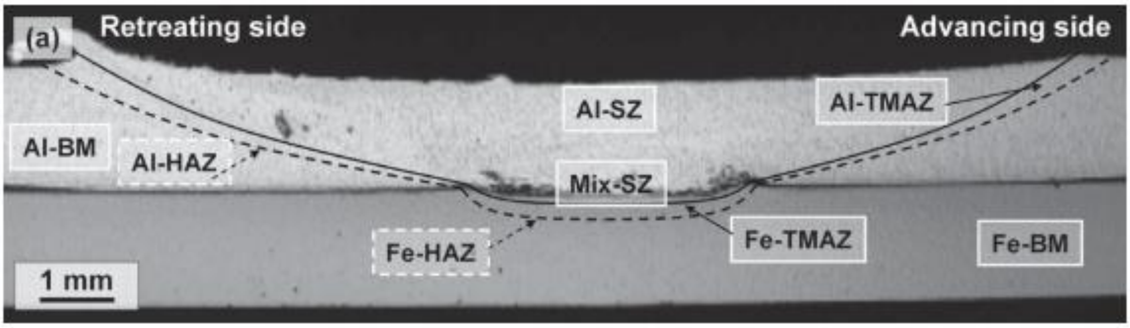

Figure 3.5 – Schematic view of the different welded zones of a joint [10].

The SZ is characterized by dynamically recrystallized equiaxial fine grains, which underwent high deformation and thermal cycles during the FSW process. The TMAZ, adjacent to the SZ, is characterized by deformed and elongated grains due to both plastic deformation and thermal cycle experienced during the welding. The HAZ, located between TMAZ and BM, which experienced only the thermal cycle, presents a grain similar to BM. The deformation of the steel is smaller because the probe is not inserted in the steel plates and because it's melting point is superior to the aluminum [10-12].

The interface of the welds consists of IMC layers with different compositions. Wei et al. [13] examined the influence of the depth of the probe in friction stir lap welded joints of AA1060 to austenitic stainless steel, and analyzed the interfacial morphology and mechanical properties. An interlaced structure was present in the interface of the welds, as shown in Figure 3.6 and Table 3.2, containing a mixed layer, composed by solutions of Fe in Al (point 6) and possible $FeAl_3$ phase (point 4), and the deformed steel (point 5), as a result of severe plastic deformation of the materials in the stir zone. On the other hand, Chen et al. [14] obtained welds of AA6060-T5 and mild steel with an interface composed of irregular laminates of steel and thin intermetallic layers of $FeAl_2$ or Fe_2Al_5.

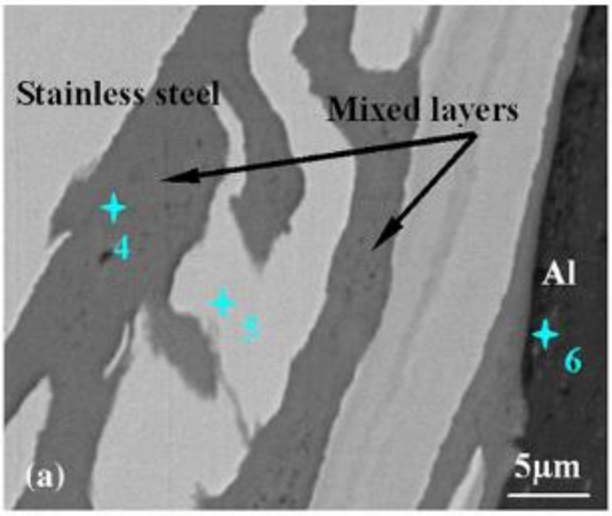

Figure 3.6 – An interlaced structure in the interface of a joint produced using a welding speed of 150 mm/min, a rotational speed of 950 rpm, and an insertion depth of 3.2 mm [13].

Table 3.2 – Energy Dispersive X-Ray Spectroscopy (EDS) at points 4, 5, and 6 indicated in Figure 3.6 [13].

Point	**Chemical Composition (at.%)**			
	Al	**Fe**	**Cr**	**Ni**
4	73.12	21.45	5.43	2.82
5	1.27	72.26	17.95	8.52
6	97.24	1.87	0.59	0.30

The size of the IMC layers is increased with high heat input conditions, such as low travel speed and high rotational speed, as same as the steel fragments, that difficult the material flow and generate voids and cracks, reducing the tensile strength. However, due to the dissimilarities in properties of both aluminum and steel, the stir zone always presents tensile strength less than or equal the aluminum base material [39].

In general, the studies are focused on eliminating weld defects through microstructural and tensile property optimization, and just a few studies have been conducted to control the amount and morphology of the IMC, and to understand the mechanisms of the intermetallic formation and growth [60].

In this context, Lan et al. [15] analyzed the interface of AA6061-T6 and TRIP780 steel and measured the size of the intermetallic compound layer as a function of the welding conditions. They concluded that the IMC layer identified, shown in Figure 3.7a, could be either FeAl or Fe_3Al, formed due to diffusion and reaction, and that the thickness of these layers can be reduced under higher welding speed, smaller rotational speed and higher tool offset, as shown in Figure 3.7b and c.

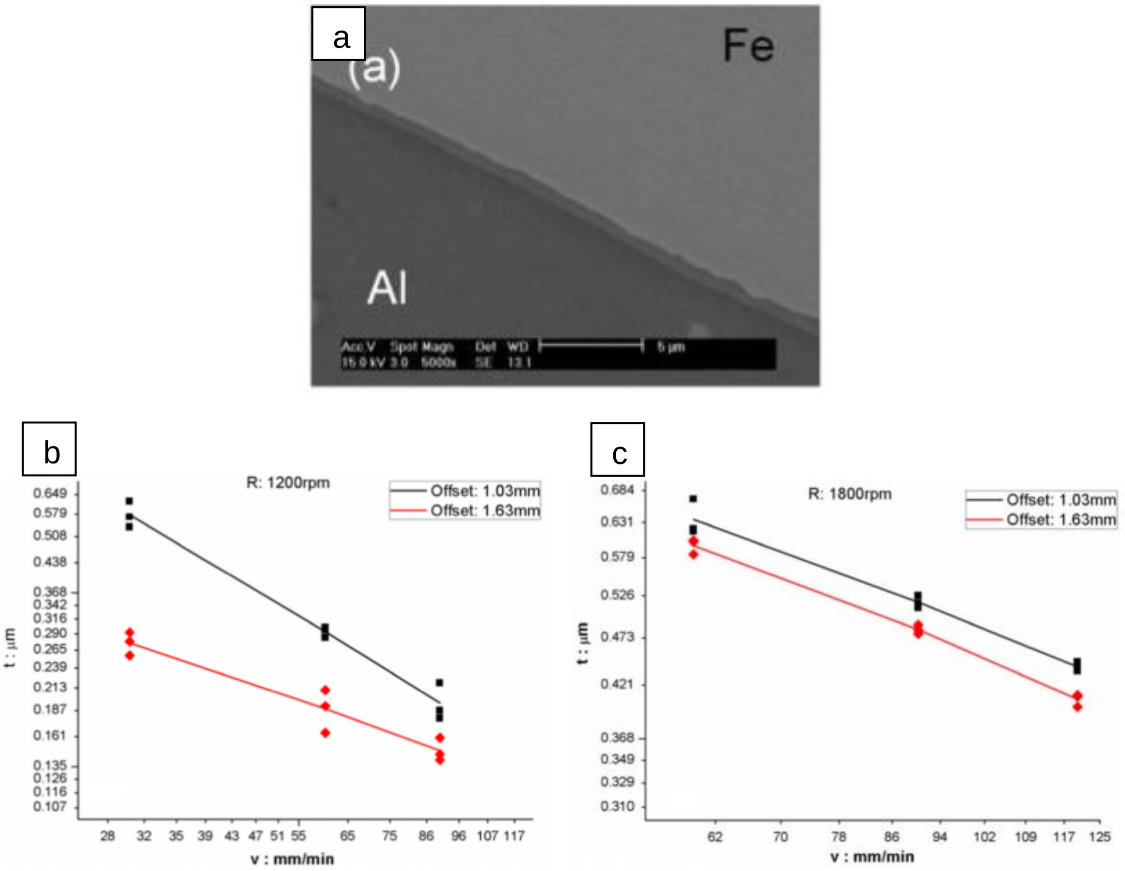

Figure 3.7 – a) SEM images of the Al-Fe interface under rotational speed of 1800 rpm, tool offset of 1.63 mm, and welding speed of 60 mm/min, and relationships between the thickness of the interlayer (t) and welding speed (v) under different tool offsets and rotational speeds in logarithm scale of b) 1200 rpm and c) 1800 rpm [15].

3.3 AA5083-O/H111 Aluminum Alloy

Since the end of the 19th century, when Charles Hall in Ohio and Paul Heroult in France developed independently, the electrolytic reduction of alumina (Al_2O_3) dissolved in molten cryolite, the aluminum has been an economic competitor in engineering applications. However, it became an attractive material in shipbuilding only after the Second World War, when the development in arc welding processes gave an alternative to riveting as a joining method for the material [61-62].

The pure aluminum density of 2.7 g/cm^3, which is approximately a third of the steel density (7.83 g/cm^3), delivers many benefits in transport applications, such as aerospace, automotive, and marine. The metal's lightweight performance helps to increase fuel economy and to reduce emissions, as well as increase the speed in the automotive and in other transport sectors. Another significant advantage is its excellent corrosion resistance in most environments, such as atmosphere, water, many chemical systems, and petrochemicals [61, 63]. In the seawater, the pitting corrosion is the most common form of corrosion that can occur to aluminum alloys, due to the pH (approximately 8.2) close to neutral, and the presence of chloride ions that are absorbed and cause the local rupture of the natural oxide film formed in the aluminum surface. Despite this, immersion tests carried out over the last years showed that the 5xxx and 6xxx aluminum alloy series present excellent corrosion resistance in seawater and marine environment. Anyway, protections, such as paint and anodization, are recommended in some situations for these aluminum alloy series and must be used in the 2xxx, 6xxx, and 7xxx aluminum alloy series for marine applications [30, 63].

Despite the use of aluminum in many transportation areas, in shipbuilding and other harsh operating conditions, the aluminum was only widely used after the development of commercially available aluminum-magnesium alloys in the 1930s. Besides the excellent corrosion resistance, these alloys are also weldable, which has led them to be firmly established as a fundamental building material [63].

In addition, advantageous properties such as thermal and electrical conductivity, suitability for surface treatments, diversity of semi-products, functional advantages of extruded and cast semi-products, ease of formability and ease of recycling, have led to the development of applications for aluminum and its alloys, as well as the sustained increase in consumption [63].

There are a variety of aluminum alloys being used, that can be separated into two different classes, which are the non-heat treatable alloys and the heat treatable alloys. Non-heat treatable alloys need to be strain-hardened by cold working, usually combined with annealing procedures to increase tensile strength. The heat treatable alloys contain solid solution elements that decrease in solubility with decreasing temperature, in concentrations exceeding their equilibrium solid solubility at room temperature and moderately higher temperatures. These alloys respond to thermal treatments such as solution heat treatment, quenching, and precipitation hardening [61, 64]. Table 3.3 shows the division of aluminum alloy series based on these classes [65].

Table 3.3 – Series of treatable and non-heat treatable aluminum alloys and their respective alloying elements. Adapted from [65].

Method of Hardening	Series	Alloying Element
Strain Hardening	1xxx	None
	3xxx	Manganese
	5xxx	Magnesium
	8xxx	Iron and Silicon
Age Hardening	2xxx	Copper
	4xxx	Silicon
	6xxx	Magnesium and Silicon
	7xxx	Zinc and Magnesium

Among aluminum alloys, aluminum-magnesium alloys (5xxx series) and aluminum-magnesium-silicon alloys (6xxx series) are the most suitable for shipbuilding. Some of the typical aluminum alloys used in shipbuilding are the AA5083, AA5059, AA6005A, and AA6082 aluminum alloys. Alloys AA 5083 and

AA5059, as well as alloy AA5383, are monophasic alloys whose mechanical properties are determined by the content of solid solution elements and the grain size. As previously stated, the 6xxx series aluminum alloys are suitable for heat treatment and, because of this possibility, are less used in manufacturing processes that can undergo metallurgical variations, such as welding [62, 66].

In the 5xxx series, the presence of magnesium as a major element or with manganese results in a moderate-to-high-strength work-hardenable alloy, but to avoid susceptibility to stress-corrosion cracking, should be placed certain limitations on the amount of cold work and the safe operating temperatures permissible for the higher-magnesium alloys. However, alloys in this series present good welding characteristics and corrosion resistance in marine environments [61].

The AA5083 aluminum alloy, considered as base alloy in the naval industry [66], or EN AW-5083 (ISO: Al Mg4.5 Mn 0.7), presents 4-5% of magnesium and additions of manganese and chromium, and exhibits in the O/H111 tempers typical values of yield strength, $R_{p0,2}$, of 125 MPa and ultimate tensile strength, R_m, between 275 and 350 MPa. The tempers O and H111 indicate that the aluminum alloy used in this study was respectively annealed to improve ductility and dimensional stability, and slightly strain hardened by rolling to improve their dimensional characteristics [65, 67].

Tronci et al. [68] analyzed friction stir welds in 1 mm thick plates of AA5083-H111 aluminum alloys using different welding conditions, including different process control modes, tool parameters, and process parameters. The base material used presented a recrystallized microstructure, as shown in Figure 3.8, with approximately equiaxed and uniform grain sizes of 18 μm and hardness of 71 HV. Analyzing the results, they concluded that the welding conditions influenced only slightly the hardness and grain size of the Thermo-Mechanically Affected Zone (TMAZ), with a maximum hardness value of 79 HV and the yield stress practically equal to the base material.

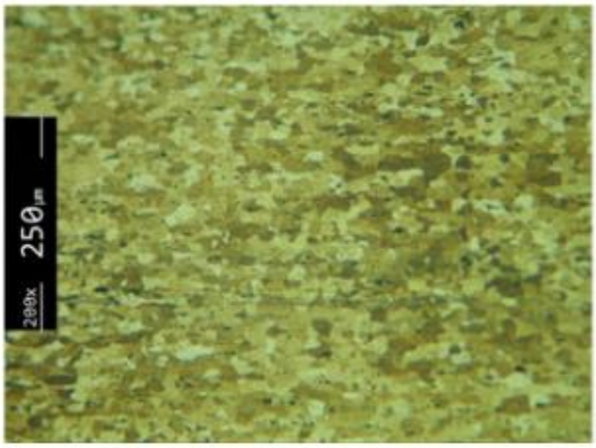

Figure 3.8 – AA5083 base material microstructure [68].

Peel et al. [69] investigated the effect of different welding speeds on microstructural and mechanical properties and residual stress of AA5083 aluminum alloys FSW welds. The microstructural analyses resulted in a nugget with a typical appearance for these welds, including the presence of “onion rings” formed by texture variations, as shown in Figure 3.9. Besides that, due to annealed microstructure resulted around the weld line, they concluded that thermal input, responsible for the dynamic recrystallization mechanism and subsequent grain growth, was the dominant effect in the weld properties.

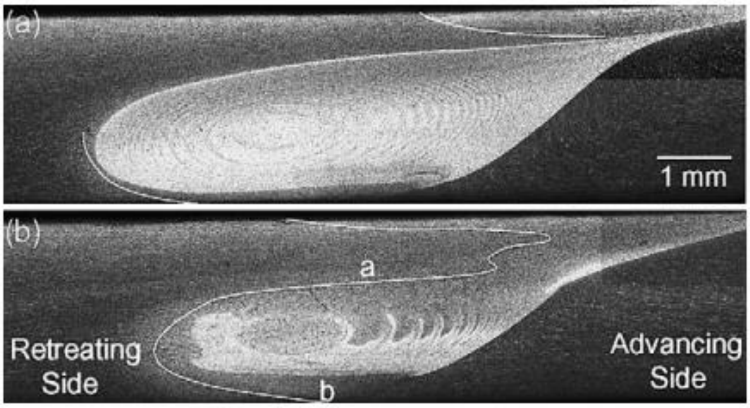

Figure 3.9 – Transverse section macrograph of two different weld zones, with lines indicating remnants of the weld line, produced using a welding speed of (a) 100 mm/min, and (b) 200 mm/min. The letters a and b in item (b) represent two regions analyzed by the author in tensile tests [69].

3.4 GL D36 Steel

Steels are the most commonly used materials for shipbuilding. These began to be used after the iron replaced the wood in the manufacture of hulls in the 18th century. Since then, a variety of types and shapes of steels have been used to build vessels. These steels must meet requirements such as strength, flexibility, easy manufacturing, weldability, and fracture strength [70].

These materials provide a wide range of mechanical properties, from moderate strength levels (200-300 MPa) with excellent ductility until strengths higher than 1400 MPa with fracture toughness as high as 110 MPa.m$^{1/2}$ [70], and also present a low processing cost [71].

Several categories of steels are used in shipbuilding. These are low carbon steels, High-Strength Steels (HSS), High-Strength Low-Alloy (HSLA) steels, and stainless steel [70].

According to the classification society Germanischer Lloyd (Germany), the grade GL D36 (or GL DH36 or ASTM A131 class DH36), commonly used for shipbuilding and marine application, is a High-Strength Steel (HSS) [72], also design as a low carbon steel, high manganese, and niobium micro-alloying [73].

In the case of HSS, the mechanical properties required by the standard are achieved by the addition of carbon, manganese, and aluminum in a manner similar to steels of moderate strength. However, due to the higher strength and toughness resistance required by these steels, other elements still have to be added. Niobium, vanadium, and titanium have the same function as aluminum and therefore act as grain refiners. Copper, chromium, nickel, and molybdenum can be added to harden the steel by metallurgical mechanism of substitutional solid solution [74].

As reported by Lehto et al. [75], the steel grade D36 presents a ferritic-pearlitic microstructure, shown in Figure 3.10, and according to the requirements standardized by Lloyd’s Register for HSS, they are supplied in the rolled condition and have a minimum yield strength of 355 MPa and an ultimate tensile strength between 490 MPa and 630 MPa [76].

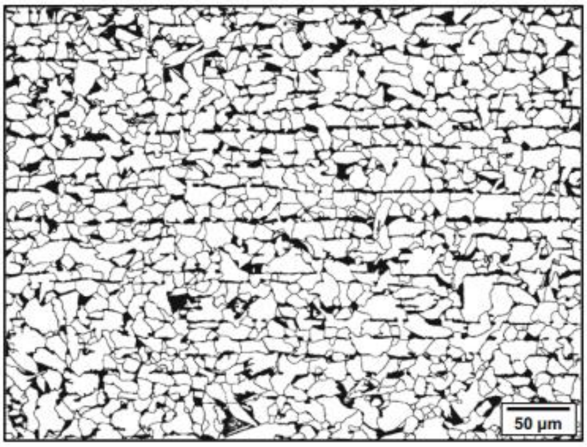

Figure 3.10 – Microstructure of the steel GL D36 base metal [75].

This grade can achieve an ultimate tensile strength of about 950 MPa and yield strength of about 650 MPa when friction stir welded [77]. Mechanical properties of these welds are enhanced due to metallurgical changes induced by the process, such as the grain refinement of the ferrite and perlite, and the formation of bainite and martensite from austenite grains in the regions under high plastic deformation and relatively rapid cooling rates [77].

4 MATERIALS AND METHODS

4.1 Material

The base materials used in this study were a 250 mm long, 130 wide and 4 mm thick AA5083-O/H111 plates and a 250 mm long, 130 mm wide and 6 mm thick GL D36 steel plates. The chemical composition of the base materials is shown in Table 4.1. AA5083 was provided with the chemical composition according to the ASTM B209M-14 [78], and Spark Spectrometric analysis was used to measure the chemical composition of GL D36 steel.

Table 4.1 – Chemical composition of AA5083 and GL D36 steel.

Material	**Chemical Composition (wt.%)**								
AA 5083	Si	Fe	Cu	Mn	Mg	Cr	Zn	Ti	Al
O/H111	0.111	0.368	0.065	0.520	4.78	0.104	0.157	0.012	Rest
Steel	C	Si	Mn	P	S	Ni	Al	Cu	Fe
GL D36	0.17	0.39	1.4	0.013	<0.01	0.02	0.027	0.03	Rest

The tool used for the welding consisted of a flat and scrolled shoulder with 15 mm in diameter, and a threaded conical probe with three flats, 6 mm in diameter and 4.2 mm in length, as shown in Figure 4.1, both made of Hotvar hot-work tool steel (2.6% Cr, 2.25% Mn and 0.85% V).

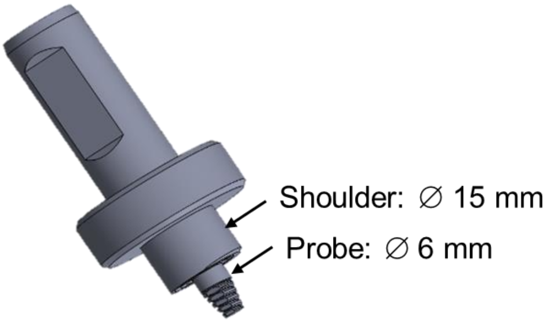

Figure 4.1 – Tool attachment configuration used for welding.

4.2 Methods

4.2.1 Welding Procedure

The welds were carried out at the Solid-State Joining Processes Department (WMP) of Helmholtz-Zentrum Geesthacht (HZG) research institute in Germany. The process used was Friction Stir Welding (FSW), varying welding speed and tool rotational speed. The welding processes were done using an FSW Gantry System, presented in Figure 4.2, with horizontal table movement. Through its software interface was possible to control the parameters during the welding procedure, such as rotational speed, welding speed, and axial force, and to obtain the measurements of the tool torque and the forces in the plane. The tilt angle was fixed manually in the equipment.

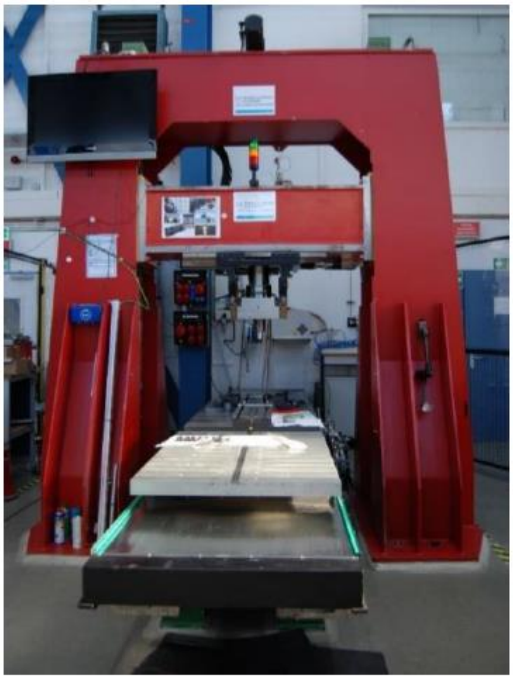

Figure 4.2 – Gantry System – Friction Stir Welding machine.

The welds were produced with the lap joint configuration and an overlap of 30 mm. The aluminum plate was placed above the steel on the advancing side, as shown in Figure 4.3.

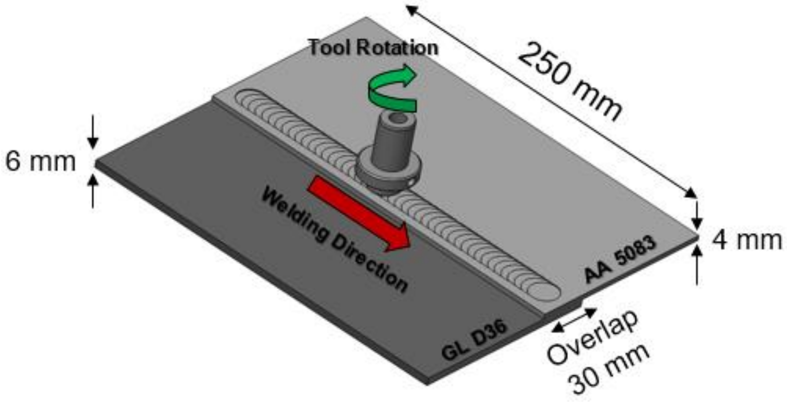
Tool Rotation
250 mm
6 mm
4 mm
Welding Direction
AA 5083
GL D36
Overlap
30 mm

Figure 4.3 – Schematic illustration of the lap joint configuration.

The tilt angle and the axial force were fixed in 0.5º and 15 kN, respectively, and the welding speed and rotational speed were varied, as shown in Table 4.2.

Table 4.2 – Welding parameters used to join AA5083 aluminum alloy to steel GL D36 in a lap joint configuration.

Weld	**Tool Welding Speed (mm/s)**	**Tool Rotational Speed (rpm)**
1	5	300
2	5	500
3	5	700
4	5	900
5	5	1100
6	7	700
7	9	700
8	13	700
9	15	700
10	7	900
11	9	900
12	11	900
13	13	900
14	15	900

4.2.2 Welds Characterization

Hereafter, the techniques used in the microstructural and mechanical characterization of the samples are detailed. All equipment used was available at DEMa-UFSCar or WMP-HZG.

4.2.2.1 Microstructural Characterization

The microstructural analysis was carried out to evaluate the different weld zones and the presence of defects in the joints with the process parameters variation.

For this, the welded plates were sectioned from 5 mm of the end of the weld, and used for microstructure analysis. The metallography procedure was then performed as described in ASTM E3-11 [79], followed by electrolytic etching for the aluminum part and chemical etching for the steel part, and observation of the samples in the optical microscope, in order to identify and understand what microstructural modifications occurred with the material due to the welding process.

The cutting procedure was carried out in a Struers Axitom® using a 50S35 cut-off disc with a linear displacement speed of 0.2 mm/s in the vertical direction.

After this, the samples were embedded with a mixture of Demotec-20® powder and resin, in the proportion of 2:1, respectively, in a polyethylene mounting cups. The grinding/polishing step was performed in a Struers Tegramim® equipment, starting with a grinding disc (320 mesh) with water, followed by a Struers Largo®, a Struers Dac® and a Struers Dur® polishing cloth discs with diamond suspension lubricant of 9 μm, 3 μm and 1 μm, respectively, and were finished with a Struers Chem® polishing cloth disc with OP-S (0.4 μm).

The aluminum part of the sample was electrolytically etched using Barkers Etchant in a Struers LectroPol-5® with a voltage of 20 V for 120 seconds, and the steel part of the sample was chemically etched using Nital 0.5% for 40 seconds.

Then, the samples were observed in a Leica SM IRM® optical microscope equipped with 90º polarized light. Pictures were taken with the program Leica

Application Suite®, and the grain size of the materials was determined through the intercept method according to the ASTM E112-13 [80] standard.

4.2.2.2 Mechanical Characterization

Mechanical characterization was used to determine the properties of the joints, and to evaluate the application of the FSW process to join aluminum to steel in comparison with the current welding processes.

For this, hardness tests, according to ASTM E384-17 [81], were performed along the cross-section of the welded samples to characterize the different weld zones, analyzing the occurrence of microstructural alteration in the regions of the weld and mixing between the different materials.

A Struers DuraScan® machine was used to evaluate the hardness profile along the cross section of the welded samples. The load applied, the indentation time, and the distance between each indentation in a row was 200 gf, 10 seconds and 0.25 mm, respectively. A row of indentation in the aluminum alloy and a row in the steel were made, both with 1 mm of distance to the interface between aluminum and steel. Also, it was done a row in the vertical direction in the middle of the Stir Zone (SZ).

The welds were also tested for lap shear strength to determine the maximum shear force and displacement to fracture, as well as to obtain information about the fracture mechanism.

The lap shear tensile test was carried out in a screw-driven Zwick/Roell® testing machine with a load capacity of 100 kN at room temperature. The test samples presented 25 mm in width and 212.5 mm in length. The separation gap between the clamps and the displacement rate was 112.5 mm and 1 mm/min, respectively. Each test was performed in triplicate, and the results were analyzed by the mean of the measurements.

4.2.2.3 Interface Characterization

The interface characterization was made to measure the size and the composition of the Intermetallic Compound (IMCs) layers formed at the interface between the aluminum and steel plates, since these IMCs directly affect the mechanical properties of the joint.

The metallographic preparation of the samples was done as described above. After this, the samples were analyzed in a Scanning Electron Microscopy (SEM) Philips XL-30 FEG equipped with Energy Dispersive X-Ray Spectroscopy (EDS), present in the Laboratory of Structural Characterization (LCE)/DEMa, in different magnifications.

Additional X-Ray Diffraction (XRD) was done to identify the phase formation in the IMC layers. The 2θ range from 5° to 120° and Cu-$K_{\alpha1}$ radiation were used on a Bruker D8 Advance ECO XRD instrument, also present in the LCE/DEMa. The software GSAS-II [82] was used to compare the experimental results with the theoretical XRD patterns through the Rietveld refinement. For this comparison, it was first necessary to define the parameters of the XRD equipment, which was done through the refinement of the equipment parameters in the software GSAS-II, using the diffractogram pattern of a standard sample of ZnO oxide obtained in the same XRD equipment, the NIST SRM 674b [83] standard, and the theoretical XRD pattern of the ZnO phase. Then, these equipment parameters were used to refine the lattice parameters and the fraction (wt.%) of the phases possibly formed in the IMC layers in the software GSAS-II during the comparison of the experimental results of the sample welded with the theoretical XRD patterns.

5 RESULTS AND DISCUSSION

5.1 Energy Input

Microstructural, interface, and consequently, mechanical properties of the joints are dependent on the material plastic deformation and heat flow during the Friction Stir Welding (FSW). The heat generated in the FSW mainly results from the friction between the tool and the base materials and is affected by the process conditions [84]. Thus, to understand the influence of the welding speed and tool rotational speed on the joints properties, it is important the knowledge of the influence of these process parameters on heat generation during the formation of the joints.

The torque-based model shown in Equation 5.1 can be used for the estimation of the average energy input generated per unit length in FSW of dissimilar aluminum/steel joints, as reported by Wei et al. [13]. ν, n, T, and η are the welding speed (mm/min), tool rotational speed (rpm), tool torque (N.m), and efficiency of heat transfer to the weld, respectively.

$$Q = \eta \frac{2\pi n T}{v} \qquad (5.1)$$

The tool torque during the welding was given by the FSW machine’s software interface as a function of the displacement, as shown in Figure 5.1. The average tool torque during welding is presented in Table 5.1 for each welding condition, and the comparison between the process parameters shows an increase in the average torque when increasing the welding speed and decreasing the rotational speed. The maximum average torque was achieved in the weld 1, produced using a rotational speed of 300 rpm, and the minimum average torque in the weld 5, produced using a rotational speed of 1100 rpm, both welds produced using a welding speed of 5 mm/s. Besides, it can be observed that the torque variation is more significant for variations in rotational speed than in welding speed, which can be related to the greater influence of the rotational speed in the heat generation and temperature distribution, as related in the literature [85].

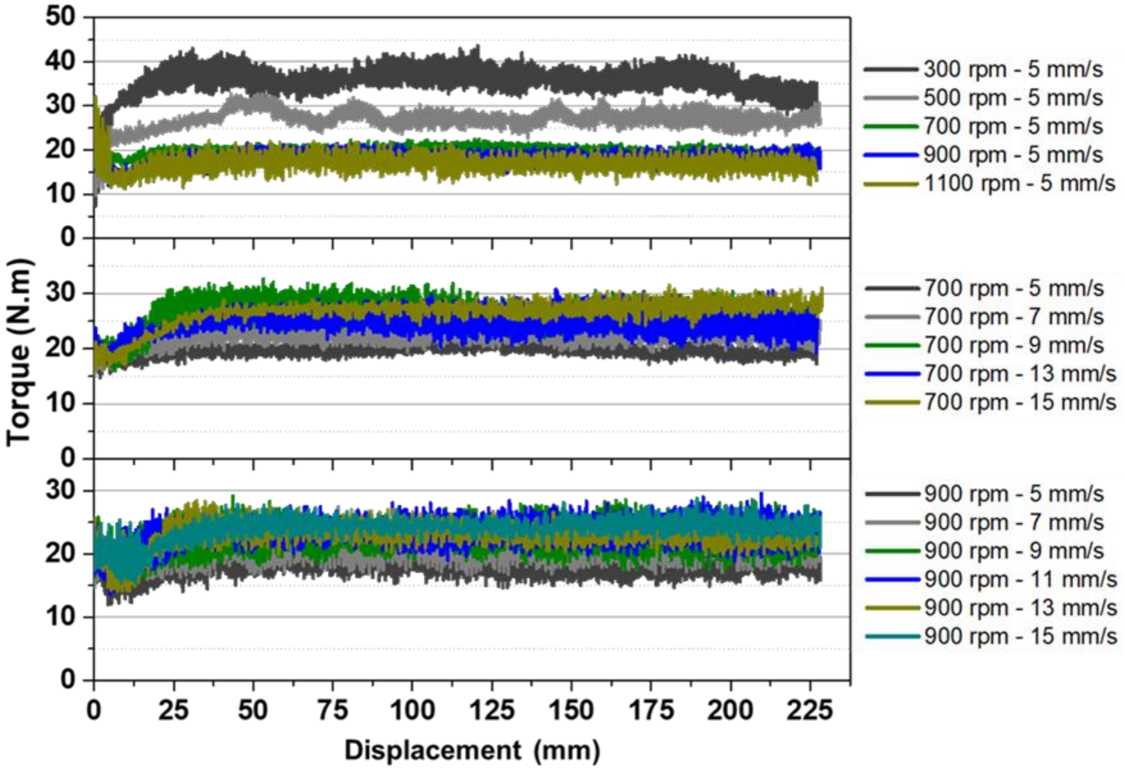

Figure 5.1 – Tool torque during the production of the joints by FSW, with tool rotational speeds from 300 rpm to 1100 rpm, and welding speeds from 5 mm/s to 15 mm/s.

Table 5.1 – Average tool torque during FSW with different rotational speeds and welding speeds.

Welding Speed (mm/s)	**Rotational Speed (rpm)**	**Average Torque (N.m)**	**Welding Speed (mm/s)**	**Rotational Speed (rpm)**	**Average Torque (N.m)**
5	300	35.91 ± 2.74	13	700	25.57 ± 2.40
5	500	27.66 ± 1.70	15	700	27.38 ± 1.31
5	700	19. 80 ± 0.90	7	900	21. 57 ± 2.53
5	900	18.27 ± 1.37	9	900	23.01 ± 2.61
5	1100	17.00 ± 1.72	11	900	23.96 ± 2.16
7	700	23.14 ± 1.83	13	900	23.43 ± 1.69
9	700	26.80 ± 2.37	15	900	24.60 ± 1.49

Considering a typical value of η = 0.9 [13] and the tool torque during the welding process given in Figure 5.1, the average energy input per unit length was calculated using Equation 5.1, and the results are presented in Figure 5.2 in relation to the welding speed and tool rotational speed. Differently of the tool torque, the average energy input increases when decreasing welding speed and increasing rotational speed, achieving the maximum average energy input in the weld 5, produced using welding speed of 5 mm/s and rotational speed of 1100 rpm, and the minimum average energy input in the weld 9, produced using welding speed of 15 mm/s and rotational speed of 700 rpm.

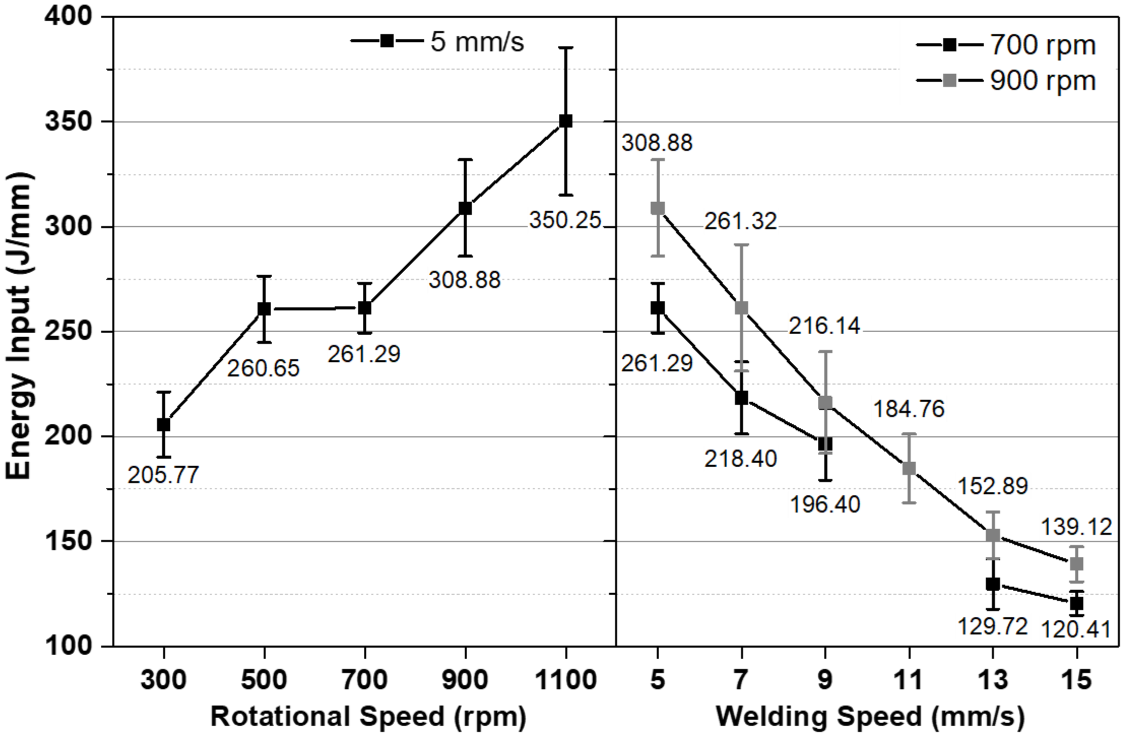

(a) (b)

Figure 5.2 – Average energy input during the production of the joints by FSW at a constant (a) welding speed of 5 mm/s, and (b) two different rotational speeds of 700 rpm and 900 rpm.

The tool torque is considered as a measure of the shear stress resulting from the friction between the tool and the base materials, which is responsible for heat generation and material flow, and is related to the plasticized material and temperature during the welding [86]. The increase in the rotational speed results in the increase of the plastic deformation of the materials and the friction action of the tool, increasing the heat generation. The increase in the energy input and temperature during the process cause the more quickly plasticization of the materials, which reduces their viscosity and the resistance to material flow, and consequently reduces the shear stress and tool torque. On the contrary, the increase in the welding speed results in a decrease in the time available for plastic deformation and frictional heat generation, which results in a decrease in the energy input and a slight increase in the resistance to material flow and tool torque. Similar behavior was related by Das et al. [86], who stated the importance of the energy input on joint strength of AA6063 to zinc-coated steel FSW welds.

5.2 Macrostructural Characterization

Degradation of the mechanical properties of joints produced by FSW is reported to occur due to the presence of defects in the joints surface and cross-section, which are formed by unsuitable material flow during the welding [9]. Surface defects such as flash, groove, furrow, and hole, and cross-section defects such as void and tunnel type defect, are commonly reported in the literature for dissimilar aluminum/steel FSW joints and are related to the incorrect heat generation and plastic deformation during welding due to the improper selection of process parameters [9, 13, 87-89].

The visual inspection investigated the presence of defects on the surface of the welds, as shown in Figure 5.3. Almost all the welds presented good surface quality, without the formation of defects, as shown in Figure 5.3a for the weld 3, produced using a welding speed of 5 mm/s and rotational speed of 700 rpm. Just the weld 5, shown in Figure 5.3b and produced using a welding speed of 5 mm/s and rotational speed of 1100 rpm, presented excessive flash on the surface.

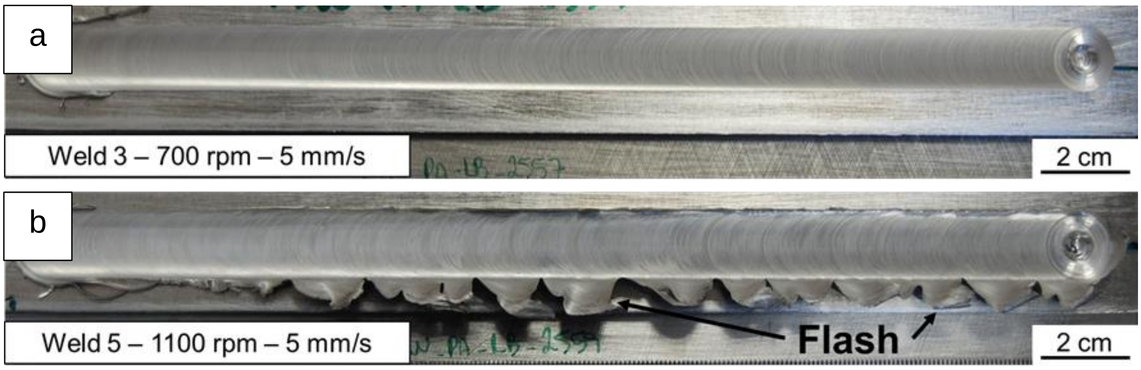

Figure 5.3 – Visual Inspection of the surface of the welds produced by FSW using a welding speed of 5 mm/s and rotational speed of (a) 700 rpm and (b) 1100 rpm.

The flash formation on the surface of the weld 5 occurred due to the highest energy input per unit length during the FSW among the joints analyzed (showed in Figure 5.2), resulting from the higher rotational speed, which causes extensively thermal softening of the aluminum under the shoulder. Because of this, the aluminum softened was no longer able to support the constant force applied by the tool during the process and then was extruded through the lateral of the shoulder, forming the excessive flash on the surface. This represented a limitation for the increase in the rotational speed, in view that the extrusion of material out of the weld zone causes a reduction of the weld thickness or lack of material to fill the cavity left by the probe, resulting in degradation of the mechanical properties of the joints. The decrease of the rotational speed was enough to avoid the flash formation in the other welds, as can be seen in Appendix A, where is presented the visual inspection for each welding condition investigated in this study.

The macrostructure of the welds is characterized by the presence of the steel hook on the Retreating Side (RS) of the weld zones, and steel particles dispersed in the aluminum matrix, as shown in Figure 5.4a to Figure 5.4d. Moreover, tunnel-shaped void defects were identified for some process parameters, as shown in Figure 5.4a and Figure 5.4b, and cracks were found in the interface of the weld 5, produced using a welding speed of 5 mm/s and rotational speed of 1100 rpm, as shown in Figure 5.4d.

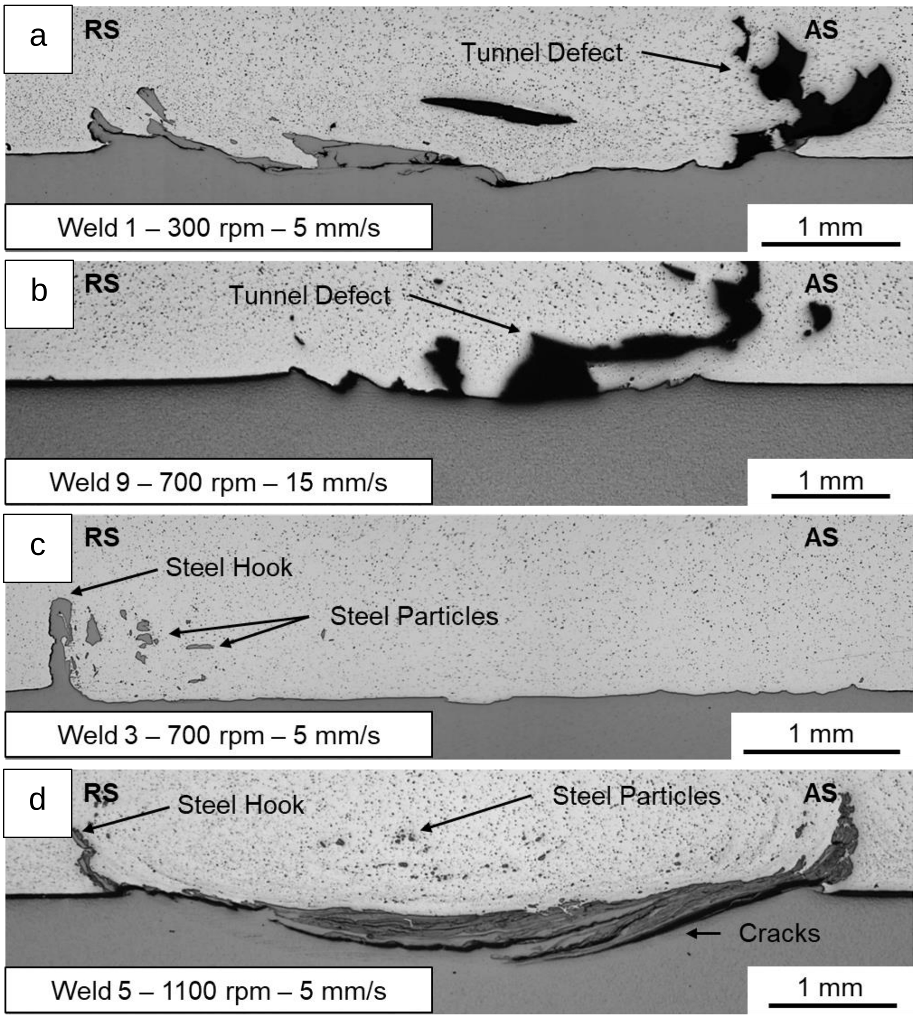
a
RS
AS
Tunnel Defect
Weld 1 – 300 rpm – 5 mm/s
1 mm
b
RS
AS
Tunnel Defect
Weld 9 – 700 rpm – 15 mm/s
1 mm
c
RS
AS
Steel Hook
Steel Particles
Weld 3 – 700 rpm – 5 mm/s
1 mm
d
RS
AS
Steel Hook
Steel Particles
Cracks
Weld 5 – 1100 rpm – 5 mm/s
1 mm

Figure 5.4 – Macrostructure of the welds produced by FSW using welding speed and rotational speed of (a) 5 mm/s and 300 rpm, (b) 15 mm/s 700 rpm, (c) 5 mm/s and 700 rpm, and (d) 5 mm/s and 1100 rpm.

The presence of tunnel defect, void, crack, or steel hook in the cross-section macrostructure of the welds is presented in Figure 5.5 for each process parameter, according to the welds macrostructure for each welding condition investigated in this study, which can be found in Appendix B. The tunnel defects were observed in the macrostructure of the welds produced using low rotational speed or high welding speed, and cracks were observed in the weld produced with the highest rotational speed. The steel hooks were present in the macrostructure of all the welds, but with a more significant height in the welds produced using low welding speed and intermediate rotational speed.

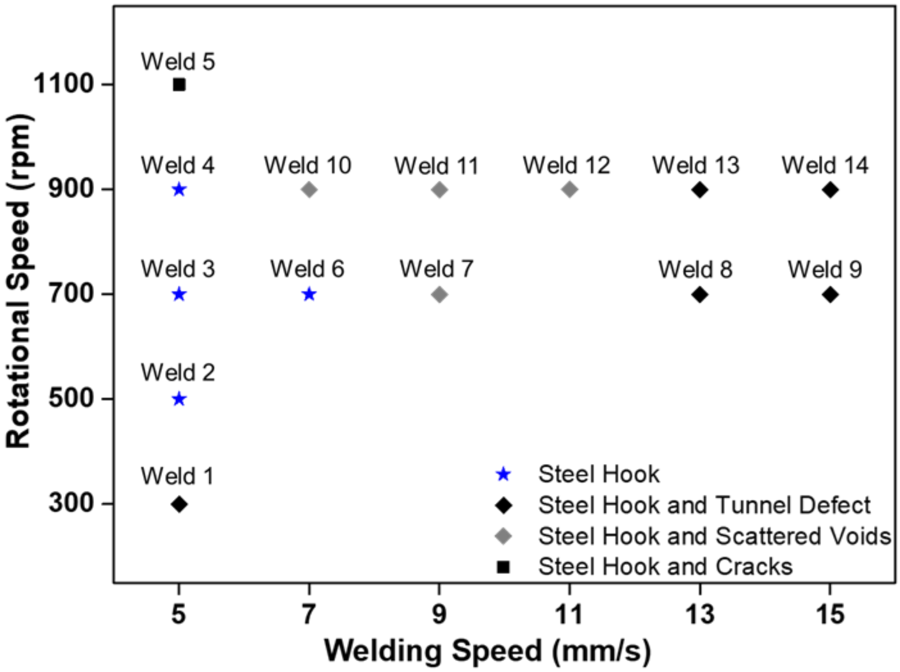

Figure 5.5 – Welds according to its process parameters and macrostructure features.

The welding with low rotational speed, such as 300 rpm (weld 1), or high welding speed, such as of 13 mm/s (welds 8 and 13) and 15 mm/s (welds 9 and 14), resulted in insufficient energy input and plastic deformation of the softened aluminum, and consequently, in the inefficient aluminum flow to fill the cavity left by the probe. As showed previously, weld 1 presented the highest average tool torque among the parameters studied, as a consequence of the higher resistance to material flow when the energy input was insufficient to correctly plasticizes the aluminum in the weld zone due to the low rotational speed used in the welding, which resulted in the formation of the tunnel defect. In the welds produced using a high welding speed, despite the decrease in the average tool torque compared to the weld 1, these welds presented the lowest values of average energy input per unit length due to the decrease in the welding time, which reduced the time available for the correct filling of the weld zone, also resulting in the formation of the tunnel defect.

The decrease of the welding speed to 11 mm/s (weld 12), 9 mm/s (welds 7 and 11), and 7 mm/s (weld 10) caused the transition from tunnel defects to scattered voids in the welds' macrostructure, as shown in Figure 5.6. Differently of the tunnel defects, these voids are smaller and not continuous throughout the weld length, due to the higher energy input per unit length during the welding that improved the material flow.

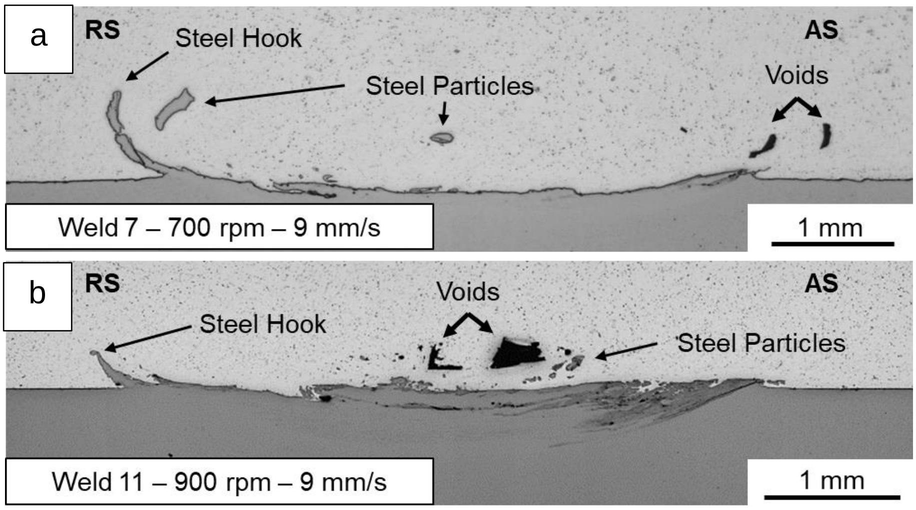

Figure 5.6 – Macrostructure of the welds produced by FSW using a welding speed of 9 mm/s and rotational speed of (a) 700 rpm, and (b) 900 rpm.

The position of these defects preferentially on the Advancing Side (AS) is a consequence of the material flow that is transported from the RS to the AS at the back part of the probe during the FSW process. The material flow during the welding is given by the movement of the softened aluminum from the front to the back part of the probe through the RS, which is possible due to the tool rotational direction opposite to the welding direction on this side of the weld and is responsible for the transport of material to the AS. Accordingly, when the softening and movement of materials are insufficient, the materials are not correctly consolidated in the weld zone, resulting in voids and tunnel defects preferentially on the AS [90-91].

For low welding speeds as 5 mm/s and 7 mm/s, and rotational speed ranging from 500 rpm to 900 rpm (welds 2, 3, 4, and 6), sound joints were produced, without the presence of macro voids, tunnel defects, or cracks in its cross-section macrostructure. Moreover, these welds were characterized by the presence of the steel hook on the RS and plastically deformed steel fragments dispersed in the aluminum matrix, as shown detailed in Figure 5.7. The energy input per unit length in these welds ranges from around 220 J/mm to 310 J/mm, indicating the energy input per unit length necessary to the correct material flow using the welding conditions considered in this study.

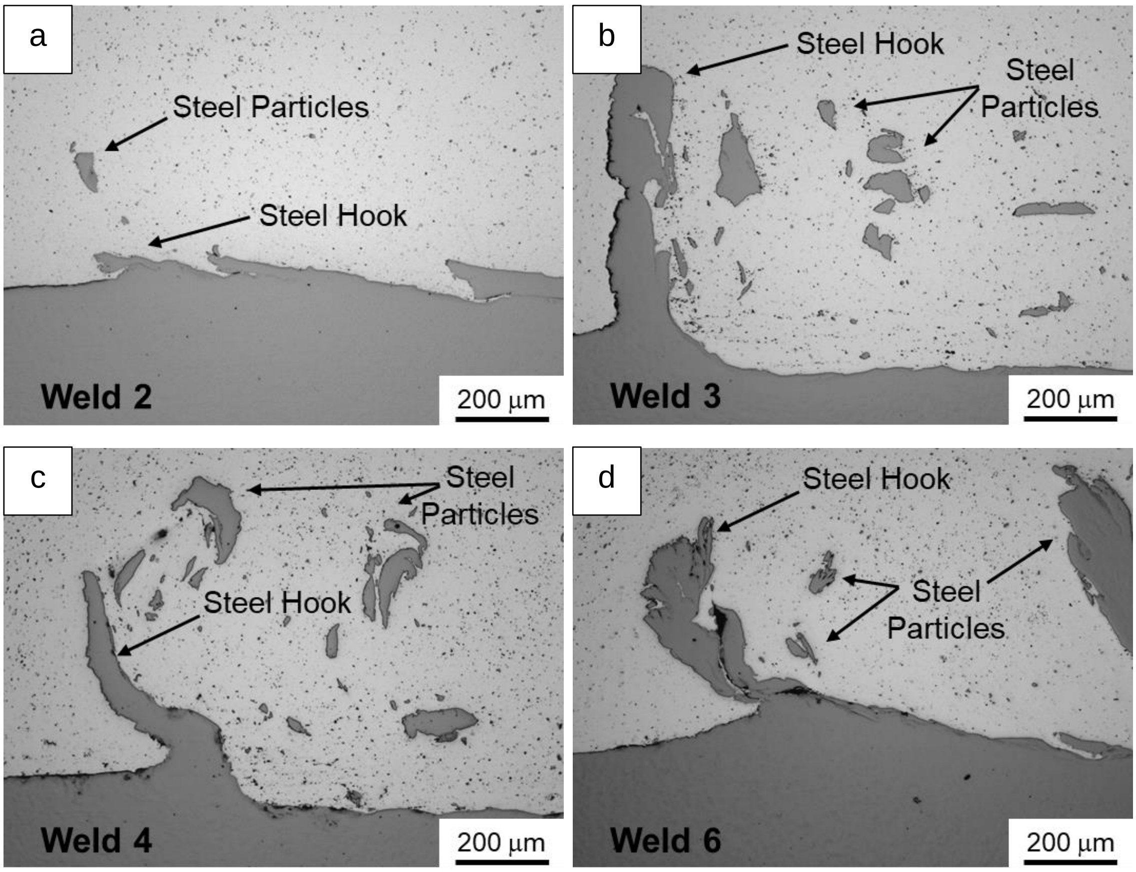
a
Steel Particles
Steel Hook
Weld 2
200 µm
b
Steel Hook
Steel
Particles
Weld 3
200 µm
c
Steel
Particles
Steel Hook
Weld 4
200 µm
d
Steel Hook
Steel
Particles
Weld 6
200 µm

Figure 5.7 – Steel hook and particles present in the joints produced using welding speed and rotational speed of (a) 5 mm/s and 500 rpm, (b) 5 mm/s and 700 rpm, (c) 5 mm/s and 900 rpm, (d) 7 mm/s and 700 rpm.

Both steel particles and steel hook are formed due to the aluminum flow and scratching action of the probe on the steel surface. During the process, the higher temperatures resulted from the frictional heating promoted by the shoulder reduces the flow stress in the upper region of the weld, which causes the downward movement of material. To occupy the space left on top of the weld, the materials on the bottom flows upward (counter-flow) under the action of the tool pressure, resulting in the deformation of the steel and formation of the steel hook within the aluminum weld zone, with the contribution of the scratching and deformation action of the probe on the steel surface [85]. Besides that, steel particles are detached from the steel surface by the probe contact and the aluminum downward flow, which is pressed against the steel surface as a result of the threaded probe rotation, and are dragged upwards due to the counter-flow of the softened aluminum [10].

These macrostructure features are present in all the joints, although it was more evident in the welds produced using low welding speed and high rotational speed. In these cases, the energy input per unit length was increased, consequently increasing the plastic deformation and mixing of materials, and resulting in the detachment of more steel particles, and a more evident steel hook. The tendency to increase the height of the steel hook with welding speed decrease and rotational speed increase can be seen in Table 5.2, where is presented the average steel hook height for each welding parameter, measured in relation to the original interface between aluminum and steel plates. According to Xiong et al. [90], the height of the steel hook is decreased with the increasing of welding speed as a consequence of the inversely proportional relationship between welding speed and energy input.

Table 5.2 – Average steel hook height for welds produced using different welding speeds and rotational speeds.

Welding Speed (mm/s)	**Rotational Speed (rpm)**	**Steel Hook Height (μm)**	**Welding Speed (mm/s)**	**Rotational Speed (rpm)**	**Steel Hook Height (μm)**
5	300	342 ± 14	13	700	243 ± 21
5	500	96 ± 9	15	700	117 ± 28
5	700	605 ± 35	7	900	63 ± 13
5	900	463 ± 31	9	900	271 ± 42
5	1100	477 ± 68	11	900	79 ± 7
7	700	500 ± 68	13	900	124 ± 19
9	700	714 ± 33	15	900	121 ± 14

Finally, for high rotational speed, as used to produce the weld 5 (5 mm/s and 1100 rpm), a lamellar structure of aluminum and steel was formed in the weld interface, with cracks within the layers, as presented in Figure 5.4, and shown in detail in Figure 5.8. This lamellar structure occurred due to the different plastic deformability of the aluminum and steel, which resulted in the formation of microcracks in the steel surface due to its low ductility compared to the aluminum at the welding temperature. The creation and stretching of more microcracks made possible the flow of aluminum into these cracks and its reaction with steel [90]. The cracks present in the lamellar structure can be a result of its incomplete filling, or the formation of thick Intermetallic Compound (IMC) layers in the interface, which can initiate microcracks due to the rapid temperature cooling [92] and different thermal contraction compared to the steel and aluminum. As already mentioned, this weld presented the highest average energy input per unit length among the process parameters studied, which facilitates the mixture and interdiffusion of aluminum and iron, forming the IMC layers.

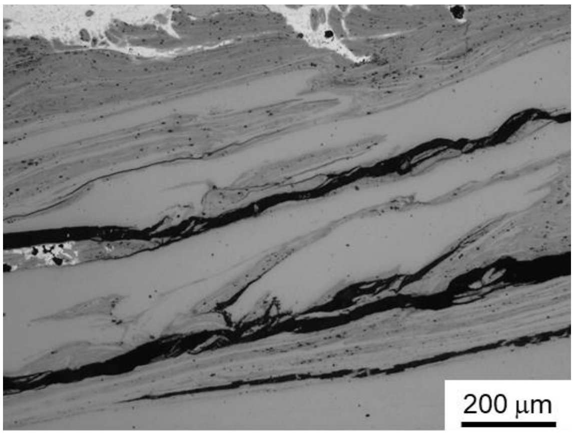

Figure 5.8 – Lamellar structure with cracks inside formed at the interface of the weld 5, produced using a welding speed of 5 mm/s and rotational speed of 1100 rpm.

In resume, sound joints, without voids and defects, were produced using low welding speed (5 mm/s and 7 mm/s) and intermediate rotational speed (500 rpm, 700 rpm, and 900 rpm). These welds presented steel hook with higher height and more steel particles dispersed in the aluminum weld zone, due to the higher plastic deformation and mixing of materials. Increasing the welding speed (between 9 mm/s and 15 mm/s) or decreasing the rotational speed (300 rpm) caused the insufficient aluminum flow due to the decrease of the energy input per unit length, resulting in scattered voids or tunnel defects in the macrostructure of the welds. Furthermore, the increase of the rotational speed (1100 rpm) caused the formation of flashes in the weld surface, and a lamellar structure in the weld interface, with cracks inside, due to the different plastic deformability between the aluminum and steel, and the highest energy input per unit length.

5.3 Microstructural Characterization

The microstructure of the joints was characterized by the weld zones shown in the representative cross-section in Figure 5.9 of the weld 3, produced using a welding speed of 5 mm/s and a rotational speed of 700 rpm. These weld zones are the Base Material (BM), Heat Affected Zone (HAZ), and Thermo-Mechanically Affected Zone (TMAZ) in the aluminum and steel, and the Stir Zone (SZ) in the aluminum part. This is a typical microstructure observed in dissimilar aluminum/steel joints produced by FSW in the lap joint configuration, as already reported in the literature [39]. The cross-section microstructure of the welds can be found in Appendix C for each welding condition studied. The steel hook and steel particles dispersed in the aluminum matrix were corroded during the etching of the aluminum alloy, which resulted in their appearance as black voids in the cross-section microstructure of the welds. Because of this, the steel and steel hook microstructures were analyzed separated, as will be shown forward in this section.

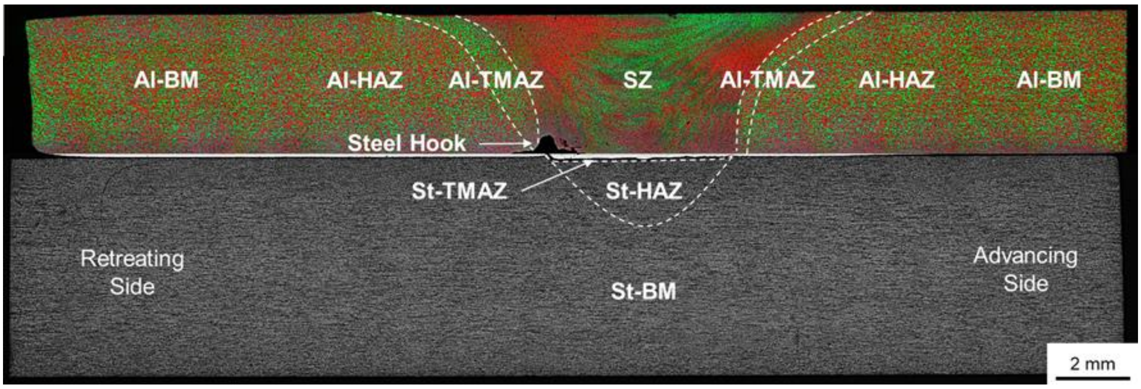

Figure 5.9 – Microstructure of the weld 3, produced using a welding speed of 5 mm/s and rotational speed of 700 rpm, and weld zones.

The microstructure of the AA5083-O/H111 BM is characterized by slightly elongated grains in the rolling direction, with an average grain size of 35.0 ± 0.2 μm (Figure 5.10a). This is the original microstructure of the aluminum alloy, which resulted in the microstructure of the weld zones when affected by the temperature and plastic deformation during the welding. Located next to the Al-BM, the Al-HAZ (Figure 5.10a), which experienced just the thermal cycle, presents a microstructure similar to Al-BM. Between the Al-HAZ and Al-SZ, the Al-TMAZ (Figure 5.10b and c) was affected by both thermal cycle and plastic deformation, resulting in deformed and elongated grains. The Al-SZ (Figure 5.10d), which was severe plastic deformed and experienced the thermal cycle during the welding, is characterized by fine and equiaxed grains dynamically recrystallized. This zone also contains the plastic deformed steel particles detached from the steel surface.

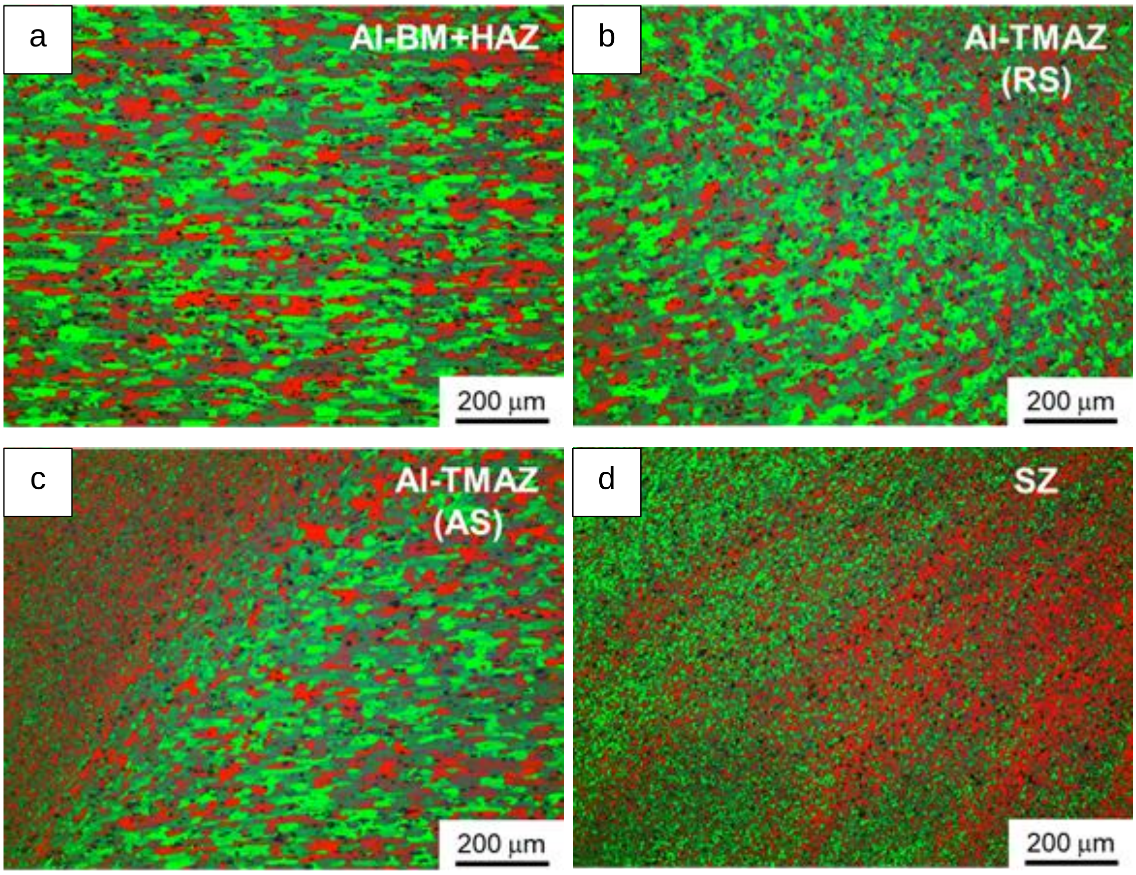

Figure 5.10 – (a) Aluminum BM and HAZ, (b) aluminum TMAZ on the RS, (c) aluminum TMAZ on the AS, and (d) aluminum SZ, in the weld 3, produced using a welding speed of 5 mm/s and rotational speed of 700 rpm.

However, the welds present asymmetries between the microstructure on the AS and RS, due to the simultaneous rotation and translation movement of the tool, typically observed in FSW joints [93]. As can be seen in Figure 5.10, and specified in Figure 5.11, the transition from the TMAZ to the SZ is more abrupt on the AS than on the RS, as a consequence of opposite welding direction and tool rotation on the RS of the weld, which generates wider thermal field and complex strain gradients than on the AS [93-94].

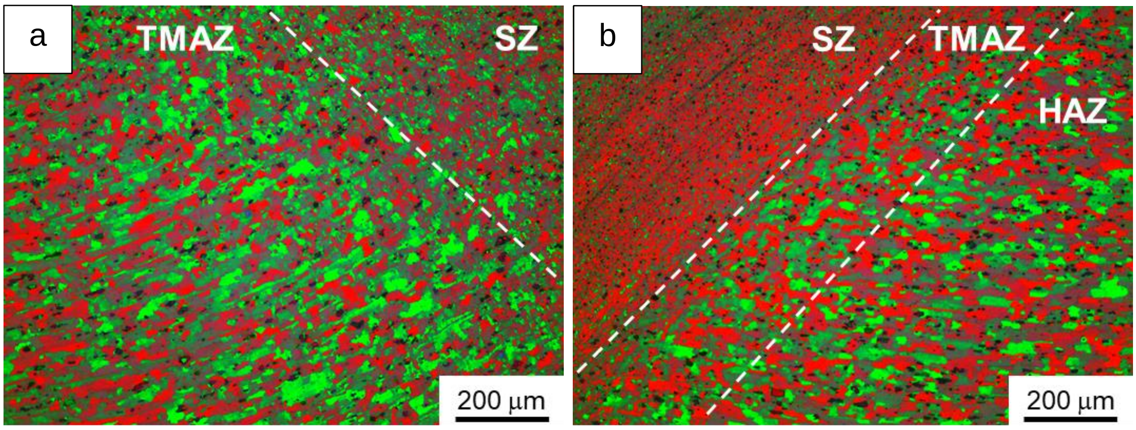

Figure 5.11 – Transition in the microstructure from the TMAZ to the SZ on the (a) RS, and (b) AS of the weld 8 (13 mm/s and 700 rpm).

Additionally, due to the asymmetric material flow during the welding, the microstructure in the Al-SZ presents variations in the grain size. As reported in the literature [10-11], the aluminum grain size is slightly smaller at the top of the weld due to the increase of the shear stress exerted by the shoulder in this region, and slightly coarser near the interface, because of the heat generated by the friction between the probe and the steel surface. These variations in the grain size in the Al-SZ could not be identified clearly in the welds being studied, but, as can be seen in the yellow-marked region in Figure 5.12, slightly coarser grains could be observed near the transition to the Al-TMAZ, especially on the RS. This phenomenon is more visible at high rotational speed and may be related to the complex strain gradient and thermal field on the RS.

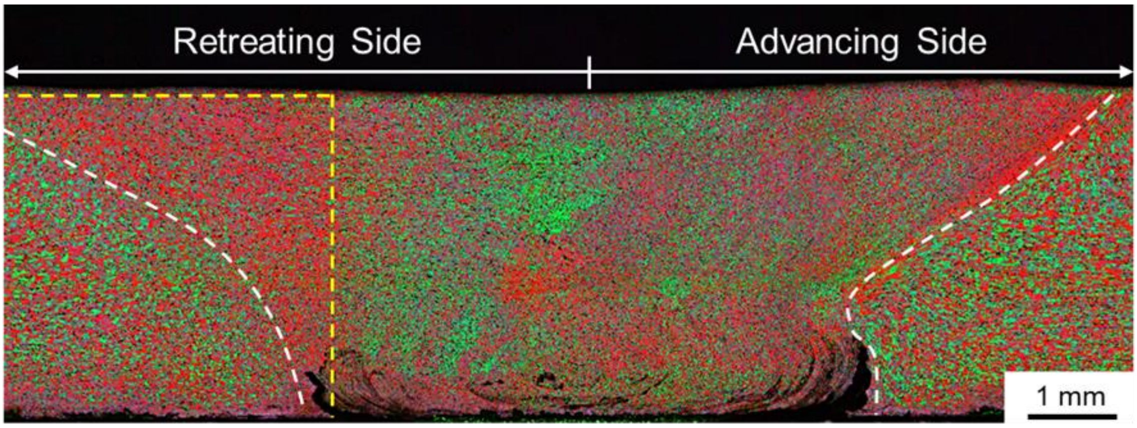

Figure 5.12 – Microstructure of the Al-SZ of the weld 5 (5 mm/s and 1100 rpm).

The evolution of the AA5083 SZ microstructure was investigated by Yazdipour et al. [95] during Friction Stir Processing (FSP), which is a technique for modifying and refine the microstructure of materials with the same basic principles as FSW. They stated that the fine grains formed in the SZ are a result of Dynamic Recovery (DRV) and Continuous Dynamic Recrystallization (CDRX) occurring during the process. Despite the high Stacking-Fault Energy (SFE) of the aluminum, the strain, the presence of second phase particles, such as $Al_6(Mn,Fe)$ in case of AA5083, and/or alloying elements interferes in the DRV. This allows the formation of fine grains by the coalescence and rotation of the subgrains structure with high misorientation during the CDRX, which experience grain growth after the end of the severe plastic deformation. Thus, the final grain size in the Al-SZ is affected by the energy input and cooling rate.

In this way, both rotational speed and welding speed affects the final grain size in the Al-SZ, as shown in Figure 5.13 and Table 5.3 for the welds studied. The increase of the rotational speed or decrease of the welding speed caused the increase in the average grain size in the Al-SZ. Increasing the rotational speed (Figure 5.13a and Figure 5.13b) results in the increase of the energy input, and hence in the temperature of the process, which causes grain growth. Similarly, decreasing the welding speed (Figure 5.13c and Figure 5.13d) not only increases the energy input per unit length but also increases the time available for grain growth. The maximum average grain size in the Al-SZ was 15.64 μm, achieved in the weld 5 (5 mm/s and 1100 rpm), and the minimum was 4.04 μm, achieved in the weld 1 (5 mm/s and 300 rpm). Increasing the welding speed from 5 mm/s to 15 mm/s, the average grain size in the Al-SZ decreased from 8.61 μm to 6.99 μm, keeping a constant rotational speed of 700 rpm, and decreased from 12.70 μm to 8.53 μm, keeping a constant rotational speed of 900 rpm.

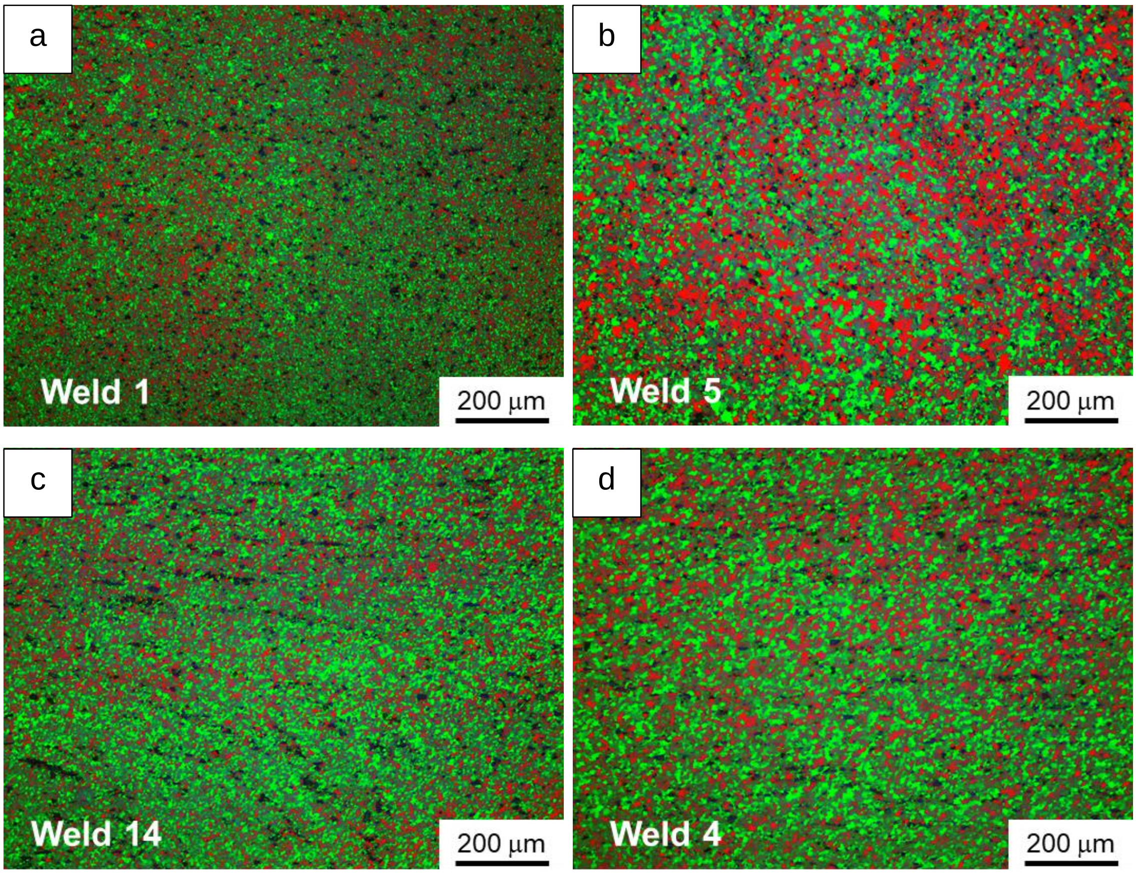

Figure 5.13 – Grain size variation in the Al-SZ of the welds produced using welding speed and rotational speed of (a) 5 mm/s and 300 rpm, (b) 5 mm/s and 1100 rpm, (c) 15 mm/s and 900 rpm, and (d) 5 mm/s and 900 rpm.

Table 5.3 – Average grain size for welds varying welding speed and rotational speed.

Welding Speed (mm/s)	**Rotational Speed (rpm)**	**Average Grain Size (μm)**	**Welding Speed (mm/s)**	**Rotational Speed (rpm)**	**Average Grain Size (μm)**
5	300	4.04 ± 0.01	13	700	7.47 ± 0.03
5	500	7.60 ± 0.02	15	700	6.99 ± 0.01
5	700	8.61 ± 0.02	7	900	11.12 ± 0.03
5	900	12.70 ± 0.04	9	900	10.01 ± 0.02
5	1100	15.64 ± 0.03	11	900	9.83 ± 0.02
7	700	8.11 ± 0.02	13	900	9.33 ± 0.03
9	700	8.06 ± 0.03	15	900	8.53 ± 0.03

On the other side of the weld, the microstructure of the GL D36 steel BM (Figure 5.14a) is characterized by slightly elongated ferrite grains, resulting from the rolling process, and perlite on the grain boundaries, with a homogenous grain size of about 10.99 ± 0.05 μm. Metallurgical changes were not observed in the steel, such as the formation of bainite and martensite, in view that its melting point is higher than of the aluminum alloy, and that the probe just scratched the steel surface and was not inserted in the steel plate, which would increase the strain and temperature during the welding. Accordingly, the St-HAZ (Figure 5.14a), which was affected only by the thermal cycle, presents a microstructure similar to St-BM. In contrast, the St-TMAZ (Figure 5.14b) presents deformed grains, resulting from the severe plastic deformation and friction heating experienced during the welding.

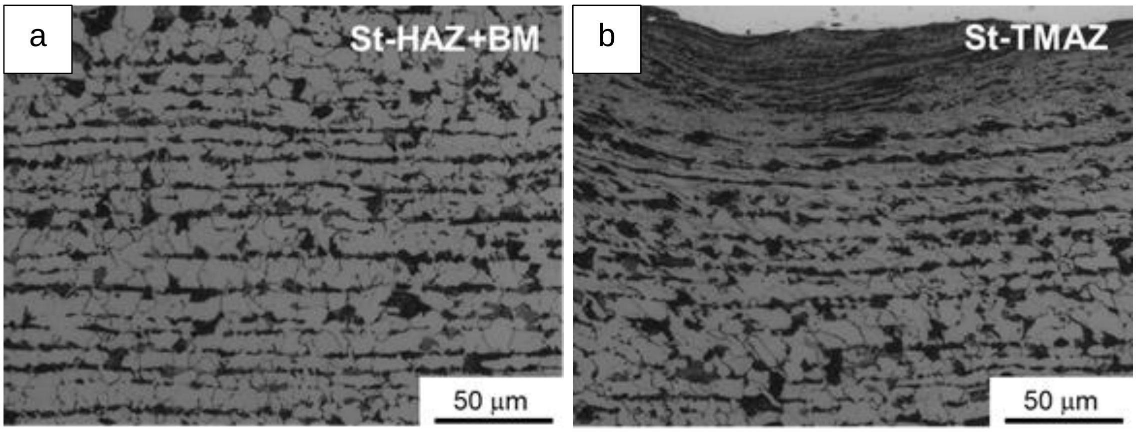

Figure 5.14 – (a) Steel BM and HAZ, and (b) steel TMAZ, in the weld 3, produced using a welding speed of 5 mm/s and rotational speed of 700 rpm.

The influence of the welding speed and rotational speed on the St-TMAZ is shown in Figure 5.15. The depth of the St-TMAZ showed a tendency to increase with the increase of the rotational speed and welding speed. The increase of the rotational speed (Figure 5.15a and Figure 5.15b) caused the energy input increases, resulting in the improvement of the material flow and plastic deformation of the aluminum alloy and steel. In turn, increasing the welding speed (Figure 5.15a and Figure 5.15c), in spite of reducing the energy input per unit length, resulted in a shortening welding time available for plastic deformation, making the frictional heating and strain concentrates in a deeper region of the St-TMAZ with a smaller width at the welded interface.

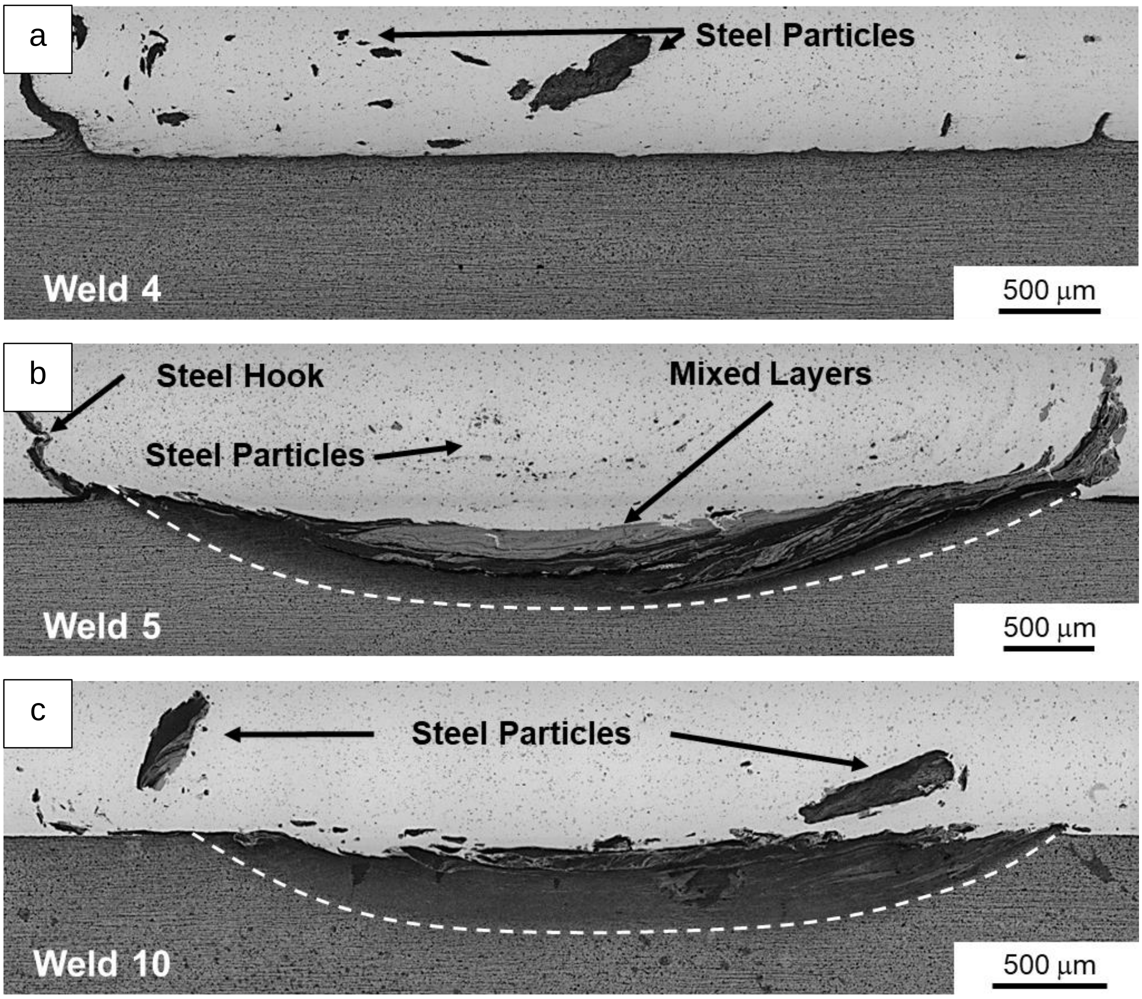
a
Steel Particles
Weld 4
500 µm
b
Steel Hook
Mixed Layers
Steel Particles
Weld 5
500 µm
c
Steel Particles
Weld 10
500 µm

Figure 5.15 – Microstructure of the St-TMAZ of the welds produced using a welding speed and rotational speed of (a) 5 mm/s and 900 rpm, (b) 5 mm/s and 1100 rpm, and (c) 7 mm/s and 900 rpm.

Studying dissimilar aluminum to steel lap joints, Wan et al. [17] also reported the presence of a region composed of fine and dynamically recrystallized grains in the steel near the weld interface. As they reported, the decrease of the rotational speed and increase of the welding speed resulted in smaller grain size in this region, due to the decrease of the energy input and strain rate.

In addition, another characteristic of the St-TMAZ was the presence of mixed layers of steel and aluminum at the weld interface, as shown in Figure 5.15b. This structure is formed due to the high local temperatures resulting from the frictional heating, and high axial pressures, which forces the softened aluminum against the steel surface, accelerating the diffusion process and leading to metallurgical bonding between the aluminum alloy and steel. A similar discussion was approached by Coelho et al. [10], relating the formation of IMCs in these mixed layers. Among the parameters investigated in this study, these mixed layers were more evident in the weld 5, produced with the highest rotational speed (1100 rpm), and consequently, the highest energy input and plastic deformation.

However, as exemplified in Figure 5.16 for the weld 13, produced using welding speed of 13 mm/s and rotational speed of 900 rpm, the welds that presented tunnel defects in the macrostructure did not follow the tendency to increase the depth of the St-TMAZ increasing the welding speed and rotational speed, as described previously. This break in the tendency may be related to the inefficient material flow due to the insufficient energy input per unit length and plastic deformation, which results in smaller heating and strain at the steel near the weld interface, and consequently, shallow and superficial St-TMAZ.

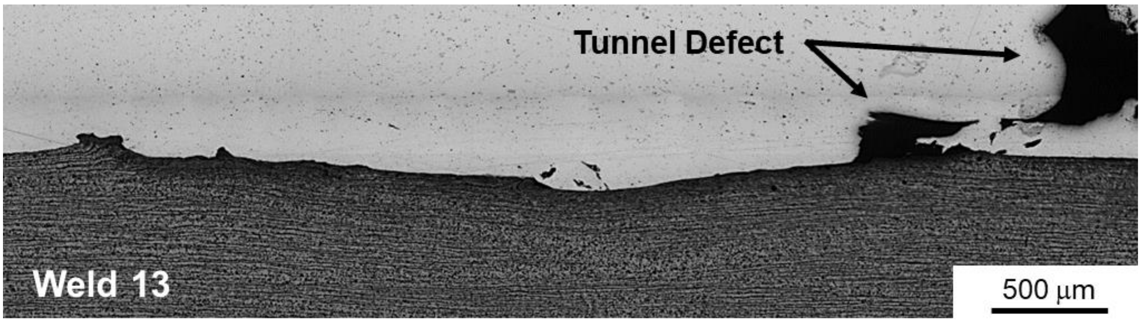

Figure 5.16 – Microstructure of the St-TMAZ of the weld 13, produced using a welding speed of 13 mm/s and rotational speed of 900 rpm.

Last, the steel hook and dispersed steel particles also presented a microstructure with deformed grains, similar to St-TMAZ, as shown in Figure 5.17, as a consequence of the severe plastic deformation and heating experienced at the weld interface due to the friction action of the probe, and the aluminum flow. The steel particles dispersed in the Al-SZ presented mixed layers of aluminum and steel, as well as observed in the St-TMAZ.

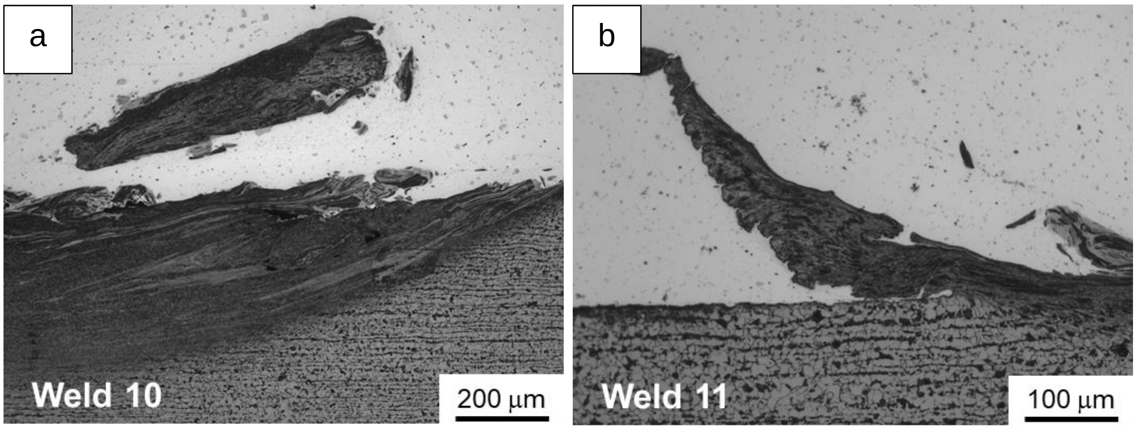

Figure 5.17 – Microstructure of the (a) dispersed steel particles, and (b) steel hook, at the weld interface.

In short, the FSW process significantly reduced the grain size in the weld zone, refining from around 35 μm in the Al-BM to a minimum of 4.04 μm in the SZ of the weld with a welding speed of 5 mm/s and a rotational speed of 300 rpm, produced with the lowest energy input per unit length. The decrease of the welding speed and increase of the rotational speed caused the coarsening of the grain size in the Al-SZ, which achieved a maximum grain size of 15.64 μm in the SZ of the weld with a welding speed of 5 mm/s and a rotational speed of 1100 rpm. In the steel, a tendency to a deeper and less wide St-TMAZ was observed with the increase of the welding speed and rotational speed.

5.4 Interface Characterization

The sufficient energy input during the welding leads to the metallurgical bonding between aluminum and steel, with the formation of IMC layers at the interface, which can be thicker depending on the heating and plastic deformation during the process. Thick IMC layers may turn the welds more brittle, resulting in the decrease of the joint strength [92]. Because of this, IMCs have been commonly identified in aluminum to steel FSW lap welds [10-11, 13-14, 16-17, 87, 89-90, 92, 96], and the understanding of the effects of the process parameters, welding speed and rotational speed in this case, on the IMC layer, are important.

Continuous IMC layers throughout the entire interface between aluminum and steel were identified in the welds 3 (5 mm/s and 700 rpm), 7 (9 mm/s and 700 rpm), and 11 (9 mm/s and 900 rpm), as shown in Figure 5.18, where is presented the results obtained by Scanning Electron Microscopy (SEM) equipped with Energy Dispersive X-Ray Spectroscopy (EDS). The average thickness of these layers increased from 250 ± 40 nm to 400 ± 70 nm, increasing the welding speed from 5 mm/s (weld 3, Figure 5.18a) to 9 mm/s (weld 7, Figure 5.18b), and keeping a constant rotational speed of 700 rpm. Increasing the rotational speed from 700 rpm (weld 7, Figure 5.18b) to 900 rpm (weld 11, Figure 5.18c), and keeping a constant welding speed of 9 mm/s, the IMC thickness increased from around 400 ± 70 nm to 800 ± 170 nm. Higher magnifications than that showed in Figure 5.18 were used for those measurements, as can be seen in Appendix D for each welding condition studied.

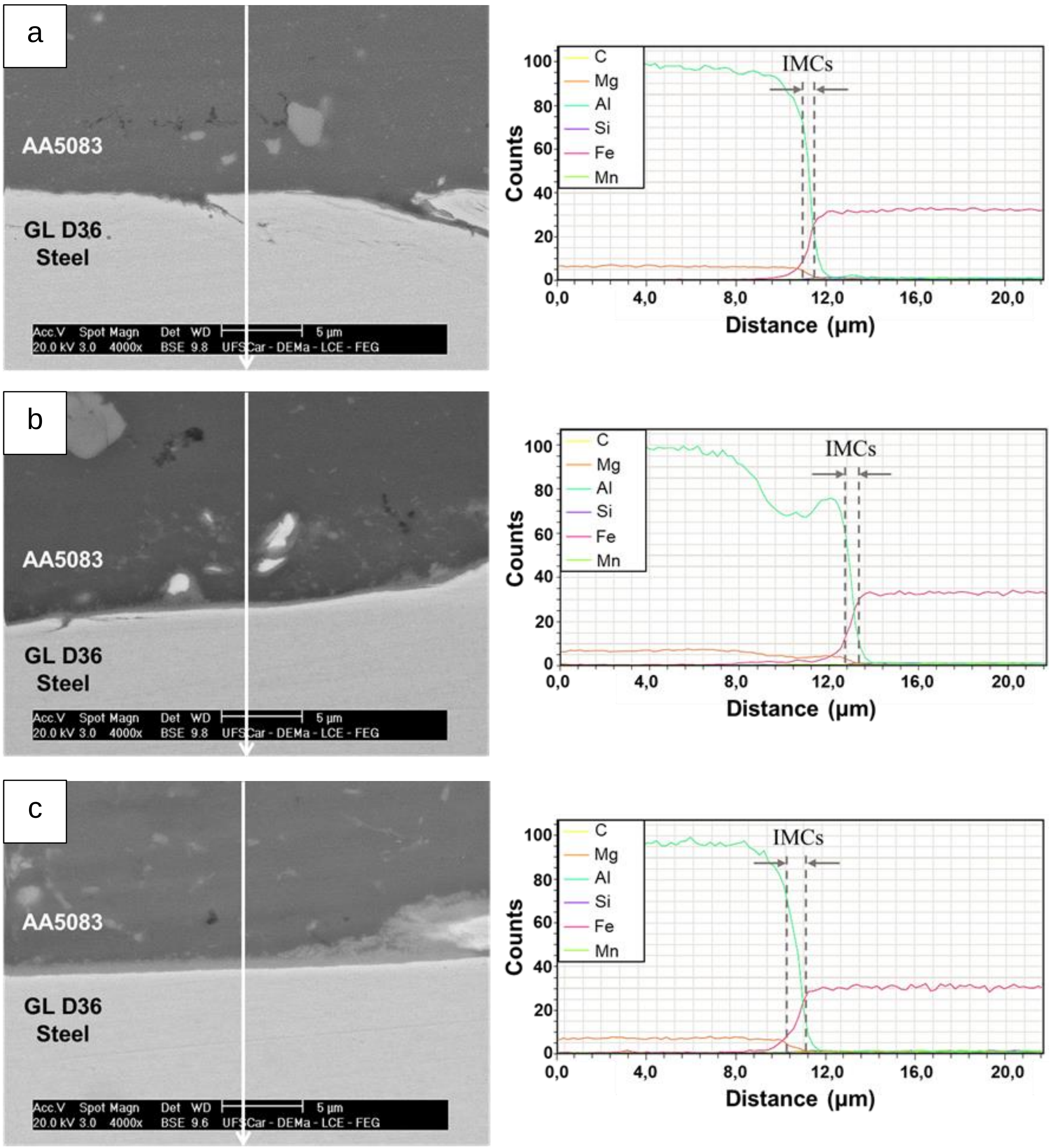

Figure 5.18 – SEM backscattered micrograph and EDS line scan results of the interface of joints produced using welding speed and rotational speed of (a) 5 mm/s and 700 rpm, (b) 9 mm/s and 700 rpm, and (c) 9 mm/s and 900 rpm.

The formation and growth of IMC layers are affected by the energy input and plastic deformation at the weld interface, as discussed by Wan et al. [17]. The thicker IMC layer observed when the rotational speed increased, was a consequence of the higher energy input that allows its diffusional growth, which was also reported by Kimapong et al. [96] in investigations of dissimilar AA5083/SS400 steel FSW lap welds. Additionally, they reported the decrease in the IMC thickness increasing the welding speed, due to the lower energy input per unit length and plastic deformation. Nevertheless, the contrary occurred in the welds investigated in Figure 5.18, where the IMC thickness increased with the increase of the welding speed, despite the lower energy input per unit length, as shown in Figure 5.2. This may be related to the shorter welding time when the welding speed is increased, which reduces the time available for mixing and plastic deformation, resulting in the concentration of the welding energy in the IMC growth, as reported by Pourali et al. [89]. In this case, when the welding speed was increased from 5 mm/s (weld 3, Figure 5.18a) to 9 mm/s (weld 7, Figure 5.18b), the plastic deformation consumed the least amount of welding energy, resulting in thicker IMC layer, and fewer steel particles detached and dispersed in the Al-SZ. The amount of steel particles dispersed on the RS of the welds 3 and 7 can be seen in the macrostructures of Figure 5.4c and Figure 5.6a, respectively.

In addition, the detachment of steel particles from the steel surface contributes to the lowering thickness of the IMC layer, since these layers are detached and dispersed in the Al-SZ with the steel fragments. Thus, when the welding speed is decreased, higher is the time available for plastic deformation near the steel surface and consequently more steel fragments are detached and dispersed in the Al-SZ, resulting in the continuous breaking of the IMC layer at the weld interface during the welding, and thinner IMC layer after the process.

The difference of the influence of the welding speed in the IMC thickness in the results obtained for the welds investigated in this study and the results of the literature [96] mentioned above can be related to the influence of other process parameters on the energy input and plastic deformation during welding. For example, to investigate the influence of the welding speed and rotational speed on the IMC thickness, Kimapong et al. [96] used a fixed probe depth of 0.1 mm in the steel plate, while the axial force was fixed (load control process) in the present study, instead of the probe depth. The load control process resulted in the achievement of the maximum axial force with a slight probe penetration in the steel plate in the welds being studied, in view that higher axial force is necessary for the probe penetrates the steel plate due to its higher melting point and mechanical properties than the aluminum alloy. Moreover, Kimapong et al. [96] showed that the increase in the probe depth results in the increase of the IMC thickness, as a consequence of the higher shear stress that generates a higher energy input and temperatures. Therefore, when the probe penetrates the steel plate, the welding energy becomes more significant for the IMC growth than for the plastic deformation at the weld interface, and because of this, the increase of the welding speed results in the thinner IMC layers due to the reduction of the energy input. On the contrary, when the probe only scratches the plate surface, as in the present work, the plastic deformation becomes significant at the weld interface, and the thickness of the IMC layers decreases when the time available for plastic deformation is longer, as discussed previously.

Not only the probe depth but also the probe geometry can influence the relationship between the welding speed and IMC thickness. In the study conducted by Kimapong et al. [96], a non-threaded probe was used in the FSW, which results in higher heat generation to soften the steel, as reported by Xiong et al. [90]. As a consequence, the plastic deformation at the interface is restricted, and the welding energy is concentrated on heating with the growth of the IMC layer, similarly to when the probe depth increases.

Anyway, independent of the influence of the welding parameters on the IMC thickness, the welds investigated by EDS presented a distribution of the elements at the interface as shown in Figure 5.19 for the welds 3 (5 mm/s and 700 rpm), 7 (9 mm/s and 900 rpm), and 11 (9 mm/s and 900 rpm). The EDS chemical maps show a mixture of Al and Fe atoms in the IMC layer, confirming their interdiffusion across the weld interface. This interdiffusion of Al and Fe atoms and the formation of IMC layers also can be seen around the steel fragments, as shown in Figure 5.19b, formed due to the severe plastic deformation experienced during welding. Besides that, IMC fragments can be observed dispersed in the aluminum alloy, as shown in Figure 5.19a, which were removed from the interface by the friction and plastic deformation during welding, and dragged by the aluminum flow. Both steel particles and IMC fragments present small quantities of Mg, Mn, Si, and C elements.

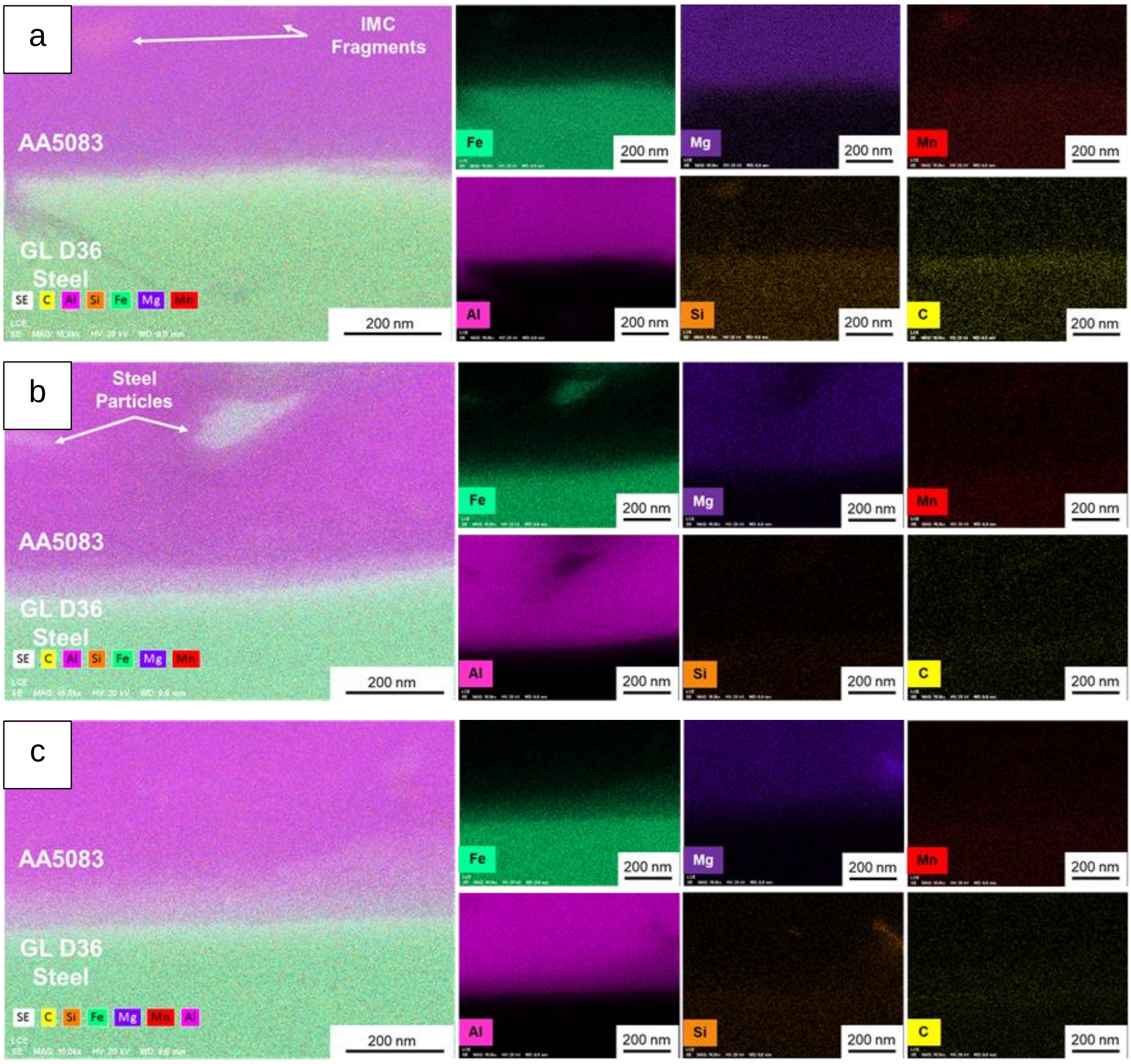
a
IMC Fragments
AA5083
GL D36 Steel
SE C Al Si Fe Mg Mn
200 nm
Fe
Mg
Mn
Al
Si
C
b
Steel Particles
AA5083
GL D36 Steel
SE C Al Si Fe Mg Mn
200 nm
c
AA5083
GL D36 Steel
SE C Si Fe Mg Mn Al
200 nm

Figure 5.19 – EDS chemical maps of the IMC layer showing the Fe, Mg, Mn, Al, Si, and C elements at the interface of the welds produced using a welding speed and rotational speed of (a) 5 mm/s and 700 rpm, (b) 9 mm/s and 700 rpm, and (c) 9 mm/s and 900 rpm.

Another constituent of the welds interface can be observed in Figure 5.19c, with the concentration of Mg, Si, Al, and Fe elements, which may correspond to β phase precipitates (Al_3Mg_2) and Al_6(Mn,Fe)Si dispersoids. The β precipitates tend to be formed on/near the dispersoids in severe plastically deformed materials, and due to its preferential dissolution, lead to intergranular corrosion in harsh environments, and then, result in problems especially for the marine industry [97-98].

The phase formation in the interface of the weld 3 (5 mm/s and 700 rpm) was investigated by X-Ray Diffraction (XRD), and the result is presented in Figure 5.20. Besides the identification of the α-Fe and Al phases from the BM, the IMC Fe_3Al and FeAl phases, present around the steel particles dispersed in the Al-SZ and at the weld interface, were identified. These Fe-rich phases have already been reported in dissimilar Al/Fe FSW lap joints [17, 89], and as mentioned in the literature review, they are less brittle than the Al-rich phases, present good corrosion resistance, and can be used as structural materials.

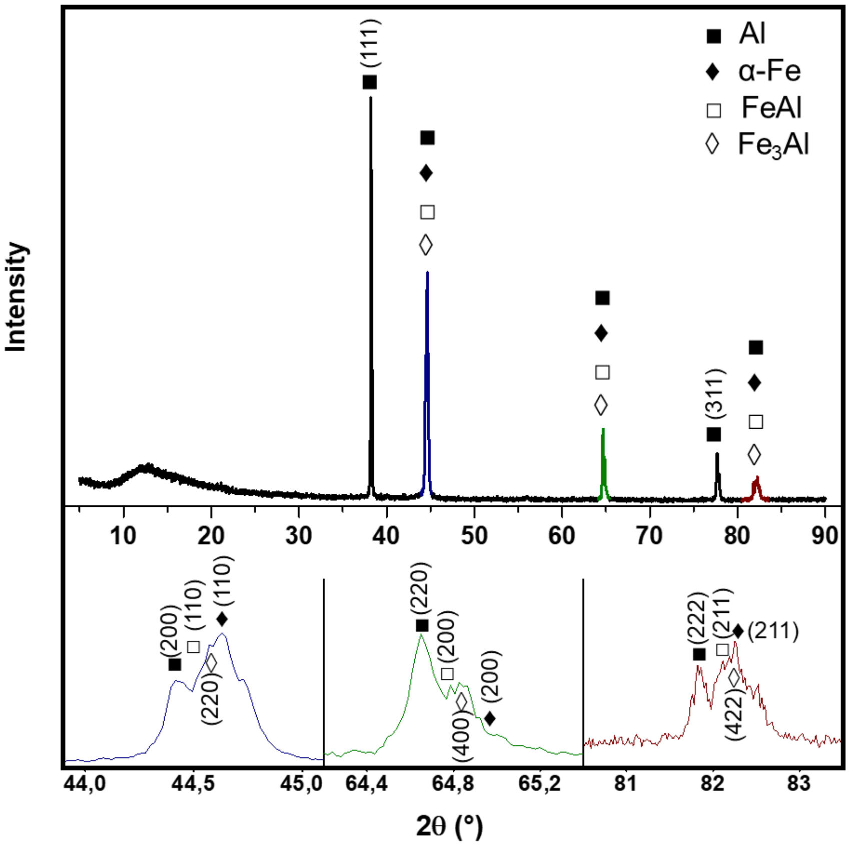

Figure 5.20 – XRD pattern from the interface of the weld 3 produced using a welding speed of 5 mm/s and a rotational speed of 700 rpm.

The FeAl is stable at Al contents ranging from 23 at.% to 55 at.% and reported to be formed at around 1300°C through a peritectic reaction, whereas Fe_3Al is stable at Al contents ranging from 23 at.% to 34 at.% and formed through the first-order reaction of the FeAl phase at about 550°C under atmospheric pressure [35, 85]. Their formation at the lower FSW temperatures occurs due to high pressure and severe plastic deformation during the process, which enhances the diffusion and the IMC nucleation and growth.

During the FSW process, a tongue-like morphology was formed in the interface between the iron substrate and the intermetallic layer, identified by the steel peaks towards the IMC layer in Figure 5.21. This wave feature has already been reported in investigations of the formation of IMC layers by diffusion experiments [99-101] and is attributed to anisotropic diffusion (high vacancy concentration in certain crystallographic direction). About the IMC growth, a study reported [101] that the IMC layer grows preferentially towards the aluminum alloy, with a slightly grown into the steel, compared to the original interface.

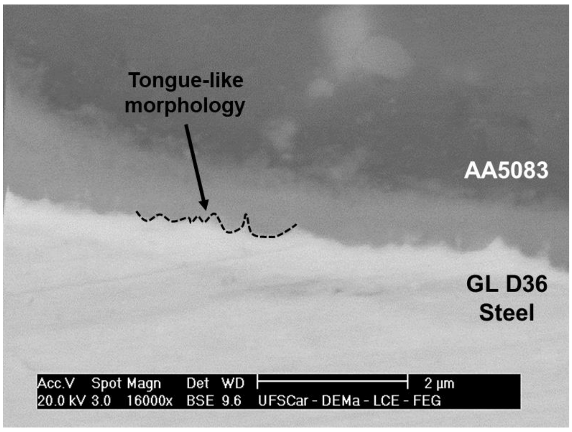
Tongue-like morphology
AA5083
GL D36 Steel
Acc.V Spot Magn Det WD 2 µm
20.0 kV 3.0 16000x BSE 9.6 UFSCar - DEMa - LCE - FEG

Figure 5.21 – Tongue-like morphology in the interface of SEM backscattered micrograph of the weld 11 produced using a welding speed of 9 mm/s and rotational speed of 900 rpm.

Additionally, some micro interlocks were observed in the weld interface, as shown in Figure 5.22, produced due to the difference in the plastic deformability between aluminum and steel. The higher melting point and lower ductility of the steel compared to the softened aluminum resulted in an increase in the surface roughness and microcracks in the steel surface during the welding process, which were filled by the aluminum flow, forming micro interlocks with the reaction between aluminum and steel in the weld interface.

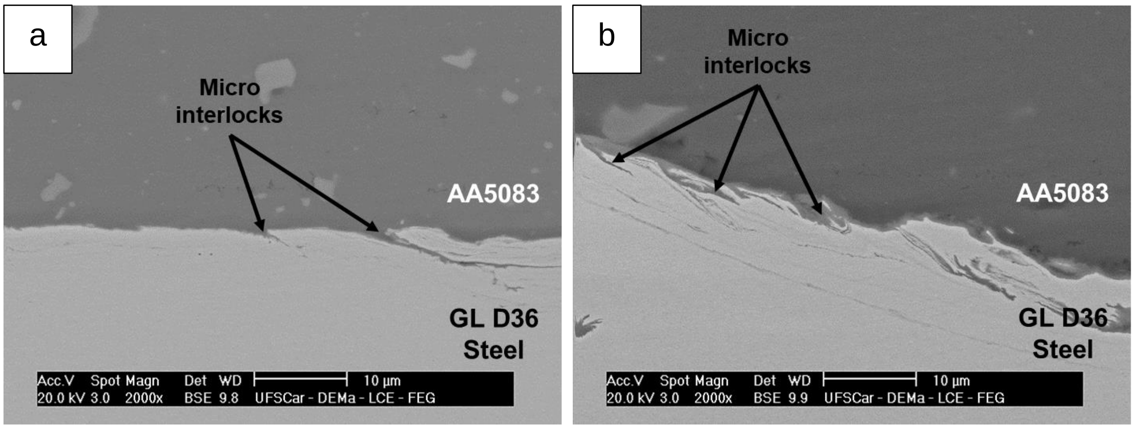
a
Micro
interlocks
AA5083
GL D36
Steel
Acc.V Spot Magn Det WD 10 µm
20.0 kV 3.0 2000x BSE 9.8 UFSCar - DEMa - LCE - FEG
b
Micro
interlocks
AA5083
GL D36
Steel
Acc.V Spot Magn Det WD 10 µm
20.0 kV 3.0 2000x BSE 9.9 UFSCar - DEMa - LCE - FEG

Figure 5.22 – Micro interlocks in SEM backscattered micrographs of the interface of welds produced using welding speed and rotational speed of (a) 5 mm/s and 700 rpm, and (b) 9 mm/s and 700 rpm.

On the whole, the FSW process resulted in continuous Intermetallic Compound (IMC) layers throughout the entire interface of the welds, composed of FeAl and Fe_3Al Fe-rich phases. The average thickness of these layers increased with the increasing of the welding speed and rotational speed, as a consequence of the improvement of the energy input per unit length and plastic deformation. Thinner IMC layers with an average thickness of about 250 nm were observed in the interface of the weld with a welding speed of 5 mm/s and a rotational speed of 700 rpm, which increased to an average thickness of about 800 nm in the interface of the weld 11 with a welding speed of 9 mm/s and a rotational speed of 900 rpm. In addition, the different plastic deformability between the aluminum and steel resulted in micro interlocks in the weld interface.

5.5 Mechanical Characterization

5.5.1 Hardness Tests

Microhardness measurements were carried out horizontally along the cross-section of the welds, and in the vertical direction perpendicularly to the weld interface, in order to evaluate the variation of the mechanical properties along the different weld zones, and to investigate the effects of the welding speed and rotational speed on the microhardness of the welds.

The horizontal microhardness profile along the cross-section of the aluminum alloy part of the welds is shown in Figure 5.23. These measurements were produced at 1 mm of distance from the weld interface, and as can be seen, the weld zones can be identified by their microhardness values. The AA5083-O/H111 BM presents hardness values of around 86 $HV_{0.2}$ that is determined by the grain size. Since the Al-HAZ presented similar microstructure to Al-BM, was not observed a significant difference in the microhardness values of these regions. In the Al-TMAZ the microhardness increased gradually, due to the presence of deformed and elongated grains. In general, the microhardness values in the Al-TMAZ is lower than in the Al-SZ since the energy input and plastic deformation in the Al-TMAZ was not enough to cause dynamic recrystallization and reduce the grain sizes and is higher on the AS, due to the higher strain and thermal gradients, than on the RS. The Al-SZ presents higher microhardness values due to the presence of equiaxial and fine dynamically recrystallized grains. Some peaks in the microhardness profile may be related to the measurement near fine steel particles with high microhardness.

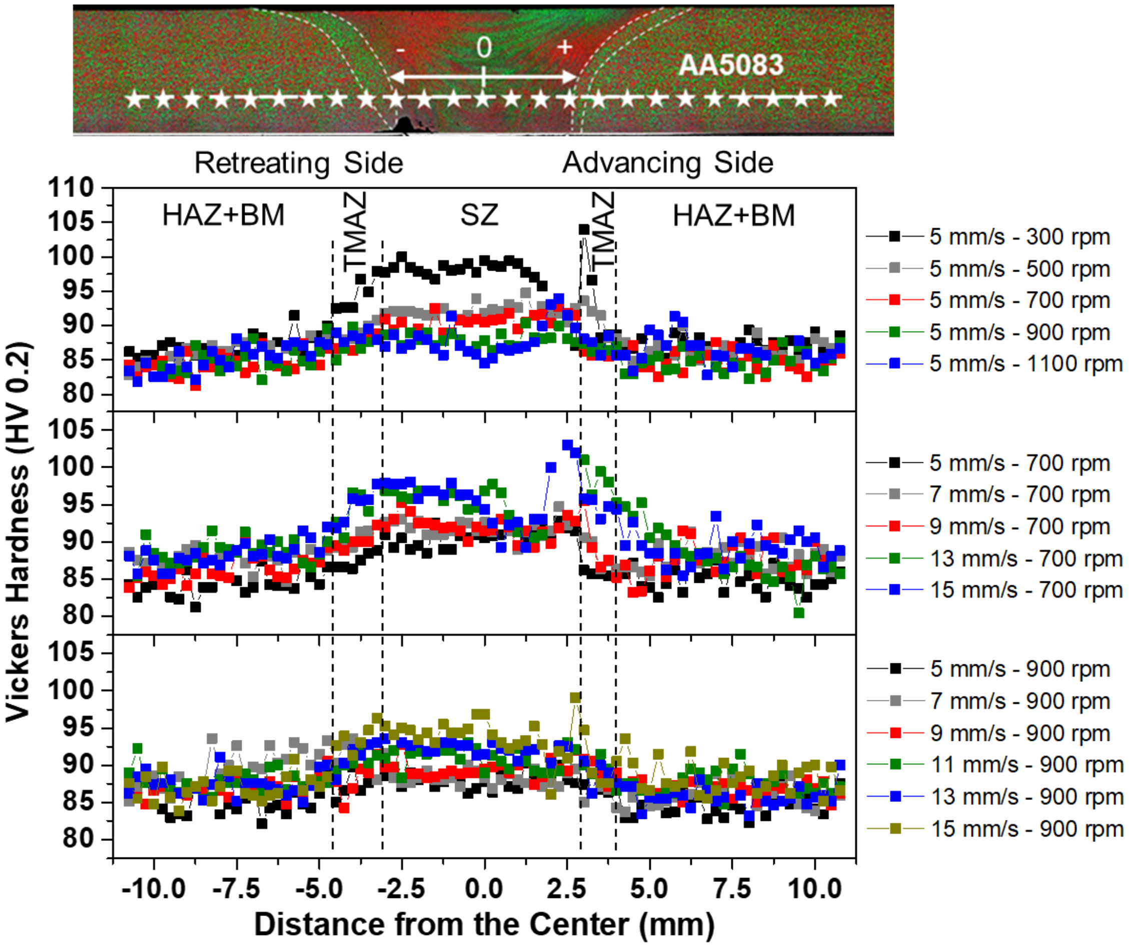

Figure 5.23 – Horizontal microhardness profile along the aluminum alloy part of the welds at different welding speeds and rotational speeds.

A relationship between the microhardness values and the welding speed and rotational speed could be established, similar to the dependence of the grain size on the Al-SZ with the welding parameters. Maintaining a constant welding speed, as seen in Figure 5.23, the average microhardness in the Al-SZ increased with the decrease of the rotational speed, achieving a minimum average microhardness of about 88 $HV_{0.2}$ in the Al-SZ of the weld 5 (5 mm/s and 1100 rpm), and a maximum average microhardness of about 100 $HV_{0.2}$ in the Al-SZ of the weld 1 (5 mm/s and 300 rpm). On the other hand, maintaining a constant rotational speed, the average microhardness in the Al-SZ increased with the increase of the welding speed. At a constant rotational speed of 700 rpm, a minimum average microhardness of about 90 $HV_{0.2}$ was achieved in the Al-SZ of the weld 3 (5 mm/s and 700 rpm), and a maximum average microhardness of about 96 $HV_{0.2}$ was achieved in the Al-SZ of the weld 9 (15 mm/s and 700 rpm). At a constant rotational speed of 900 rpm, a minimum average microhardness of about 88 $HV_{0.2}$ was achieved in the Al-SZ of the weld 4 (5 mm/s and 900 rpm), and a maximum average microhardness of about 94 $HV_{0.2}$ was achieved in the Al-SZ of the weld 14 (15 mm/s and 900 rpm).

The relation between the average microhardness in the Al-SZ and the welding parameters occurred because of the grain boundary strengthening in the AA5083, determined by the grain size, and governed by the Hall-Petch equation, as reported by Yazdipour et al. [95] and Sato et al. [102]. In this case, increasing the welding speed or decreasing the rotational speed, the energy input per unit length decreases, being insufficient for the grain growth after the dynamic recrystallization. The increase of the welding speed also acts by reducing the welding time available to grain growth. Therefore, the amount of grain boundaries is higher with the grain size reduction, increasing the amount of obstacles for dislocation movement and the resistance to the local plastic deformation, resulting in higher microhardness values in the Al-SZ when increasing the welding speed or decreasing the rotational speed.

Looking at the other part of the welds, the horizontal microhardness profile along the cross-section of the steel part of the welds is shown in Figure 5.24. Similar to previously discussed to the aluminum part of the welds, the measurements were produced at 1 mm of distance from the weld interface, and as can be seen, the weld zones can be identified by their microhardness values. The GL D36 BM presents hardness values of around 165 $HV_{0.2}$ that is determined by the refinement of the ferrite and perlite grains. Since the energy input during the welding was not enough to cause phase transformation, the increase in microhardness in the St-HAZ and St-TMAZ occurred due to the grain refinement and deformation as a consequence of the strain hardening and dynamic recrystallization.

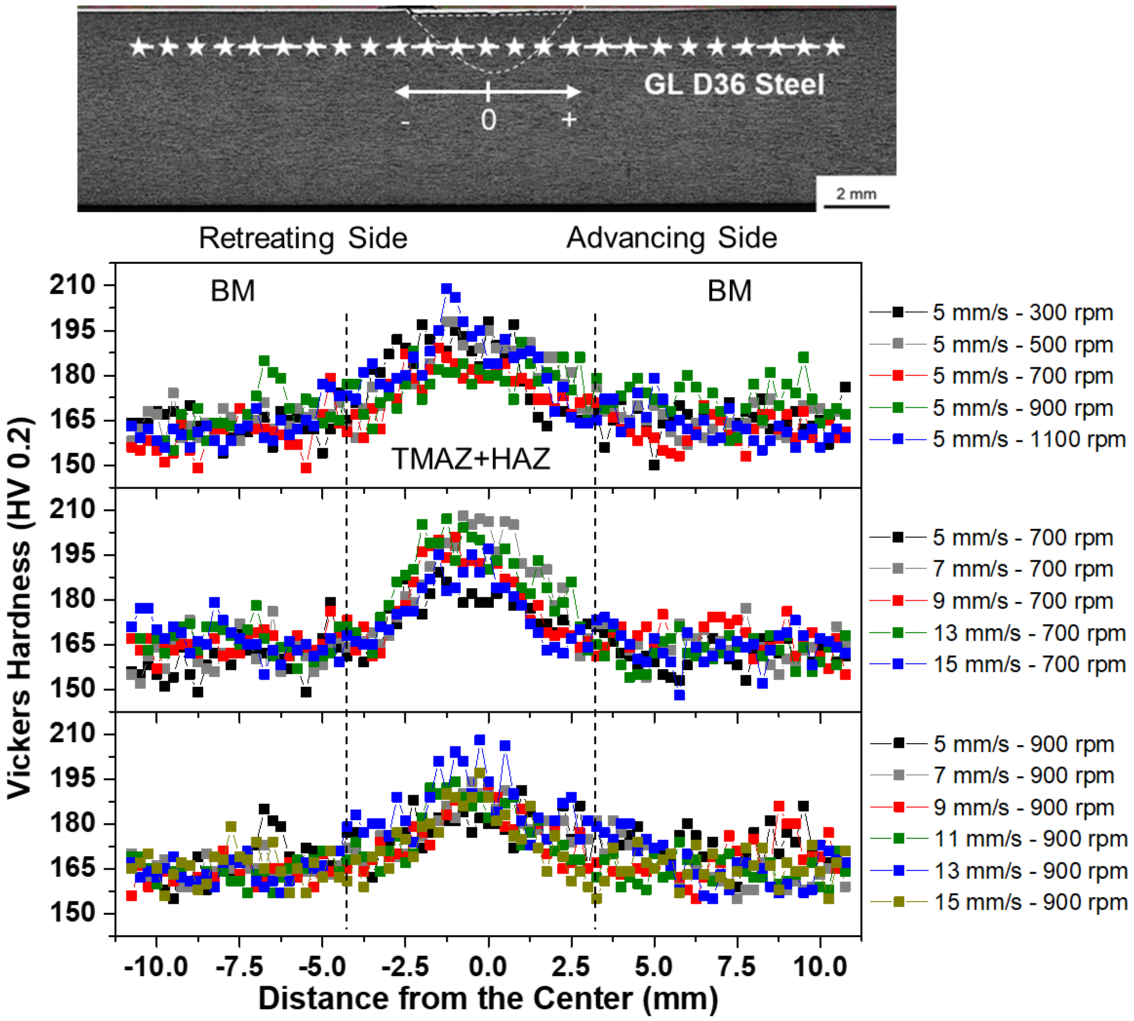

Figure 5.24 – Horizontal microhardness profile along the steel part of the welds at different welding speeds and rotational speeds.

Unlike the weld zones in the aluminum alloy part of the joints, no obvious correlations between the microhardness measurements and the welding parameters could be established, which might be related to the higher melting point of the steel, and non-insertion of the probe into the steel plate that just scratched the plate surface. Nonetheless, some tendencies can be observed in the St-TMAZ. Maintaining a constant welding speed, as seen in Figure 5.24, a minimum microhardness of 177 $HV_{0.2}$ was achieved in the weld 4 (5 mm/s and 900 rpm), and a maximum microhardness of 209 $HV_{0.2}$ was achieved in the weld 5 (5 mm/s and 1100 rpm). Meanwhile, a minimum microhardness of 179 $HV_{0.2}$ was achieved in the weld 3 (5 mm/s and 700 rpm), and a maximum microhardness of 208 $HV_{0.2}$ was achieved in the weld 6 (7 mm/s and 700 rpm), when kept a constant rotational speed of 700 rpm. Furthermore, maintaining a constant rotational speed of 900 rpm, a minimum microhardness of 177 $HV_{0.2}$ was achieved in the weld 4 (5 mm/s and 900 rpm), and a maximum microhardness of 208 $HV_{0.2}$ was achieved in the weld 13 (13 mm/s and 900 rpm).

As discussed previously, during the presentation of the microstructure of the steel, the St-TMAZ depth showed a tendency to increase with the increase of the rotational speed and welding speed due to the improvement of the frictional heating and strain at the steel near the interface, when the width of the welded interface was reduced. As can be seen in Figure 5.24, keeping a constant welding speed of 5 mm/s and varying the rotational speed, the maximum microhardness value was obtained in the St-TMAZ of the weld 5, produced using the highest rotational speed (1100 rpm), which is in line with the tendency to increase the St-TMAZ depth increasing the rotational speed. In the same way, it can be seen in Figure 5.24 that the lowest values of microhardness were obtained in the St-TMAZ of the welds 3 and 4, respectively, produced using the lowest welding speed (5 mm/s), which significantly reduced the depth of the St-TMAZ. It is also valid to remember that the welds with the highest welding speed did not follow the tendency to increase the St-TMAZ depth, due to the insufficient material flow that generates tunnel defects, and because of this, these welds did not present the highest microhardness values of the St-TMAZ.

However, in view that the probe was not inserted in the steel plate and the plastic deformation of the steel was higher near the interface, the microhardness in the St-TMAZ increases approaching the interface, as can be seen in Figure 5.25, where is presented the vertical microhardness profile perpendicular to the weld interface. The microhardness of the Al-SZ, St-TMAZ, St-HAZ, and St-BM, already discussed, can be observed.

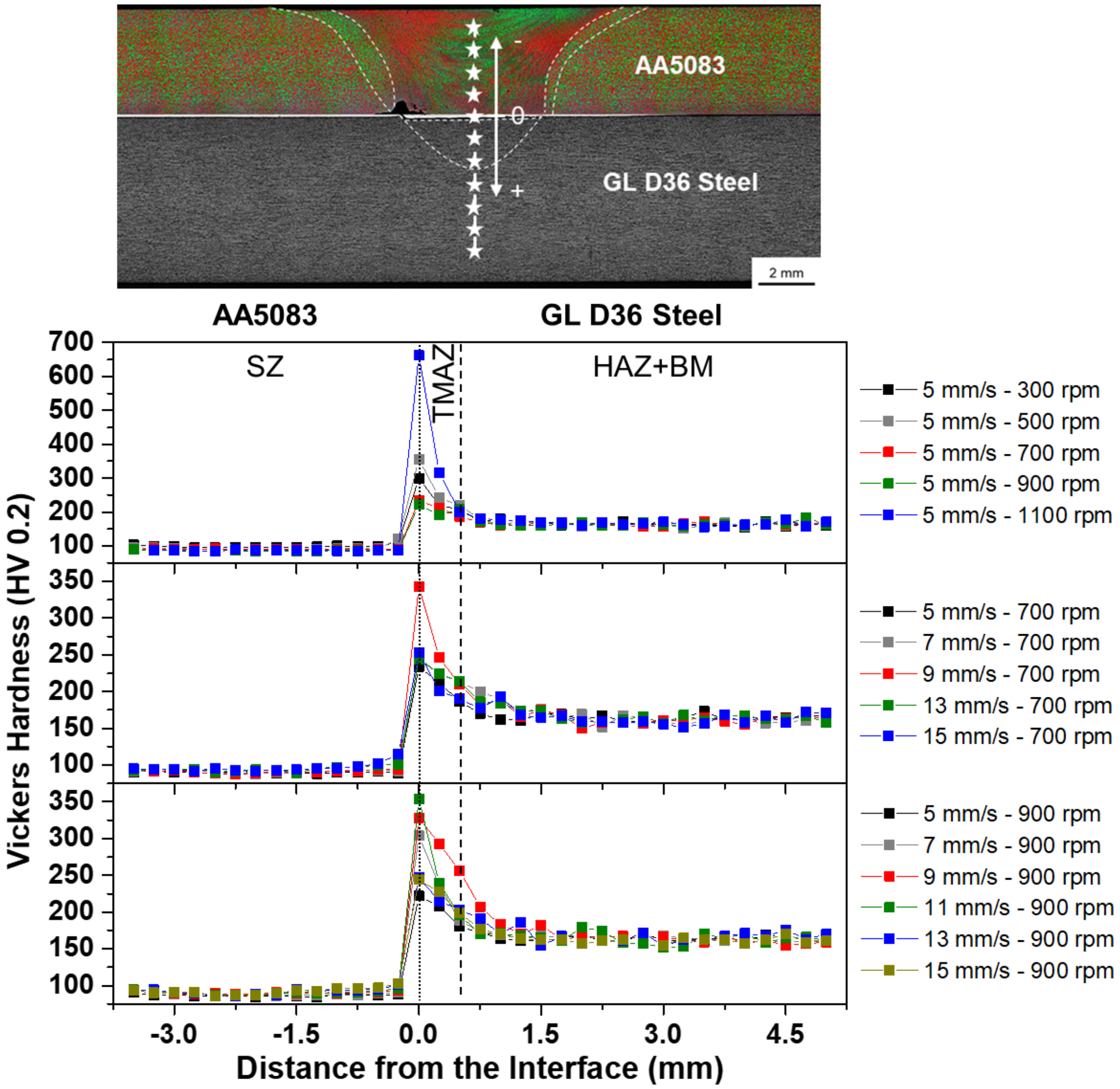

Figure 5.25 – Vertical microhardness profile perpendicular to the interface of the welds at different welding speeds and rotational speeds.

The microhardness profile along the thickness of the Al-SZ is almost constant, with slight variations related to the grain size, which is smaller in some parts of the Al-SZ, such as in the top of the weld, due to the friction action of the shoulder during the welding. Anyway, the increase of the microhardness profile along the thickness of the Al-SZ was kept increasing the welding speed and decreasing the rotational speed.

The increase of the microhardness of the St-TMAZ near the weld interface was also observed, due to the grain size deformation and refinement as a consequence of the higher energy input and plastic deformation. Despite this, the maximum microhardness occurred at the interface, due to the presence of IMCs, as suggested by SEM analyses. Maintaining a constant rotational speed of 700 rpm, a minimum microhardness of 234 $HV_{0.2}$ was achieved in the interface of the weld 3 (5 mm/s and 700 rpm), and a maximum microhardness of 343 $HV_{0.2}$ was achieved in the interface of the weld 7 (9 mm/s and 700 rpm). Similarly, a minimum microhardness of 222 $HV_{0.2}$ was achieved in the interface of the weld 4 (5 mm/s and 900 rpm), and a maximum microhardness of 354 $HV_{0.2}$ was achieved in the interface of the weld 12 (11 mm/s and 900 rpm), maintaining a constant rotational speed of 900 rpm. However, the maximum microhardness in the interface of 662 $HV_{0.2}$ was obtained in the weld 5 (5 mm/s and 1100 rpm), which presented the highest average energy input per unit length among the welds being studied, consequently increasing the thickness of the IMC layer.

In spite the increase of the microhardness at the interface due to the presence of IMCs, these measurements obtained do not represent the microhardness of the IMCs, since the layers of intermetallic phases were much thinner than the size of the hardness indentation, as can be seen in Figure 5.26, where is shown the microhardness indentation on the mixed layers in the interface of the weld 5. For the correct measure of the hardness of the IMCs, nanohardness measurements should be used, as reported by Das et al. [86] in an investigation about the influence of the processing parameters on the mechanical properties of dissimilar aluminum to steel FSW lap joints.

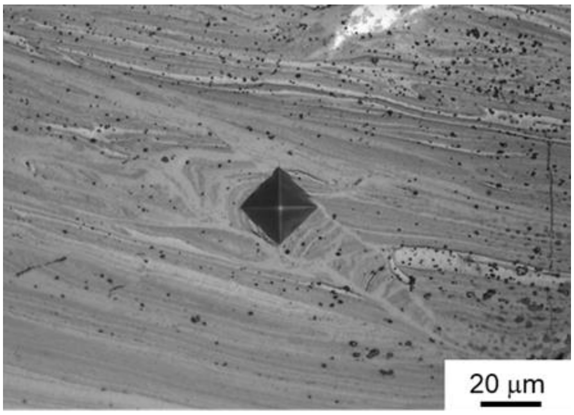

Figure 5.26 – Microhardness indentation in the mixed layers in the interface of the weld 5 produced using a welding speed of 5 mm/s and rotational speed of 1100 rpm.

In sum, the Vickers microhardness of the welds was affected by the different microstructure of the weld zones and interface. In the aluminum alloy, the maximum microhardness of around 100 $HV_{0.2}$ was achieved in the SZ of the weld with a welding speed of 5 mm/s and a rotational speed of 300 rpm, due to the presence of fine and equiaxed dynamically recrystallized grains. The decrease of the welding speed and increase of the rotational speed caused the decrease of the microhardness in the Al-SZ. In the steel, the microhardness increased in the TMAZ due to the grain deformation and refinement during the welding. However, the maximum microhardness was obtained in the interface, achieving a maximum microhardness of 662 $HV_{0.2}$ in the interface of the weld with a welding speed of 5 mm/s and a rotational speed of 1100 rpm, due to the presence of brittle IMC layers.

5.5.2 Lap Shear Tensile Tests

Analyzes of the influence of the welding speed and rotational speed on the joints strength were made through lap shear tensile tests. These tests provide a manner to correlate the macrostructural features, microstructure, and interface properties of the lap welds with their mechanical properties.

The results of the lap shear tensile tests are shown in Figure 5.27 for the samples with a better response between the three tests for each welding parameters. They are presented as lap shear load (N) versus displacement (mm) due to the complex mixing of aluminum and steel at the weld region, which impossibilities the precise determination of the welded area along the entire weld length. Besides, small variations in the maximum lap shear load and displacement to fracture occurred among samples with the same welding parameters, but the profile of the curves was maintained regardless of the sample.

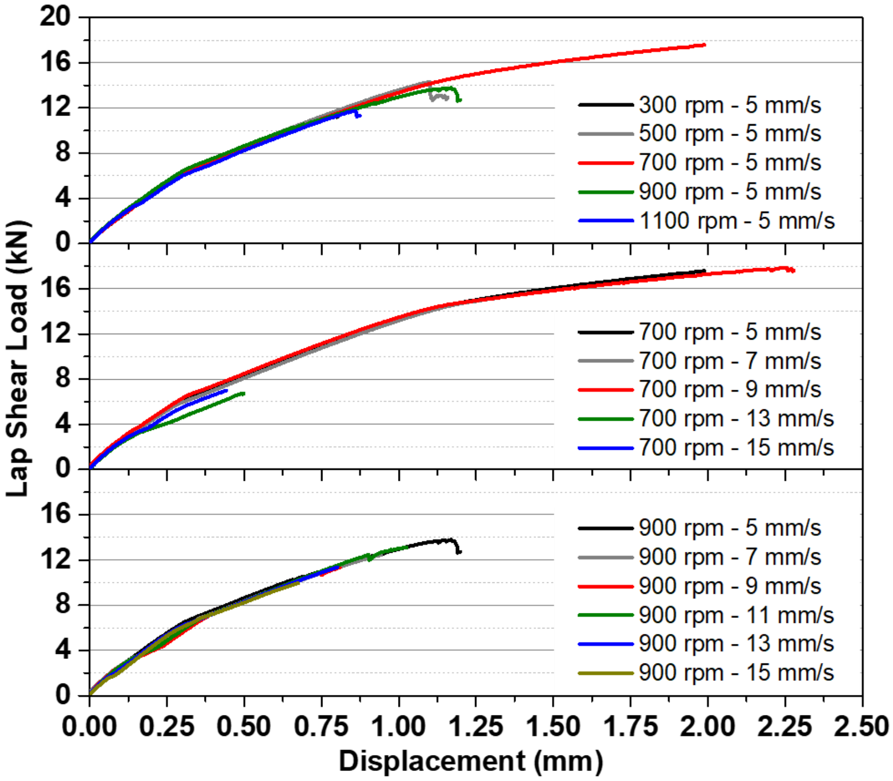

Figure 5.27 – Results of the lap shear tensile tests of welds produced by FSW using different welding speeds and rotational speeds.

The welds also showed low displacement to fracture, with a maximum displacement to fracture of 2.28 mm in the weld 7, produced using a welding speed of 9 mm/s and rotational speed of 700 rpm, followed by a displacement to fracture of 1.99 mm in the weld 3, produced using a welding speed of 7 mm/s and rotational speed of 700 rpm, as can be seen in Figure 5.27. Even using different process parameters, another research reported similar maximum displacement to fracture in dissimilar aluminum to steel FSW lap joints [10].

However, the displacement values in Figure 5.27 refers to the better result for each welding parameter. Considering the results of the three tests for each welding parameter, the average displacement to fracture was calculated and is presented in Figure 5.28. The highest average displacement to fracture of 1.79 mm was obtained in the welds 3 and 7, produced using a rotational speed of 700 rpm, and welding speed of 5 mm/s and 9 mm/s, respectively. Despite the slightly thicker IMC layer in the interface of the weld 7 (400 ± 70 nm) compared to the weld 3 (250 ± 40 nm), the weld 7 presented the highest steel hook height of 714

± 33 μm at the interface, against 605 ± 35 μm at the interface of the weld 3, which would improve the mechanical locking in the interface, and the average displacement to fracture. On the contrary of the steel hook, can be seen in Figure 5.28 that the presence of tunnel defects in the weld zone significantly reduced the average displacement to fracture, in view that the welds produced using higher welding speeds as 13 mm/s and 15 mm/s, or lower rotational speed as 300 rpm presented this macrostructural feature. In addition, most of the welds produced using a rotational speed of 900 rpm showed lower average displacement to fracture than the welds produced using a rotational speed of 700 rpm, which may be related to the formation of thicker IMC layers in the weld interface when the energy input is increased with the rotational speed increase.

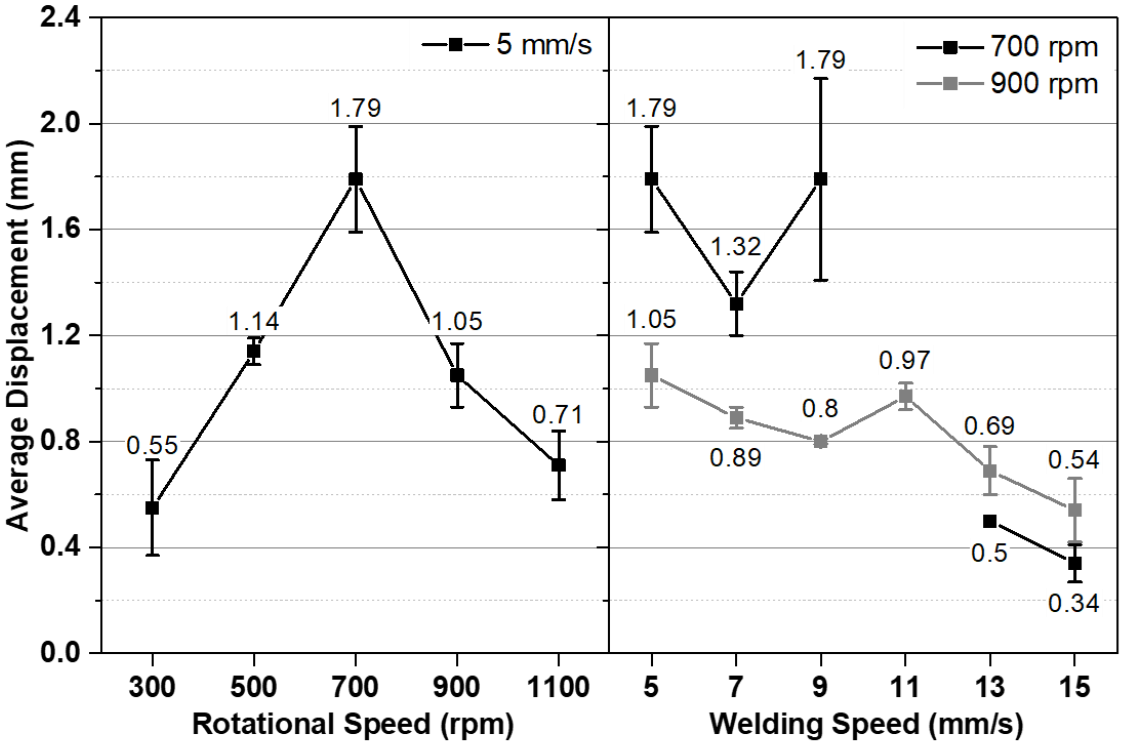

(a) (b)

Figure 5.28 – Average displacement to fracture of the welds at a constant (a) welding speed of 5 mm/s, and (b) two different rotational speeds.

The lower displacement to fracture of the joints occurred due to the presence of brittle IMC layers at the welds interface. Despite minimizing the abrupt metallurgical differences at the interface between aluminum and steel, the presence of these intermetallic phases makes the interface region the weakest part of the weld, where the fracture occurred, as shown in Figure 5.29a and Figure 5.29b. All the welds fractured in the weld interface, and the image of the samples tests for each welding parameter studied can be found in Appendix E. During the lap shear tensile test, the failure initiates at the corner of the interfacial layer, where occurred a peak of stress, and the crack grows in direction to the joint center, as studied by finite element analysis of adhesively bonded joints [103]. Consequently, the fracture initiated and grown throughout the brittle IMC layer in the weld interface, as detached by the red-marked regions and arrows in Figure 5.29c.

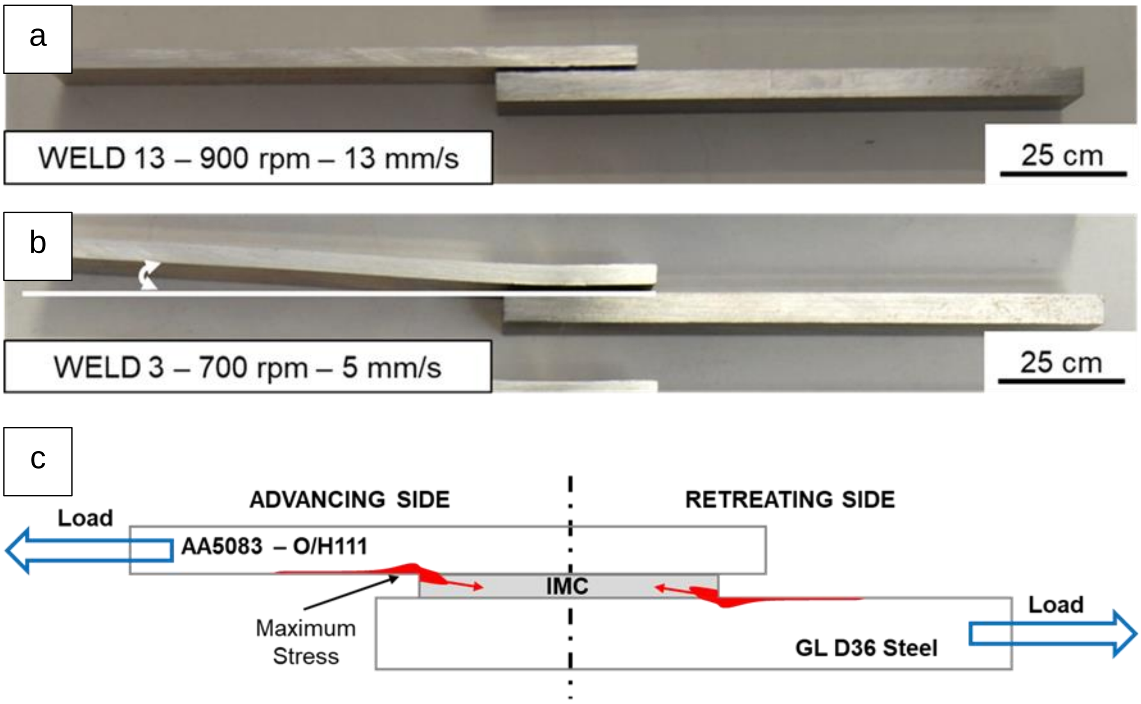
a
WELD 13 – 900 rpm – 13 mm/s
25 cm
b
WELD 3 – 700 rpm – 5 mm/s
25 cm
c
ADVANCING SIDE
RETREATING SIDE
Load
AA5083 – O/H111
IMC
Maximum Stress
GL D36 Steel
Load

Figure 5.29 – Samples after lap shear tensile tests produced by FSW using welding speed and rotational speed of (a) 13 mm/s and 900 rpm and (b) 5 mm/s and 700 rpm; and (c) schematic illustration of the maximum stress during the lap shear tensile tests.

Additionally, maximum stress during lap shear tensile test is reported to occur in the base materials near the corners of the interfacial layer, as indicated in Figure 5.29c. This results in the bending of the base materials and can cause their failure, as already reported by Pourali et al. [89], Wei et al. [13], and Coelho et al. [10], with the fracture occurring in the aluminum alloy in dissimilar aluminum to steel FSW lap joints. The location of the maximum stress during lap shear tensile test is also related to the configuration of the joint. Despite this has been investigated just for similar materials, a study reported that welds produced with the top plate placed on AS presents higher lap shear strength than welds produced with the top plate placed on RS, due to the occurrence of hooking effect on the RS, reducing the thickness of the top plate, and consequently, the joint strength [104]. Applying this to dissimilar welds, in the present study, the aluminum plate was placed in the AS, the steel hook was present in the RS, and the maximum stress on RS occurred mainly in the steel plate. In this way, the steel hook did not actuate reducing the aluminum thickness, and then, the maximum stress in the base materials in this study was just enough to cause the bending of the aluminum alloy, more significant with higher average displacement to fracture, as can be seen in Figure 5.29b compared to Figure 5.29a. On the contrary, the joints reported in the literature [10, 13, 89] were welded with the aluminum plate placed on the RS, and then, the maximum stress occurred mainly in the aluminum plate on the RS, where the steel hook was present.

The differences in the mechanical properties of the joints are also evidenced by significant variations in the average maximum lap shear load with the welding parameters, as shown in Figure 5.30. The average lap shear load presented a similar relation to the welding parameters as the average displacement to fracture. The maximum average lap shear load of 16.98 kN was obtained in the weld 3, produced using a welding speed of 5 mm/s and a rotational speed of 700 rpm.

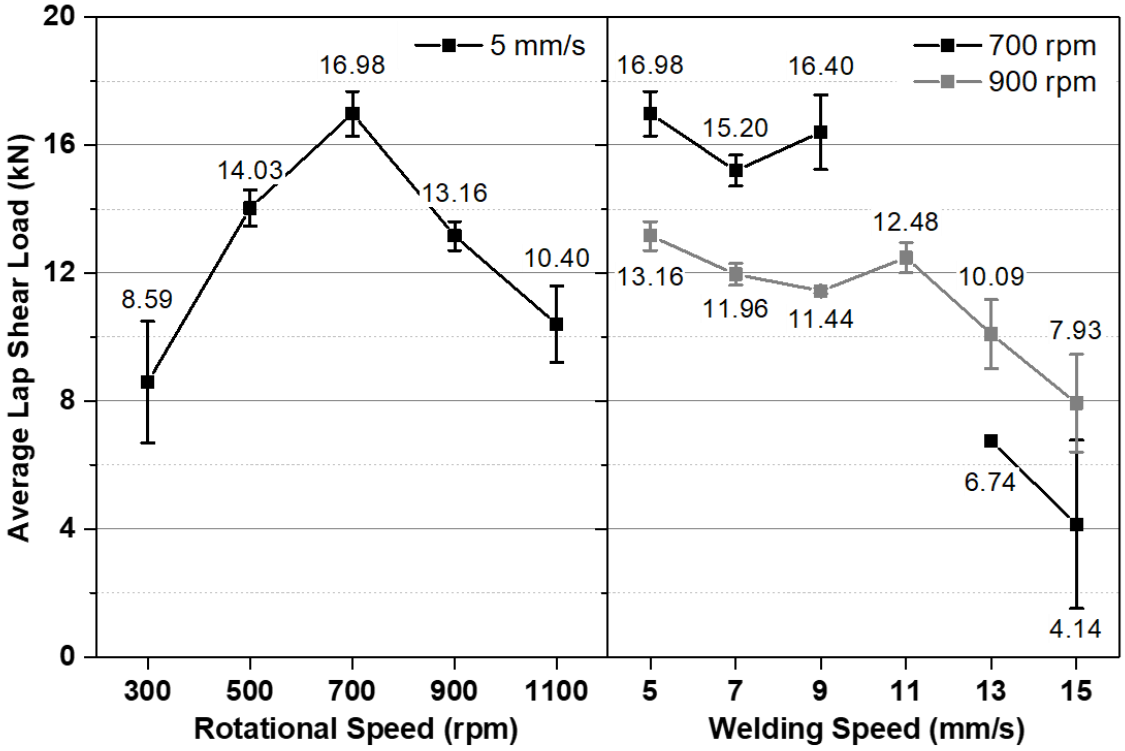

(a) (b)

Figure 5.30 – Average maximum lap shear load of the welds at a constant (a) welding speed of 5 mm/s, and (b) two different rotational speeds.

This result is similar or superior to those lap shear loads already reported in the literature for dissimilar aluminum to steel lap joints made by FSW [10, 17, 86-89, 92, 96]. For example, Pourali et al. [89] reported a maximum lap shear load of 1925 N in a 2 mm thick AA1100 and St-37 low carbon steel FSW lap joint produced using a welding speed of 50 mm/min and rotational speed of 400 rpm, an overlap of 40 mm, and a sample for lap shear tensile test 10 mm wide. In contrast, Movahedi et al. [87] obtained a maximum lap shear load of 7598 N in a 3 mm thick AA5083 to 1 mm thick St-12 steel FSW lap joint using a welding speed of 15 cm/min and rotational speed of 1125 rpm, an overlap of 35 mm, and a sample for lap shear tensile test 25 mm wide. In another study, AA5083 and SS400 mild steel (both 3 mm thick) FSW lap joint reached the maximum lap shear load of 5591 N using a welding speed of 0.73 mm/s, a rotational speed of 3.75 s^{-1}, probe depth of 0.1 mm, an overlap of 30 mm, and a sample for lap shear tensile test 10 mm wide [96].

In the case of dissimilar aluminum to steel joints produced by the explosion welding process, lap shear loads from 31 kN for 5 mm x 70 mm AA5083 and SS41 joints [31] until 10800 kN for 100 mm x 150 mm explosively welded aluminum and High-Strength Low-Alloy (HSLA) steel joints [32] can be achieved. However, the welded area in explosion welding is significantly larger than in FSW, which makes impossible the comparison with the lap shear loads obtained in this study.

The effects of the welding parameters on the average lap shear load are similar to the effects on the average displacement to fracture. The average lap shear load decreased with increasing the welding speed and increased with increasing the rotational speed until 700 rpm, and then, decreased with continuous rotational speed increases. The highest welding speeds as 13 mm/s and 15 mm/s, and lowest rotational speed as 300 rpm, resulted in tunnel defects in the welds macrostructure, which resulted in the lowest values of lap shear load. The presence of a mixed layer at higher rotational speed as 1100 rpm with the presence of cracks and thicker IMCs layers also resulted in lower lap shear load.

Higher lap shear load was obtained to low welding speeds as from 5 mm/s to 11 mm/s, and intermediate rotational speeds as 500 rpm, 700 rpm, and 900 rpm, which did not present tunnel defects in their welds macrostructure. These welds presented different sizes of IMC layer thickness and steel hook height. The steel hook height had significant influence as mechanical locking since the highest average lap shear loads were obtained in the welds 3 (5 mm/s and 700 rpm) and 7 (9 mm/s and 700 rpm) that also presented the highest height of the steel hook. The decrease of the steel hook height resulted in the decrease of the average lap shear load, as demonstrated by the weld 2 (5 mm/s and 500 rpm), which even with the thinner IMC layer when the rotational speed was decreased, presented a steel hook height of 96 ± 9 μm, much smaller than that observed in the welds 3 and 7. Besides that, the metallurgical bonding resultant of the presence of IMC layers in the welds interface also influenced the average lap shear load, which decreased with increasing welding speed and rotational speed, and consequently, with thicker IMC layers. As can be observed in weld 7, compared to weld 3, despite the higher steel hook height, the weld 7 presented a thicker IMC layer, which slightly reduced its lap shear load, compared to weld 3. Weld 3 also presented micro interlocks in the interface, contributing to the highest lap shear load.

Therefore, it can be concluded that higher mechanical properties are obtained in dissimilar AA5083-O/H111 and GL D36 steel FSW lap joints by the combination of metallurgical bonding through thinner IMC layers formation, and mechanical locking, with higher steel hooks height and micro interlocks in the welds interface. This result is similar to reported by Movahedi et al. [87] investigating dissimilar AA5083 to St-12 steel lap joints made by FSW. The metallurgical bonding through IMC layer formation and mechanical bonding consisting of an interlaced structure of aluminum and steel in the interface or micro interlocks were also reported in other investigations [13, 90] as reinforcements in dissimilar aluminum to steel FSW lap joints.

Similarly, Coelho et al. [10] concluded that the IMC layers added to the mechanical interlocking, but they stated that the amount of steel particles dispersed in the Al-SZ determine the mechanical properties of the joints, because these fragments act as discontinuities, concentrating stress and possibly initiating cracks and degrading mechanical properties. In the present study, a direct relationship between the steel particles in the Al-SZ and the joint strength could not be established, owing to the maximum average lap shear load in the weld 3 (5 mm/s and 700 rpm), with the lowest welding speed and thus higher amount of steel particles dispersed in the aluminum matrix, countering that stated by Coelho et al. [10]. Moreover, no relation between the microstructure of the weld zones and the joint strength was established in this work, since all the fractures during the lap shear tensile test occurred in the interface of the joints.

6 CONCLUSIONS

Dissimilar AA5083-O/H111 to GL D36 steel joints were produced by Friction Stir Welding (FSW), and from the influence of the welding speed and rotational speed on the macrostructural, microstructural, and interface properties, and their influence on the mechanical properties, the following conclusions can be drawn:

- Sound joints, without voids and defects, were produced using low welding speed (5 mm/s and 7 mm/s) and intermediate rotational speed (500 rpm, 700 rpm, and 900 rpm), which presented steel hook with higher height and more steel particles dispersed in the aluminum weld zone. The increase of the welding speed (between 9 mm/s and 15 mm/s) or decrease of the rotational speed (300 rpm) resulted in scattered voids or tunnel defects in the macrostructure of the welds. Furthermore, the increase of the rotational speed (1100 rpm) caused the formation of flashes in the weld surface, and a lamellar structure in the weld interface, with cracks inside.
- The decrease of the welding speed and increase of the rotational speed caused the coarsening of the grain size in the aluminum Stir Zone (SZ), which achieved a maximum grain size of 15.64 μm (5 mm/s and 1100 rpm) and minimum grain size of 4.04 μm (5 mm/s and 300 rpm). In the steel, a tendency to a deeper and less wide Thermo-Mechanically Affected Zone (TMAZ) was observed with the increase of the welding speed and rotational speed.
- The FSW process resulted in continuous Intermetallic Compound (IMC) layers throughout the entire interface of the welds, composed of FeAl and Fe_3Al Fe-rich phases. The average thickness of these layers increased with the increasing of the welding speed and rotational speed, varying from an average thickness of about 250 nm (5 mm/s and 700 rpm) to an average thickness of about 800 nm (9 mm/s and 900 rpm). In addition, the different plastic deformability between the aluminum and steel resulted in micro interlocks in the weld interface.
- In the aluminum alloy, the maximum microhardness of around 100 $HV_{0.2}$ was achieved in the SZ of the weld with a welding speed of 5 mm/s and a rotational speed of 300 rpm, which decreased with decreasing the welding speed and increasing the rotational speed. The maximum microhardness was obtained

in the interface, achieving a maximum microhardness of 662 $HV_{0.2}$ (5 mm/s and 1100 rpm), due to the presence of brittle IMC layers.

- The maximum average lap shear load of 16.98 kN was obtained in the weld with a welding speed of 5 mm/s and a rotational speed of 700 rpm, which presented a high steel hook, thinner IMC layers, and micro interlocks in the weld interface. The increase of the welding speed and increase or decrease of the rotational speed resulted in the degradation of the mechanical properties, due to the reduction of the steel hook height, the increase of the thickness of the IMC layers, and the presence of voids or tunnel defects on the weld zone. Therefore, better mechanical properties of the welds are resultant of the combination of metallurgical bonding through thinner IMC layers formation, and mechanical locking, with higher steel hooks height and micro interlocks in the weld interface.

7 FUTURE WORKS

The Friction Stir Welding (FSW) process was demonstrated to be a suitable method for the production of dissimilar AA5083-O/H111 to GL D36 steel lap joints. However, for a better understanding of the influence of the process parameters on joint properties, and to evaluate the behavior of the welds in marine environments, further studies could be done, as summarized in the following recommendations for future works:

- Investigations of the corrosion behavior of the welds in marine environments.
- Transmission Electron Microscopy (TEM) analysis of the IMC layers at the interface region of the welds, and Electron Backscattered Diffraction (EBSD) investigations of the grain size distribution and crystallography orientation of the different weld zones.
- Investigations of the influence of the plates' position on joints properties, analyzing the influence of the welding speed and rotational speed on the properties of joints with the aluminum plate on the Retreating Side (RS) and the steel plate on the Advancing Side (AS), and comparing with the results obtained in this work, where the aluminum plate was placed on the AS and the steel plate on the RS.
- Analysis of the influence of other parameters, such as the probe depth and the axial force, on the joints properties, when varying the welding speed and rotational speed, in view of the complex plastic deformation and intermetallic phase formation in the weld region.
- Producing dissimilar AA5083-O/H111 and GL D36 steel FSW lap joints using adhesive and coating under the same process condition analyzed in this work, to investigate their influence on the properties of the welds, since this protection is normally used for marine applications.

8 REFERENCES

[1] Aluminium in commercial vehicles. **European Aluminium Association**. Available on: <https://www.european-aluminium.eu/media/1295/aluminium-in-commercial-vehicle_en.pdf>. Accessed on 25 March 2020.

[2] WITIK, R.A.; PAYET, J.; MICHAUD, V.; LUDWIG, C.; MANSON, J.A.E. Assessing the life cycle costs and environmental performance of lightweight materials in automobile applications. **Composites: Part A**, vol. 42, pp. 1694-1709, 2011.

[3] Aluminum content in cars for European Aluminium Association (2016) **Ducker Worldwide.** Available on: <https://european-aluminium.eu/media/1721/european-aluminium-ducker-study-summary-report_sept.pdf>. Accessed on 25 March 2020.

[4] Aluminum content in European passenger cars for European Aluminium Association (2019) **DuckerFrontier**. Available on: <https://www.european-aluminium.eu/media/2714/aluminum-content-in-european-cars_european-aluminium_public-summary_101019-1.pdf>. Accessed on 25 March 2020.

[5] MARTINSEN, K.; HU, S.J.; CARSLON, B.E. Joining of dissimilar materials. **CIRP Annals – Manufacturing Technology**, vol. 64, pp. 679-699, 2015.

[6] ATABAKI, M.M.; NIKODINOVSKI, M.; CHENIER, P.; MA, J.; HAROONI, M.; KOVACEVIC, R. Welding of Aluminum Alloys to Steels: An Overview. **Journal for Manufacturing Science and Production**, vol. 14, pp. 59-78, 2014.

[7] TABAN, E.; GOULD, J.E.; LIPPOLD, J.C. Dissimilar Friction Welding of 6061-T6 Aluminum and AISI 1018 Steel: Properties and Microstructural Characterization. **Materials and Design**, vol. 31, pp. 2305-2311, 2010.

[8] BUJIS, K. TRIPLATE® The ultimate solution for welding aluminum to steel. **HSB International**, Dordrecht, 2004. 4p.

[9] YAZDIPOUR, A.; HEIDARZADEH, A. Dissimilar butt friction stir welding of Al5083-H321 and 316L stainless steel alloys. **The International Journal of Advanced Manufacturing Technology**, vol. 87, pp. 3105-3112, 2016.

[10] COELHO, R.S.; KOSTKA, A.; SHEIKHI, S.; DOS SANTOS, J.F.; PYZALLA, A.R. Microstructure and Mechanical Properties of an AA6181-T4 Aluminium Alloy to HC340LA High Strength Steel Friction Stir Overlap Weld. **Advanced Engineering Materials**, vol. 10, pp. 961-972, 2008.

[11] ELREFAEY, A.; TAKAHASHI, M.; IKEUCHI, K. Friction-Stir-Welded Lap Joint of Aluminum to Zinc-Coated Steel. **Quarterly Journal of the Japan Welding Society**, vol. 23, pp. 186-193, 2006.

[12] UZUN, H.; DALLE DONNE, C.; ARGAGNOTTO, A.; GHIDINI, T.; GAMBARO, C. Friction stir welding of dissimilar Al 6013-T4 to X5CrNi18-10 stainless steel. **Materials and Design**, vol. 26, pp. 41-46, 2005.

[13] WEI, Y.; LI, J.; XIONG, J.; ZHANG, F. Effect of tool pin insertion depth on friction stir lap welding of aluminum to stainless steel. **Journal of Materials Engineering and Performance**, vol. 22, pp. 3005-3013, 2013.

[14] CHEN, Z.W.; YAZDANIAN, S.; LITTLEFFAIR, G. Effects of tool positioning on joint interface microstructure and fracture strength of friction stir lap Al-to-steel welds. **Journal of Materials Science**, vol. 48, pp. 2624-2634, 2013.

[15] LAN, S.; LIU, X.; NI, J. Microstructural evolution during friction stir welding of dissimilar aluminum alloy to advanced high-strength steel. **The International**

Journal of Advanced Manufacturing Technology, vol. 82, pp. 2183-2193, 2015.

[16] CHEN, Y.C.; KOMAZAKI, T.; KIM, Y.G.; TSUMURA, T.; NAKATA, K. Interface microstructure study of friction stir lap joint of AC4C cast aluminum alloy and zinc-coated steel. **Materials Chemistry and Physics**, vol. 111, pp. 375-380, 2008.

[17] WAN, L.; HUANG, Y. Microstructure and Mechanical Properties of Al/Steel Friction Stir Lap Weld. **Metals**, vol. 7, 14 p., 2017.

[18] TORREZ, J. B. **Light-Weight Materials Selection for High-Speed Naval Craft**. 2007. 111 p. Master Thesis (Degrees of Naval Engineer and Master of Science in Civil and Environmental Engineering) – Departments of Mechanical and Engineering and Civil and Environmental Engineering, Massachusetts Institute of Technology, Massachusetts, USA, 2007.

[19] MILLER, W. S.; ZHUANG, L.; BOTTEMA, J.; WITTEBROOD, A. J.; DE SMET, P.; HASZLER, A.; VIEREGGE, A. Recent Development in Aluminium Alloys for the Automotive Industry. **Materials Science and Engineering A**, vol. 280, pp. 37-49, 2000.

[20] SAKIYAMA, T.; NAITO, Y.; MIYAZAKI, Y.; NOSE, T.; MURAYAMA, G.; SAITA, K.; OIKAWA, H. Dissimilar Metal Joining Technologies for Steel Sheet and Aluminum Alloy Sheet in Auto Body. **Nippon Steel Technical Report**, n. 103, pp. 91-98, May 2013.

[21] YUCE, C.; KARPAT, F.; YAVUZ, N.; DOGAN, O. A review on advanced joining techniques of multi material part manufacturing for automotive industry.

Proceedings of Eighteenth TheIIER International Conference, Rome, Italy, pp. 51-56, 28-29 March 2015.

[22] CHEN, T. Process parameters study on FSW joint of dissimilar metals for aluminum-steel. **Journal of Materials Science**, vol. 44, pp. 2573-2580, 2009.

[23] HULAND, S.; MÖLLER, M.; FRANKE, M.; VAKALOPOULOS, T. The electrification of the Passat: The GTE. **Viavision**, July 2015. Available on: <http://www.viavision.org/ftp/1794.pdf>. Accessed on 01 June 2019.

[24] KUSUDA, Y. Honda develops robotized FSW technology to weld steel and aluminum and applied it to a mass-production vehicle. **Industrial Robot: An Industrial Journal**, vol. 40, n. 3, pp. 208-212, 2013.

[25] OHHAMA, S.; HATA, T.; YAHABA, T.; KOBAYASHI, T.; MIYARA, T.; SAYAMA, M. Application of an FSW Continuous Welding Technology for Steel and Aluminum to an Automotive Subframe. **Proceedings of the SAE 2013 World Congress & Exhibition**, Detroit, USA, 16-18 April 2013. 7 p.

[26] SKILLINGBERG, M. Aluminum at Sea: Speed, endurance and affordability. **Marine Log**, pp. 27-32, May 2007. Available on: <https://www.aluminum.org/sites/default/files/Aluminum_at_Sea.pdf>. Accessed on 02 June 2019.

[27] TRICLAD®: Welding Aluminium to Steel. **Technical Information**. Available on: <https://studylib.net/doc/18802199/aluminium-steel-triclad-triclad-%C2%AE-joining-aluminium-to>. Accessed on 02 June 2019.

[28] Triplate® Transition Joints. Available on: <https://continentalsteel.com/triplate-transition-joints/>. Accessed on 02 June 2019.

[29] ANCIOGLU, K.N. Corrosion and protection of aluminum alloys in seawater. In: FÉRON, D. **Corrosion behaviour and protection of copper and aluminium alloys in seawater**. European Federation of Corrosion Publications – Number 50. England: Woodhead Publishing Limited, pp. 145-155, 2007.

[30] EZUBER, H.; EL-HOUD, A.; EL-SHAWESH, F. A study on the corrosion behavior of aluminum alloys in seawater. **Materials and Design**, vol. 29, pp. 801-805, 2008.

[31] HAN, J.H.; AHN, J.P.; SHIN, M.C. Effect of interlayer thickness on shear deformation behavior of AA5083 aluminum alloy/SS41 steel plates manufactured by explosive welding. **Journal of Materials Science**, vol. 38, pp. 13-18, 2003.

[32] ACARER, M.; DEMIR, B. An investigation of mechanical and metallurgical properties of explosive welded aluminum-dual phase steel. **Materials Letters**, vol. 62, pp. 4158-4160, 2008.

[33] LIU, W.; MA, J.; ATABAKI, M.M.; KOVACEVIC, R. Joining of advanced high-strength steel to AA6061 alloy by using Fe/Al structural transition joint. **Materials and Design**, vol. 68, pp. 146-157, 2015.

[34] VEMANABOINA, H.; EDISON, G.; AKELLA, S.; BUDDU, R.K. Effect of Residual Stresses of GTA Welding for Dissimilar Materials. **Materials Research**, vol. 21, n. 4, pp. 1-7, 2018.

[35] POTESSER, M.; SCHOEBERL, T.; ANTREKOWITSCH, H.; BRUCKNER, J. The Characterization of the Intermetallic Fe-Al Layer of Steel-Aluminum Weldings. **EPD Congress**, pp. 167-176, 2006.

[36] KAH, P.; SHRESTHA, M.; MARTIKAINEN, J. Trends in Joining Dissimilar Metals by Welding. **Applied Mechanics and Materials**, vol. 440, pp. 269-276, 2014.

[37] HATANO, R.; OGURA, T.; MATSUDA, T.; SANO, T.; HIROSE, A. Relationship between intermetallic compound layer thickness with deviation and interfacial strength for dissimilar joints of aluminum alloy and stainless steel. **Materials Science and Engineering A**, vol. 735, pp. 361-366, 2018.

[38] MASSALSKI, T.B.; OKAMOTO, H.; SUBRAMANIAN, P.R.; KACPRZAK, L. **Binary alloys phase diagrams**. 2nd ed. Park (Ohio): ASM International, 1990.

[39] MEHTA, K.P. A review on friction-based joining of dissimilar aluminum-steel joints. **Journal of Materials Research**, vol. 34, n.1, pp. 78-96, 2018.

[40] MCKAMEY, C.G. Iron Aluminides. In: STOLOFF, N.S.; SIKKA, V.K. **Physical metallurgy and processing of intermetallic compounds**. Chapman and Hall, pp. 351-391, 1996.

[41] ZAMANZADE, M.; BARNOUSH, A.; MOTZ, C. A review on the properties of iron aluminide intermetallics. **Crystals**, vol. 6, 10, 29 p., 2016.

[42] CINCA, N.; LIMA, C.R.C.; GUILEMANY, J.M. An overview of intermetallics research and application: Status of thermal spray coatings. **Journal of Materials Research and Technology**, vol. 2, pp. 75-86, 2013.

[43] MATYSIK, P.; JÓZWIAK, S.; CZUJKO, T. Characterization of low-symmetry structures from phase equilibrium of Fe-Al system – Microstructures and mechanical properties. **Materials**, vol. 8, pp. 914-931, 2015.

[44] KOBAYASHI, S.; YAKOU, T. Control of intermetallic compound layers at interface between steel and aluminum by diffusion-treatment. **Materials Science and Engineering A**, vol. 338, pp. 44-53, 2002.

[45] ILYUSHIN, A.S.; WALLACE, W.E. Structural and magnetic properties of the $Fe_{3-x}Mn_xAl$ system. **Journal of Solid State Chemistry**, vol. 17, pp. 385-387, 1976.

[46] STEIN, F.; VOGEL, S.C.; EUMANN, M.; PALM, M. Determination of the crystal structure of the ε phase in the Fe-Al system by high-temperature neutron diffraction. **Intermetallics**, vol. 18, pp. 150-156, 2010.

[47] CHUMAK, I.; RICHTER, K.W.; EHRENBERG, H. Redetermination of iron dialuminide, $FeAl_2$. **Acta Crystallographica**, Section C, vol. 66, pp. i87-i88, 2010.

[48] BURKHARDT, U.; GRIN, Y.; ELLNER, M. Structure refinement of the iron-aluminium phase with the approximate composition Fe_2Al_5. **Acta Crystallographica**, Section B, vol. 50, pp. 313-316, 1994.

[49] BLACK, P.J. The structure of $FeAl_3$. **Acta Crystallographica**, vol. 8, pp. 43-48, 1855.

[50] YANG, J; LI, Y.L.; ZHANG, H.; GUO, W.; ZHOU, Y. Control of interfacial intermetallic compounds in Fe-Al joining by Zn addition. **Materials Science and Engineering A**, vol. 645, pp. 323-327, 2015.

[51] SCHNEIDER, J.; RADZILOWSKI, R. Welding of Very Dissimilar Materials (Fe-Al). **The Journal of the Minerals, Metals and Materials Society**, vol. 66, n.10, pp. 2123-2129, 2014.

[52] Solid-State Welding. In: Welding Science and Technology. **Welding Handbook**. 9th ed. American Welding Society, vol. 1, pp. 22-27, 2001.

[53] MANDAL, N.R. **Ship Construction and Welding**. 1st ed. Springer Series on Naval Architecture, Marine Engineering, Shipbuilding and Shipping, vol. 2, 2017. 332 p.

[54] MISHRA, R.S.; MA, Z.Y. Friction Stir Welding and Processing. **Materials Science and Engineering R**, vol. 50, pp. 1-78, 2005.

[55] PRATER, T. Solid-state joining of metal matrix composites: a survey of challenges and potential solutions. **Materials and Manufacturing Processes**, vol. 26, pp. 636-648, 2011.

[56] Friction Stir Welding. Available on: <https://hzg.de/institutes_platforms/materials_research/materials_mechanics/solid_state_joining_processes/techniques/index.php.en#tab-49>. Accessed on 31 March 2020.

[57] GIBSON, B.T.; LAMMLEIN, D.H.; PRATER, T.J.; LONGHURST, W.R.; COX, C.D.; BALLUN, M.C.; DHARMARAJ, K.J.; COOK, G.E.; STRAUSS, A.M. Friction Stir Welding: Process, automation, and control. **Journal of Manufacturing Processes**, vol. 16, pp. 56-73, 2014.

[58] WAN, L.; HUANG, Y. Friction stir welding of dissimilar aluminum alloys and steels: a review. **The International Journal of Advanced Manufacturing Technology**, vol. 99, pp. 1781-1811, 2018.

[59] KIMAPONG, K.; WATANABE, T. Friction Stir Welding of Aluminum Alloy to Steel. **Welding Journal**, vol. 83, pp. 277S-282S, 2004.

[60] WANG, X.; PAN, Y.; LADOS, D.A. Friction Stir Welding of Dissimilar Al/Al and Al/Non-Al Alloys: A Review. **Metallurgical and Materials Transactions B**, vol. 49, pp. 2097-2117, 2018.

[61] ASM METALS HANDBOOK. **Properties and Selection: Nonferrous Alloys and Special Purpose Materials**, vol. 2, 1990. 3470 p.

[62] FERRARIS, S.; VOLPONE, L.M. Aluminum alloys in third millennium shipbuilding: materials, technologies, perspectives. In: **The Fifth International Forum on Aluminum Ships**, Tokyo, pp. 1-11, October 2005.

[63] VARGEL, C. **Corrosion of Aluminum**. 1st ed. France: Elsevier, 2004. 700p.

[64] RAMBABU, P.; PRASAD, E.; KUTUMBARAO, V.V.; WANHILL, R.J.H. Aluminum alloys for aerospace applications. In: PRASAD, E.; WANHILL, R.J.H. **Aerospace Materials and Materials Technologies**. Indian Institute of Metals Series, Singapore, pp. 29-52, 2017.

[65] Aluminium alloys in marine applications. **Alcan Marine**. Available on: <http://www.almet-marine.com/images/clients/EN/Aluminium-users-guide/Ch03-aluminium-alloys-in-marine-applications.pdf>. Accessed on 03 June 2019.

[66] SAVI, B.M. Desenvolvimento tecnológico para soldagem MIG de ligas de alumínio 5083 H116. 103 p. Dissertação (Mestrado em Ciência e Engenharia de Materiais). Universidade Federal de Santa Catarina, Florianópolis, 2014.

[67] ENGLER, O.; MILLER-JUPP, S. Control of Second-Phase Particles in the Al-Mg-Mn Alloy AA5083. **Journal of Alloys and Compounds**, Germany, vol. 689, pp. 998-1010, 2016.

[68] TRONCI, A.; MCKENZIE, R.; LEAL, R.M.; RODRIGUES, D.M. Microstructural and mechanical characterisation of 5XXX-H111 friction stir

welded tailored blanks. **Science and Technology of Welding and Joining**, vol. 16, n. 5, pp. 433-439, 2011.

[69] PELL, M.; STEUWER, A.; PREUSS, M.; WITHERS, P.J. Microstructure, mechanical properties and residual stresses as a function of welding speed in aluminium AA5083 friction stir welds. **Acta Materialia**, vol. 51, pp. 4791-4801, 2003.

[70] Steels for Shipbuilding. Available on: <http://ispatguru.com/steels-for-shipbuilding/>. Accessed on 31 October 2018.

[71] GALANTE, H.A. Seleção de materiais no design e indústria náuticos. 2003. 115 f. Dissertação (Mestrando em Engenharia de Materiais) – Rede Temática em Engenharia de Materiais, Universidade Federal de Ouro Preto, 2003.

[72] DNV GL AS. **Offshore Standard: Metallic Materials**, DNVGL-OS-B101. 2015.

[73] The Chinese Society for Metals. **HSLA Steels 2015, Microalloying 2015 and Offshore Engineering Steels 2015.** 1st ed. The Minerals, Metals and Materials Series, 2016. 1147 p.

[74] COELHO DA SILVA, R.; GHENO, S.M. Caracterização mecânica e estrutural do aço ASTM A131 classe DH36 em comparação com aço ASTM A36 utilizado para projetos estruturais. **Revista Academus**, vol. 5, 2017. 9 p.

[75] LEHTO, P.; ROMANOFF, J., REMES, H.; SARIKKA, T. Characterisation of local grain size variation of welded structural steel. **Welding in the World**, vol. 60, pp. 673-688, 2016.

[76] Lloyd’s Rules for the Manufacture, Testing and Certification Materials. **Lloyd’s Register**. Available on:

<https://www.cdinfo.lr.org/information/documents%5CRules%5CMATERIALS%5C2014%20MATERIALS%5CNotices/14%20materials%20notice%201.pdf>. Accessed on 19 July 2019.

[77] REYNOLDS, A.P.; TANG, W.; POSADA, M.; DELOACH, J. Friction stir welding of DH36 steel. **Science and Technology of Welding and Joining**, vol. 8, pp. 455-460, 2003.

[78] ASTM STANDARD. B209M-14 Standard Specification for Aluminum and Aluminum-Alloy Sheet and Plate. **ASTM INTERNATIONAL**, 2014.

[79] ASTM STANDARD. E3-11 Standard Guide for Preparation Metalllographic Specimens. **ASTM INTERNATIONAL**, 2011.

[80] ASTM STANDARD E112-13 Standard Test Method for Determining Average Grain Size. **ASTM INTERNATIONAL**, 2013.

[81] ASTM STANDARD. E384-17 Standard Test Method for Microindentation Hardness of Materials. **ASTM INTERNATIONAL**, 2017.

[82] TOBY, B.H.; VON DREELE, R.B. GSAS-II: The genesis of a modern open-source all purpose crystallography software package. **Journal of Applied Crystallography**, vol. 46, pp. 544-549, 2013.

[83] SRM 674b. **X-Ray Powder Diffraction Intensity Set – Quantitative Powder Diffraction Standard**. National Institute of Standards and Technology, U.S. Department of Commerce: Gaithersburg, MD (2017).

[84] DEHGHANI, M.; AKBARI MOUSAVI, S.A.A.; AMADEH, A. Effects of welding parameters and tool geometry on properties of 3003-H18 aluminum alloy to mild steel friction stir weld. **Transactions of Nonferrous Metals Society of China**, vol. 23, pp. 1957-1965, 2013.

[85] LIU, X.; LAN, S.; NI, S. Analysis of process parameters effects on friction stir welding of dissimilar aluminum alloy to advanced high strength steel. **Materials and Design**, vol. 59, pp. 50-62, 2014.

[86] DAS, H.; BASAK, S.; DAS, G.; PAL, T.K. Influence of energy induced from processing parameters on the mechanical properties of friction stir welded lap joint of aluminum to coated steel sheet. **International Journal of Advanced Manufacturing Technology**, vol. 64, pp. 1653-1661, 2013.

[87] MOVAHEDI, M.; KOKABI, A.H.; SEYED REIHANI, S.M.; NAJAFI, H. Mechanical and microstructural characterization of Al-5083/St-12 lap joints made by friction stir welding. **Procedia Engineering**, vol. 10, pp. 3297-3303, 2011.

[88] ZHENG, Q.; FENG, X.; SHEN, Y.; HUANG, G.; ZHAO, P. Dissimilar friction stir welding of 6061 Al to 316 stainless steel using Zn as a filler metal. **Journal of Alloys and Compounds**, vol. 686, pp. 693-701, 2016.

[89] POURALI, M.; ABDOLLAH-ZADEH, A.; SAEID, T.; KARGAR, F. Influence of welding parameters on intermetallic compounds formation in dissimilar steel/aluminum friction stir welds. **Journal of Alloys and Compounds**, vol. 715, pp. 1-8, 2017.

[90] XIONG, J.T.; LI, J.L.; QIAN, J.W.; ZHANG, F.S.; HUANG, W.D. High strength lap joint of aluminium and stainless steels fabricated by friction stir welding with cutting pin. **Science and Technology of Welding and Joining**, vol. 17, pp. 196-201, 2012.

[91] KUMAR, K.; KAILAS, S.V. The role of friction stir welding tool on material flow and weld formation. **Materials Science and Engineering A**, vol. 485, pp. 367-374, 2008.

[92] HELAL, Y.; BOUMERZOUG, Z.; FELLAH, L. Microstructural evolution and mechanical properties of dissimilar friction stir lap welding aluminum alloy 6061-T6 to ultra low carbon steel. **Energy Procedia**, vol. 157, pp. 208-215, 2019.

[93] RAO, D.; HUBER, K.; HEERENS, J.; DOS SANTOS, J.F.; HUBER, N. Asymmetric mechanical properties and tensile behaviour prediction of aluminum alloy 5083 friction stir welding joints. **Materials Science and Engineering A**, vol. 565, pp. 44-50, 2013.

[94] FONDA, R.W.; BINGERT, J.F. COLLIGAN, K.J. Development of grain structure during friction stir welding. **Scripta Materialia**, vol. 51, pp. 243-248, 2004.

[95] YAZDIPOUR, A.; SHAFIEI, A.; DEHGHANI, K. Modeling the microstructural evolution and effect of cooling rate on the nanograins formed during the friction stir processing of Al5083. **Materials Science and Engineering A**, vol. 527, pp. 192-197, 2009.

[96] KIMAPONG, K.; WATANABE, T. Lap joint of A5083 aluminum alloy and SS400 steel by friction stir welding. **Materials Transactions**, vol. 46, pp. 835-841, 2005.

[97] SCOTTO D’ANTUONO, D.; GAIES, J.; GOLUMBFSKIE, W.; TAHERI, M.L. Direct measurement of the effect of cold rolling on β phase precipitation kinetics in 5xxx series aluminum alloys. **Acta Materialia**, vol. 123, pp. 264-271, 2017.

[98] YAN, J.; HODGE, A.M. Study of β precipitation and layer structure formation in Al 5083: The role of dispersoids and grain boundaries. **Journal of Alloys and Compounds**, vol. 703, pp. 242-250, 2017.

[99] BOUAYAD, A.; GEROMETTA, C.; BELKEBIR, A.; AMBARI, A. Kinetic interactions between solid iron and molten aluminium. **Materials Science and Engineering A**, vol. 363, pp. 53-61, 2003.

[100] SPRINGER, H.; KOSTKA, A.; PAYTON, E.J.; RAABE, D.; KAYSSER-PYZALLA, A.; EGGELER, G. On the formation and growth of intermetallic phases during interdiffusion between low-carbon steel and aluminum alloys. **Acta Materialia**, vol. 59, pp. 1586-1600, 2011.

[101] SPRINGER, H.; SZCZEPANIAK, A.; RAABE, D. On the role of zinc on the formation and growth of intermetallic phases during interdiffusion between steel and aluminium alloys. **Acta Materialia**, vol. 96, pp. 203-211, 2015.

[102] SATO, Y.S.; URATA, M.; KOKAWA, H.; IKEDA, K. Hall-Petch relationship in friction stir welds of equal channel angular-pressed aluminium alloys. **Materials Science and Engineering A**, vol. 354, pp. 298-305, 2003.

[103] Finite Element Analysis of Adhesive Bonded Joints. **ENDEAVOS Innovations Inc.** Available on: <https://www.endeavos.com/finite-element-analysis/finite-element-analysis-of-adhesive-bonded-joints/>. Accessed on 20 May 2020.

[104] BUFFA, G.; CAMPANILE, G.; FRATINI, L.; PRISCO, A. Friction stir welding o flap joints: Influence of process parameters on the metallurgical and mechanical properties. **Materials Science and Engineering A**, vol. 519, pp. 19-26, 2009.

APPENDIX A

VISUAL INSPECTION OF THE WELDS' SURFACE

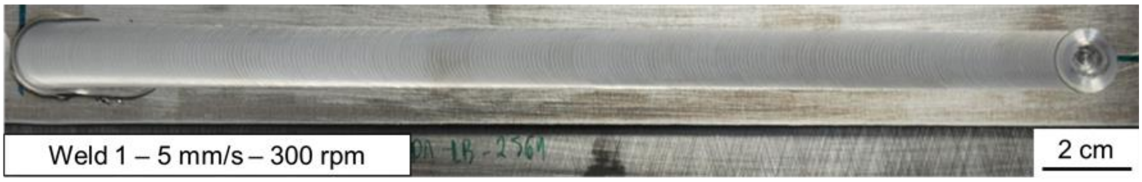
Weld 1 – 5 mm/s – 300 rpm

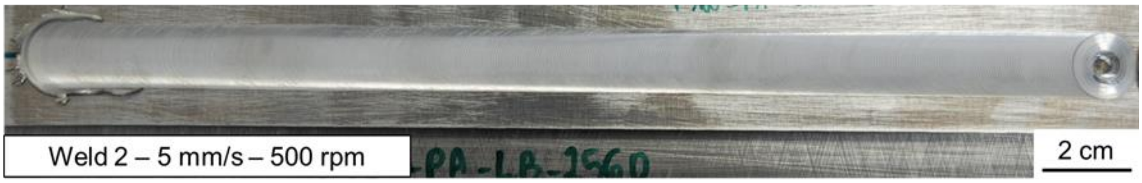
Weld 2 – 5 mm/s – 500 rpm

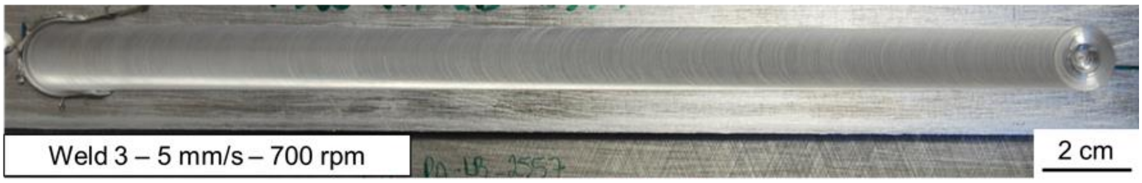
Weld 3 – 5 mm/s – 700 rpm

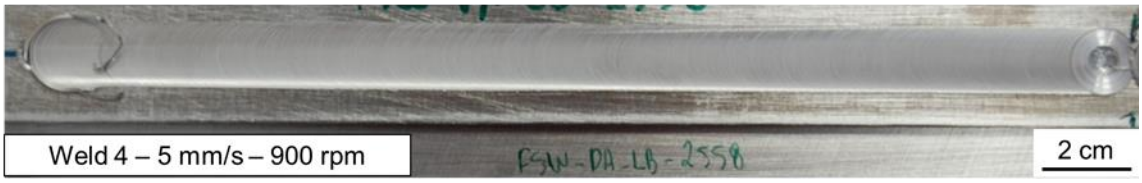
Weld 4 – 5 mm/s – 900 rpm
FSW-DA-LB-2558
2 cm

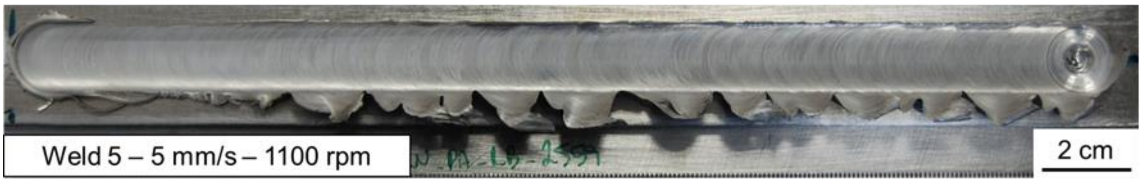
Weld 5 – 5 mm/s – 1100 rpm

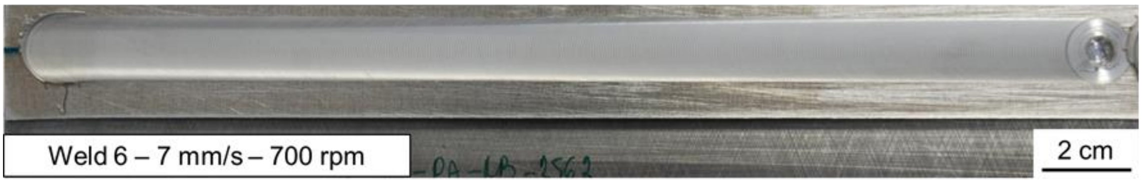
Weld 6 – 7 mm/s – 700 rpm

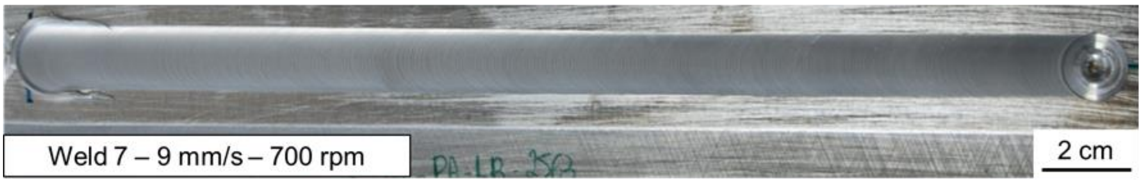
Weld 7 – 9 mm/s – 700 rpm

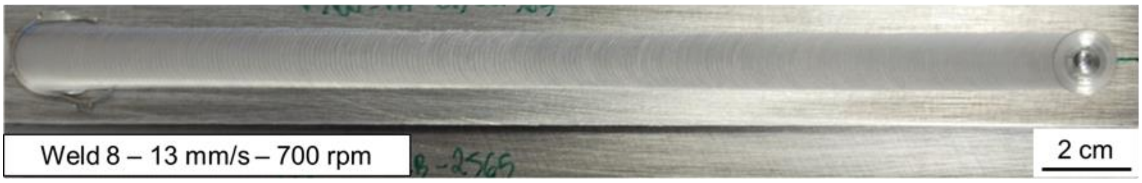
Weld 8 – 13 mm/s – 700 rpm

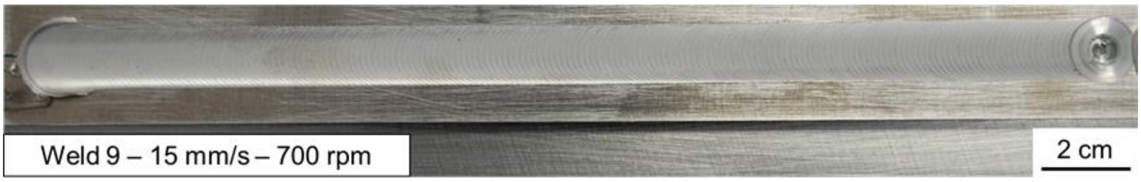
Weld 9 – 15 mm/s – 700 rpm

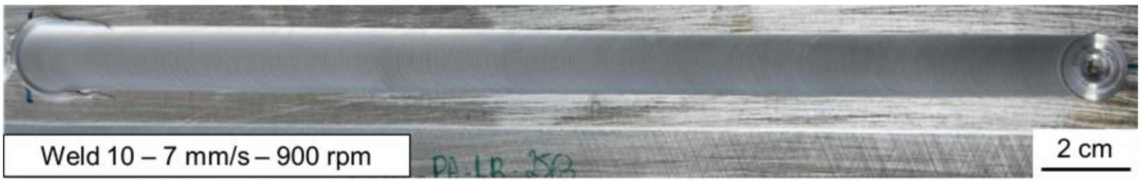
Weld 10 – 7 mm/s – 900 rpm

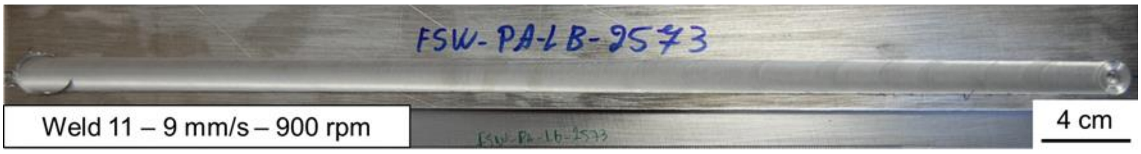
Weld 11 – 9 mm/s – 900 rpm
FSW-PA-LB-2573
4 cm

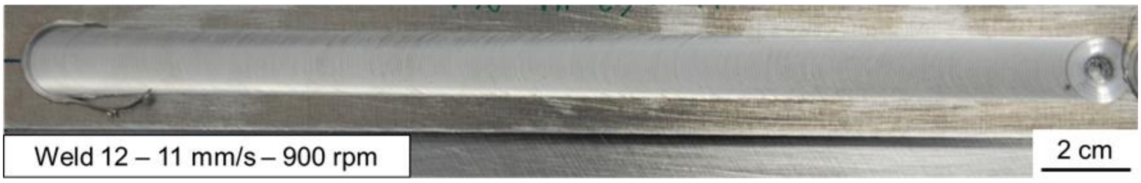
Weld 12 – 11 mm/s – 900 rpm

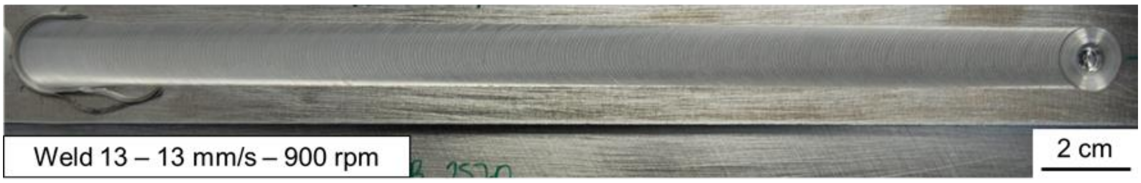
Weld 13 – 13 mm/s – 900 rpm

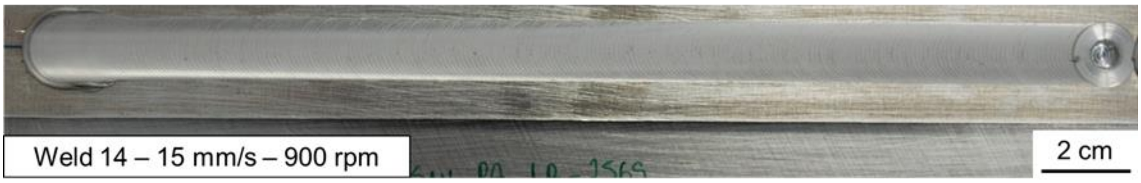
Weld 14 – 15 mm/s – 900 rpm

APPENDIX B

MACROSTRUCTURE OF THE WELDS

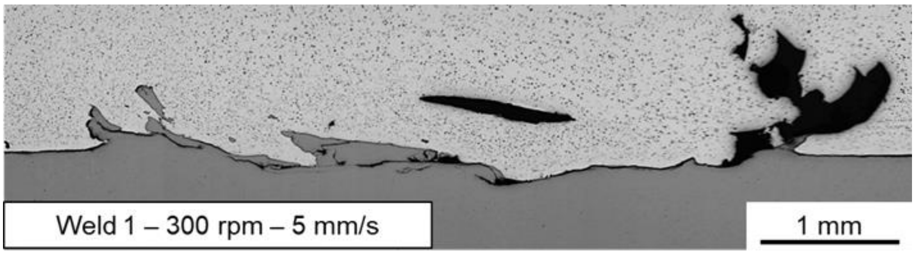
Weld 1 – 300 rpm – 5 mm/s
1 mm

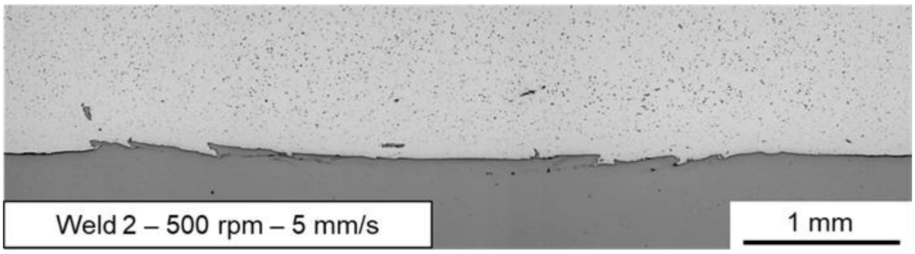
Weld 2 – 500 rpm – 5 mm/s
1 mm

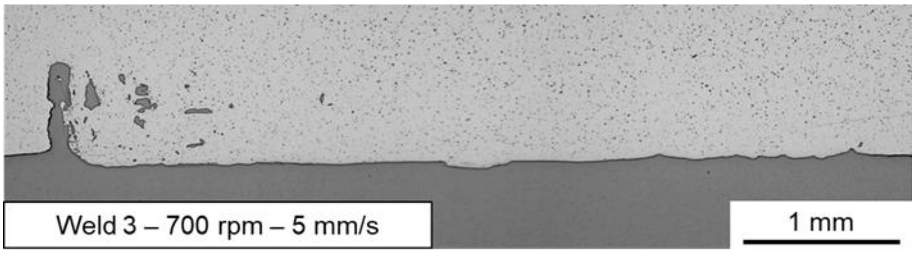
Weld 3 – 700 rpm – 5 mm/s
1 mm

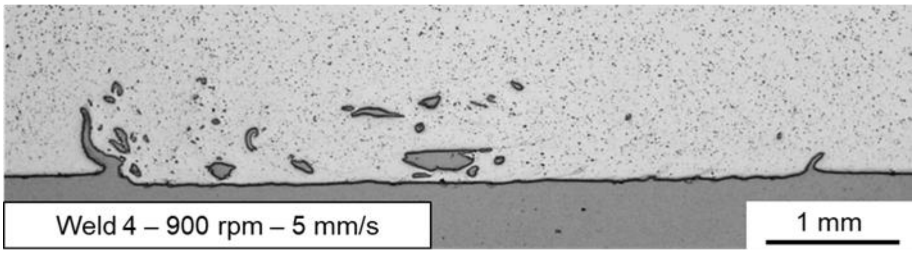
Weld 4 – 900 rpm – 5 mm/s
1 mm

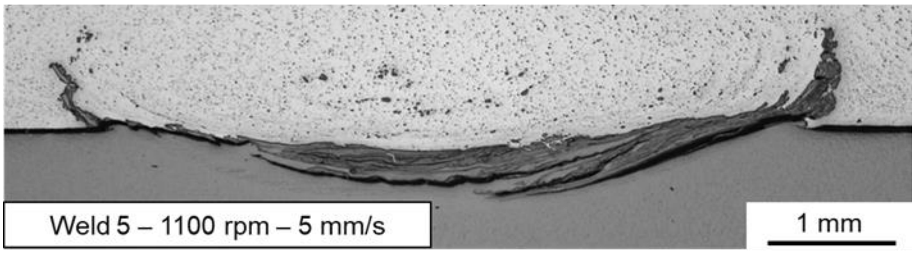
Weld 5 – 1100 rpm – 5 mm/s
1 mm

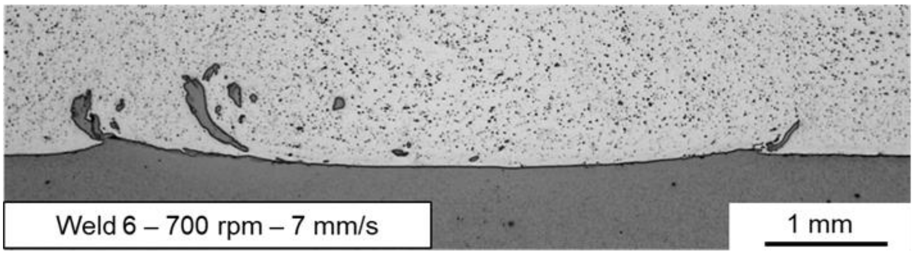
Weld 6 – 700 rpm – 7 mm/s
1 mm

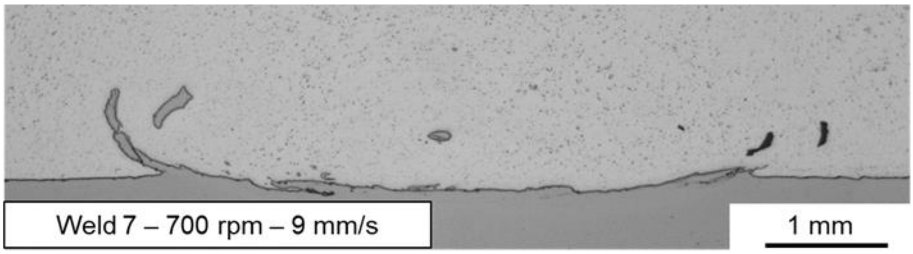
Weld 7 – 700 rpm – 9 mm/s
1 mm

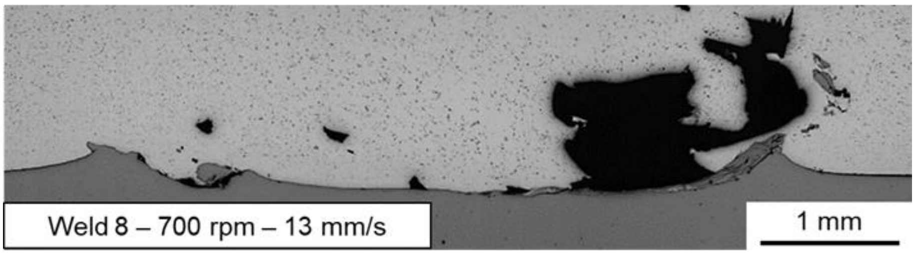
Weld 8 – 700 rpm – 13 mm/s
1 mm

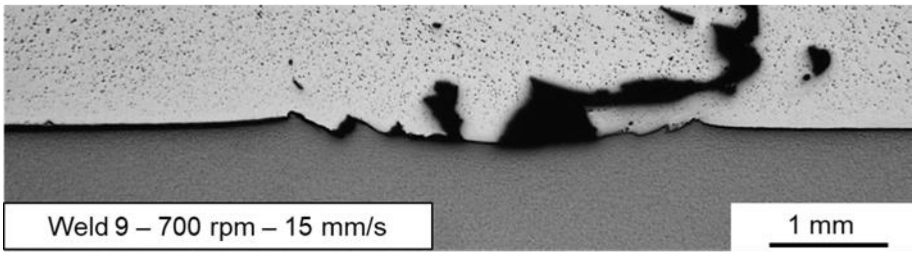
Weld 9 – 700 rpm – 15 mm/s
1 mm

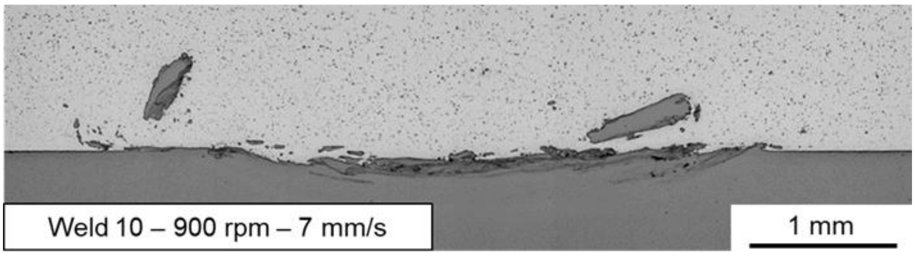
Weld 10 – 900 rpm – 7 mm/s
1 mm

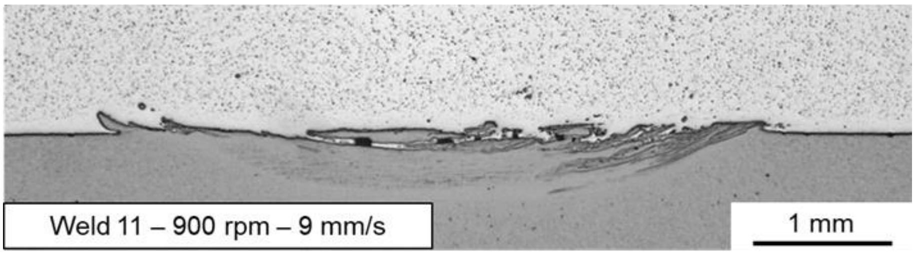
Weld 11 – 900 rpm – 9 mm/s
1 mm

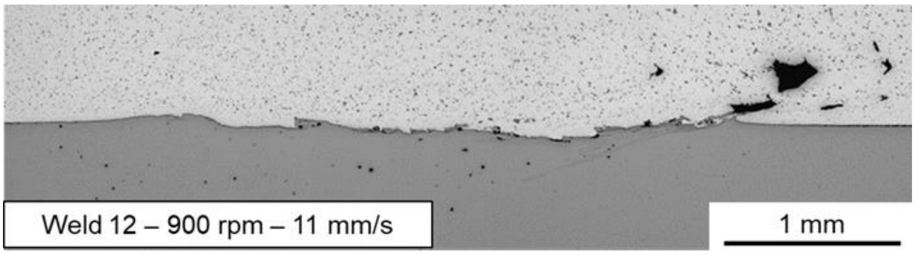
Weld 12 – 900 rpm – 11 mm/s
1 mm

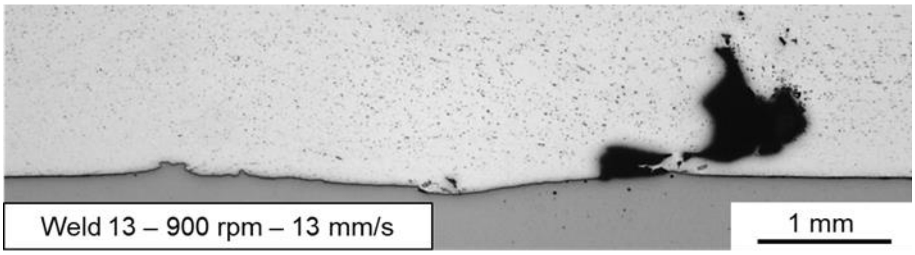
Weld 13 – 900 rpm – 13 mm/s
1 mm

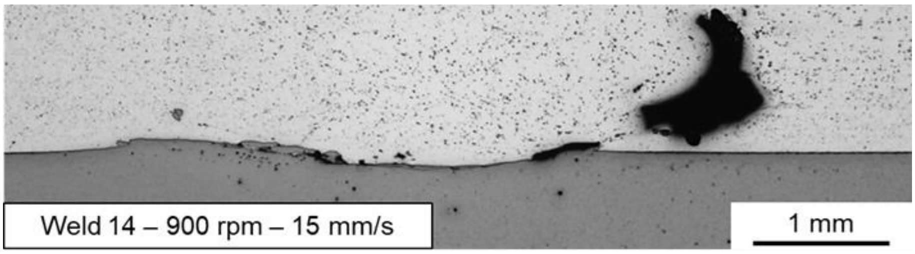
Weld 14 – 900 rpm – 15 mm/s
1 mm

APPENDIX C

MICROSTRUCTURE OF THE WELDS

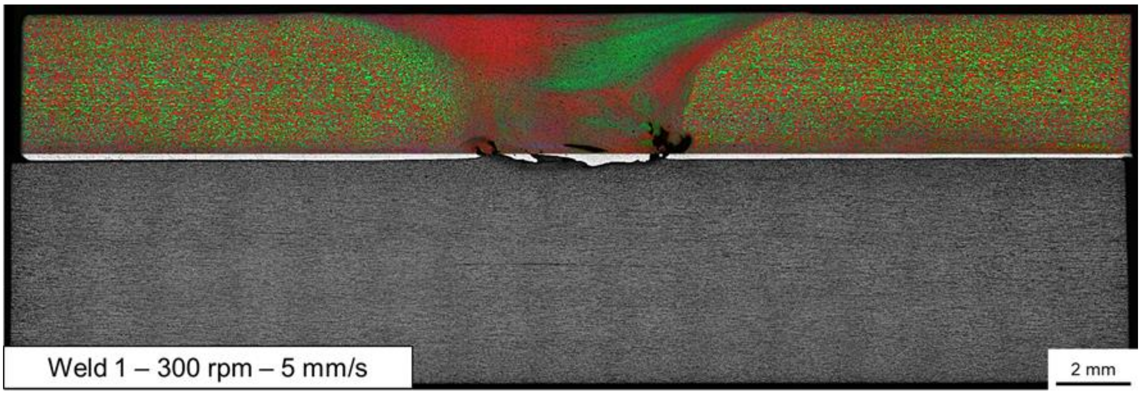

Weld 1 – 300 rpm – 5 mm/s

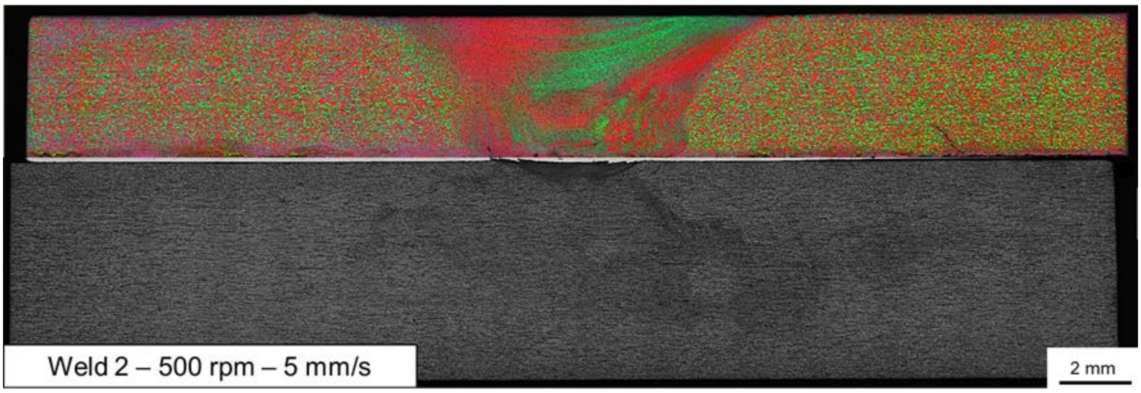

Weld 2 – 500 rpm – 5 mm/s

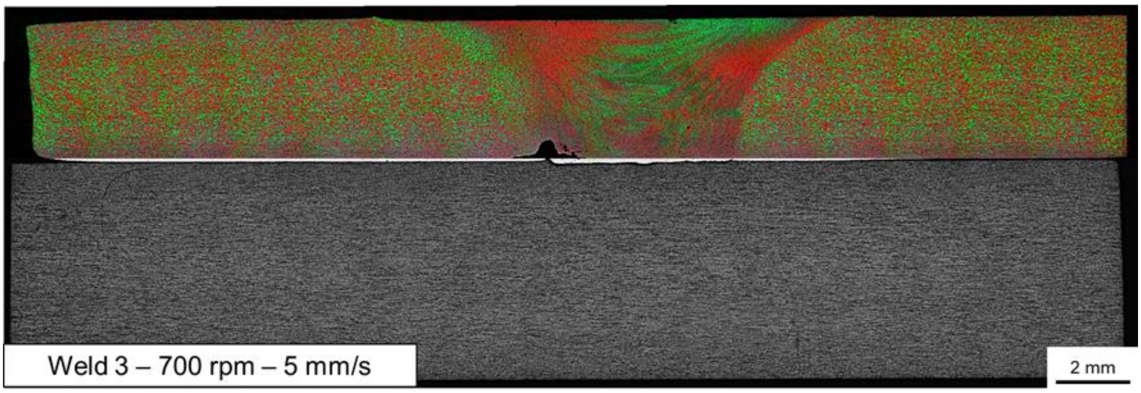

Weld 3 – 700 rpm – 5 mm/s

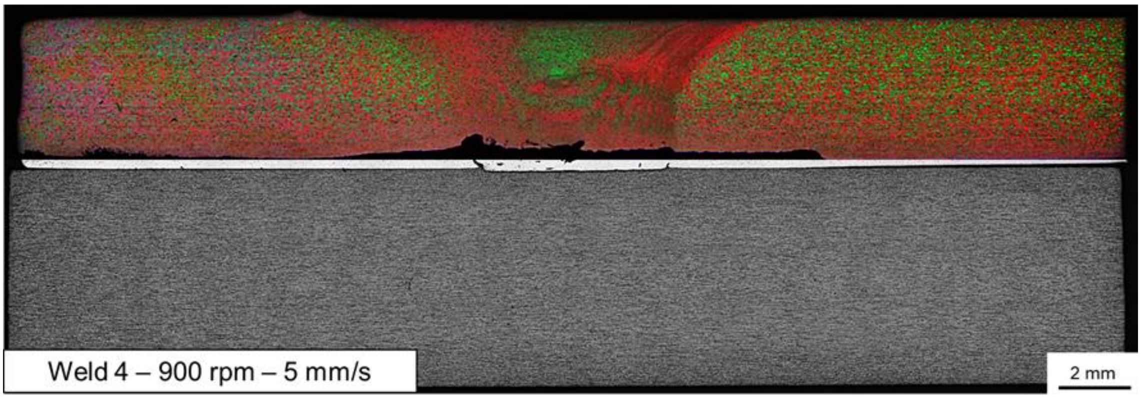

Weld 4 – 900 rpm – 5 mm/s

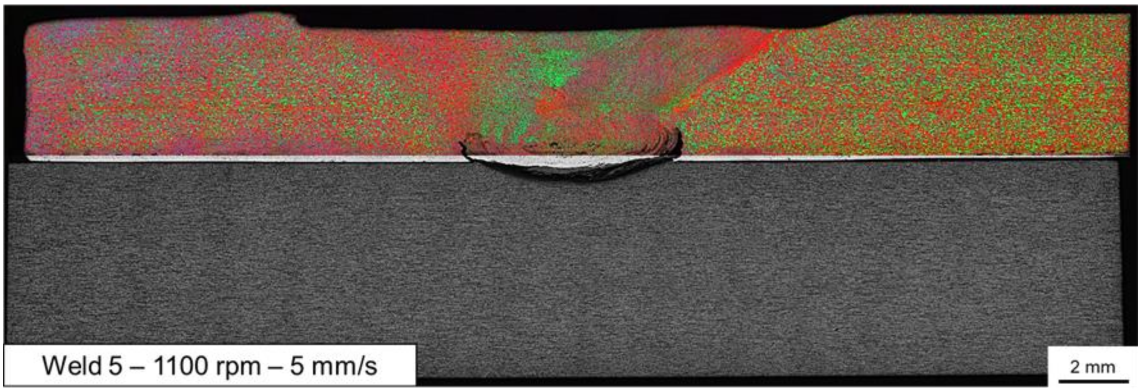
Weld 5 – 1100 rpm – 5 mm/s
2 mm

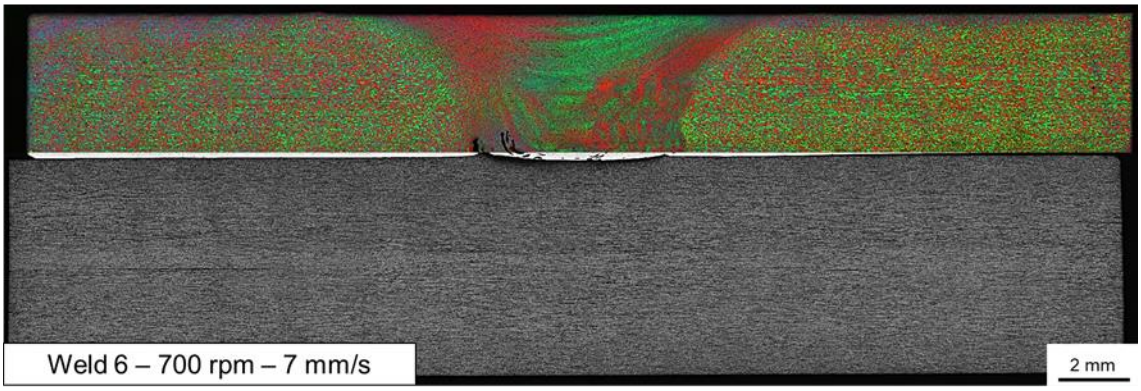
Weld 6 – 700 rpm – 7 mm/s
2 mm

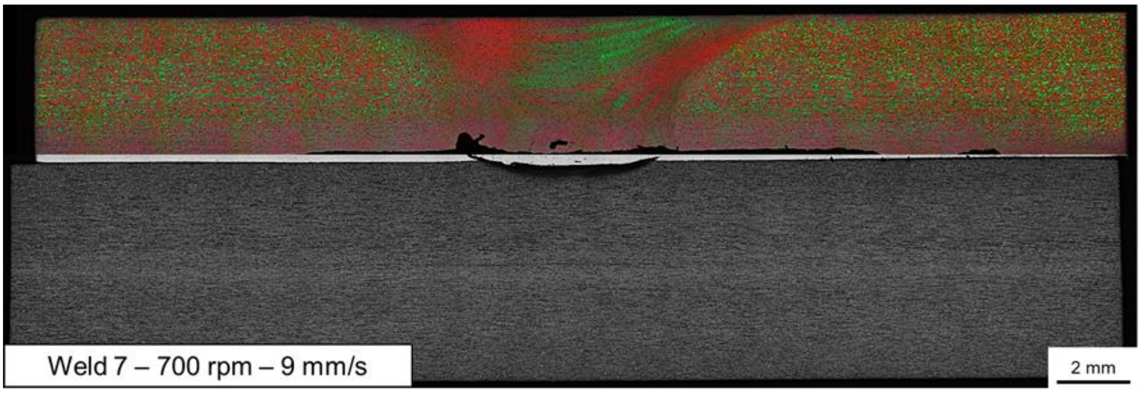
Weld 7 – 700 rpm – 9 mm/s
2 mm

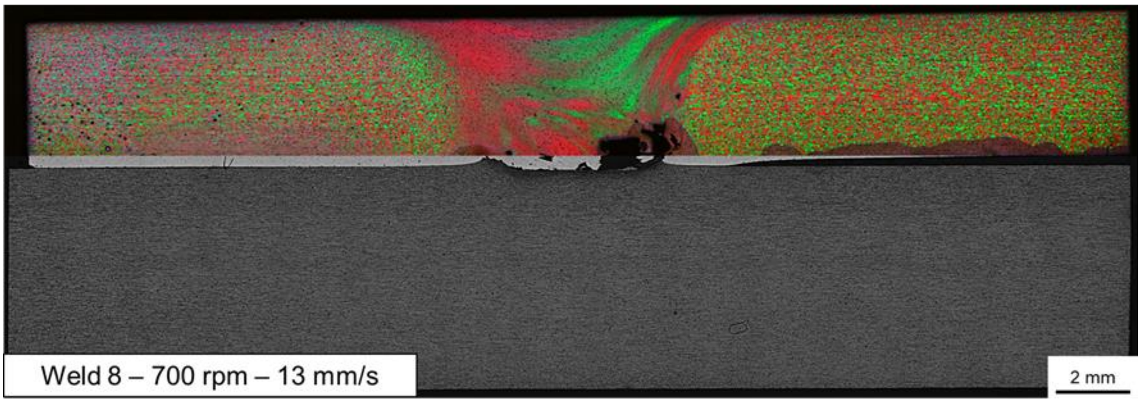
Weld 8 – 700 rpm – 13 mm/s
2 mm

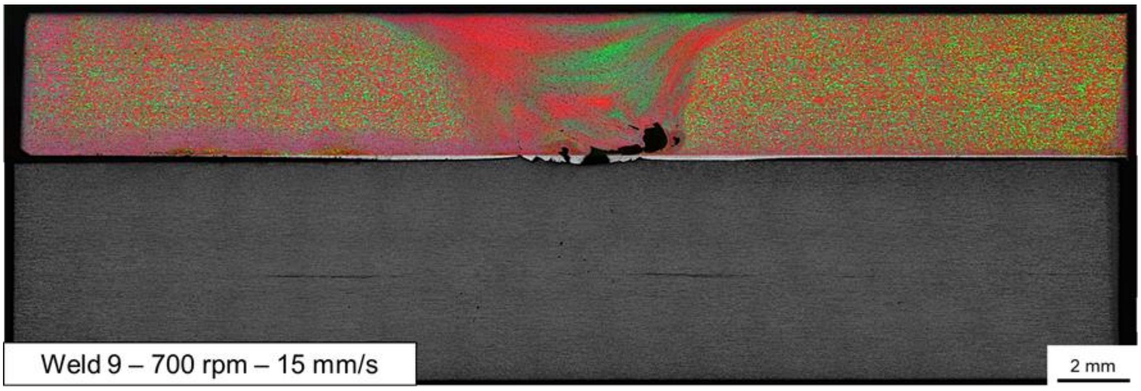
Weld 9 – 700 rpm – 15 mm/s

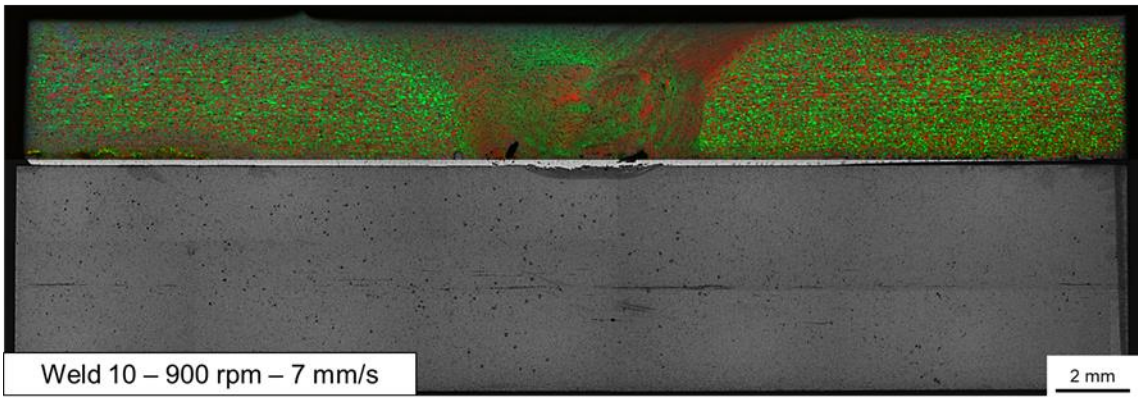
Weld 10 – 900 rpm – 7 mm/s

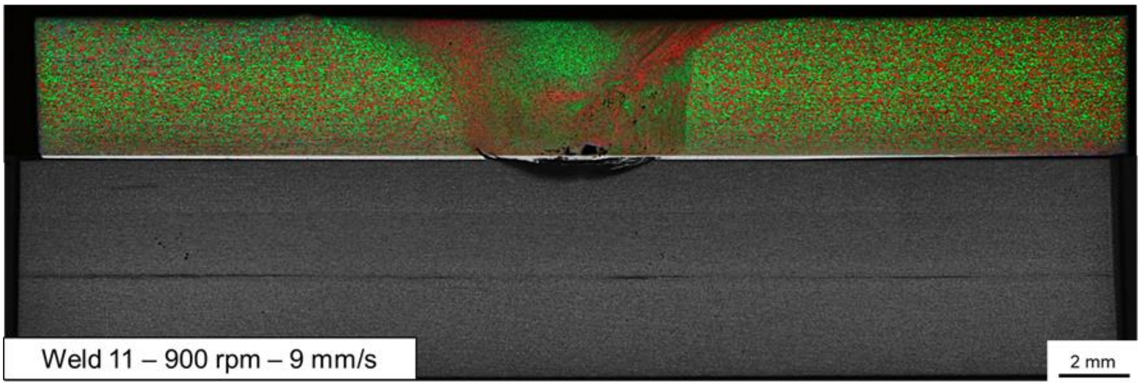
Weld 11 – 900 rpm – 9 mm/s

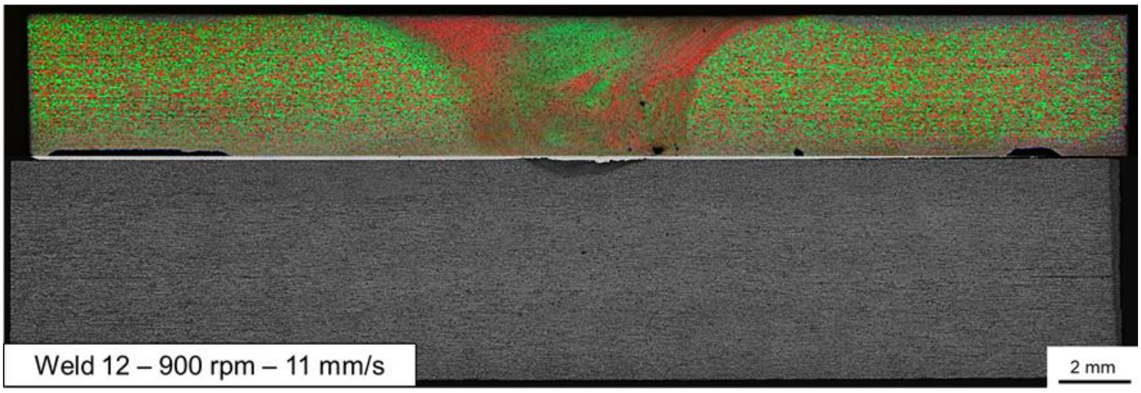
Weld 12 – 900 rpm – 11 mm/s

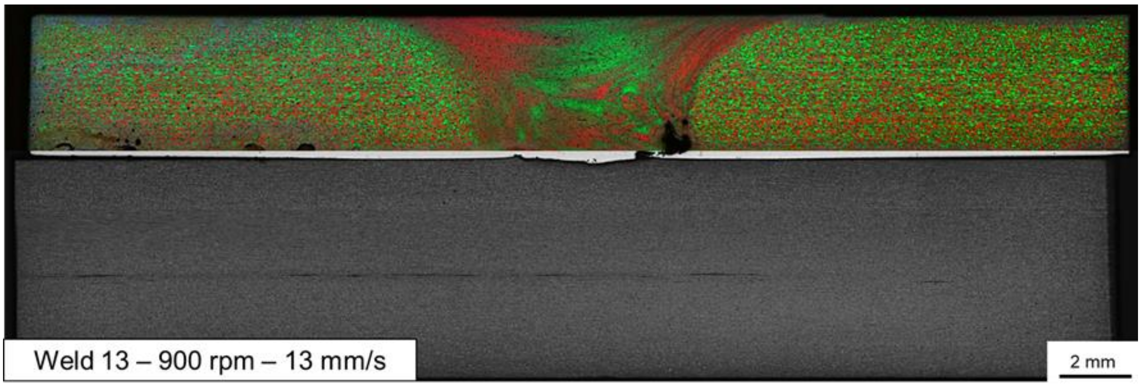
Weld 13 – 900 rpm – 13 mm/s
2 mm

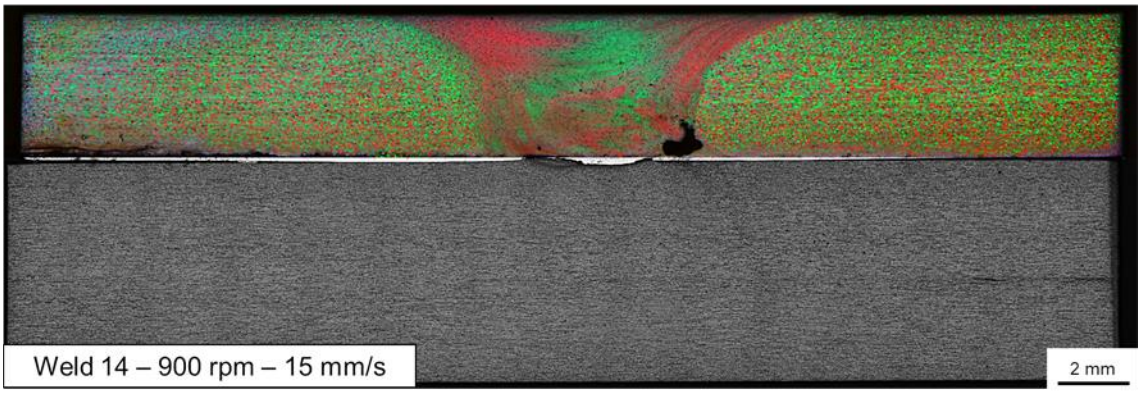
Weld 14 – 900 rpm – 15 mm/s
2 mm

APPENDIX D

INTERFACE OF THE WELDS

Weld 3 – 700 rpm – 5 mm/s

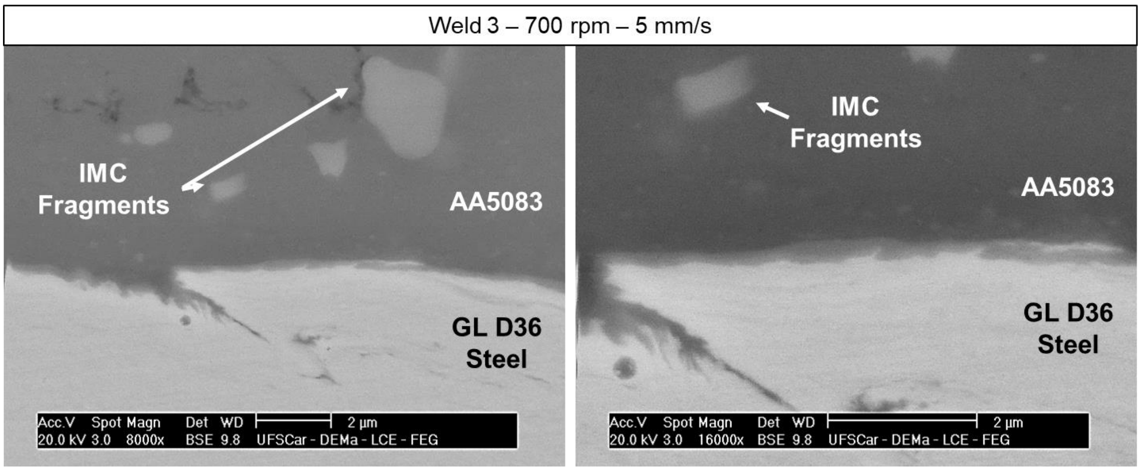
IMC Fragments
AA5083
GL D36 Steel
Acc.V Spot Magn Det WD 2 µm
20.0 kV 3.0 8000x BSE 9.8 UFSCar - DEMa - LCE - FEG
IMC Fragments
AA5083
GL D36 Steel
Acc.V Spot Magn Det WD 2 µm
20.0 kV 3.0 16000x BSE 9.8 UFSCar - DEMa - LCE - FEG

Weld 7 – 700 rpm – 9 mm/s

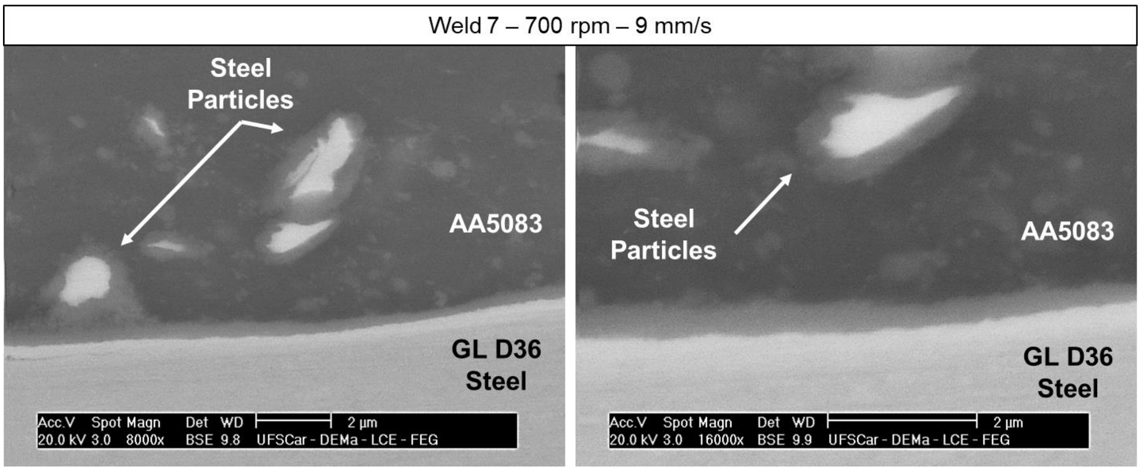
Steel Particles
AA5083
GL D36 Steel
Acc.V Spot Magn Det WD 2 µm
20.0 kV 3.0 8000x BSE 9.8 UFSCar - DEMa - LCE - FEG
Steel Particles
AA5083
GL D36 Steel
Acc.V Spot Magn Det WD 2 µm
20.0 kV 3.0 16000x BSE 9.9 UFSCar - DEMa - LCE - FEG

Weld 11 – 900 rpm – 9 mm/s

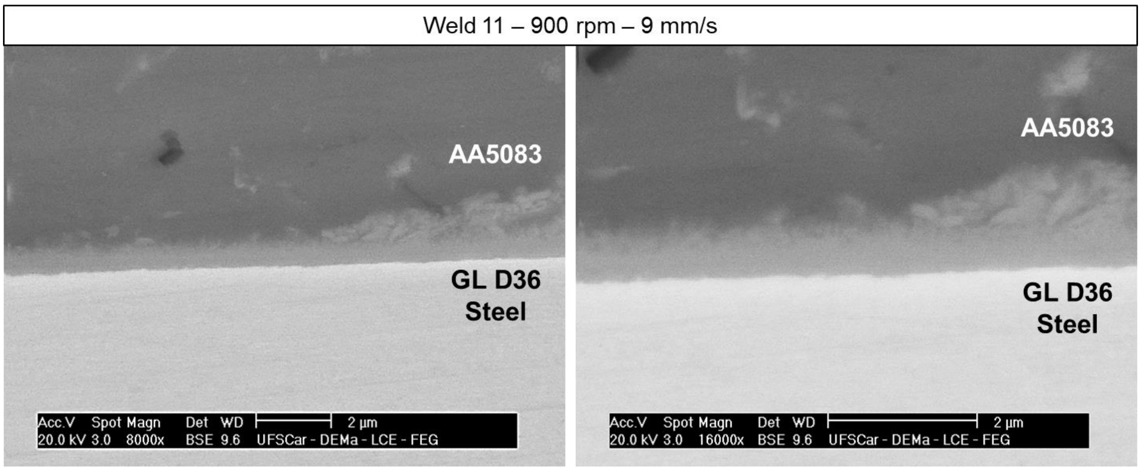
AA5083
GL D36 Steel
Acc.V Spot Magn Det WD 2 µm
20.0 kV 3.0 8000x BSE 9.6 UFSCar - DEMa - LCE - FEG
AA5083
GL D36 Steel
Acc.V Spot Magn Det WD 2 µm
20.0 kV 3.0 16000x BSE 9.6 UFSCar - DEMa - LCE - FEG

APPENDIX E

SAMPLES AFTER LAP SHEAR TENSILE TEST

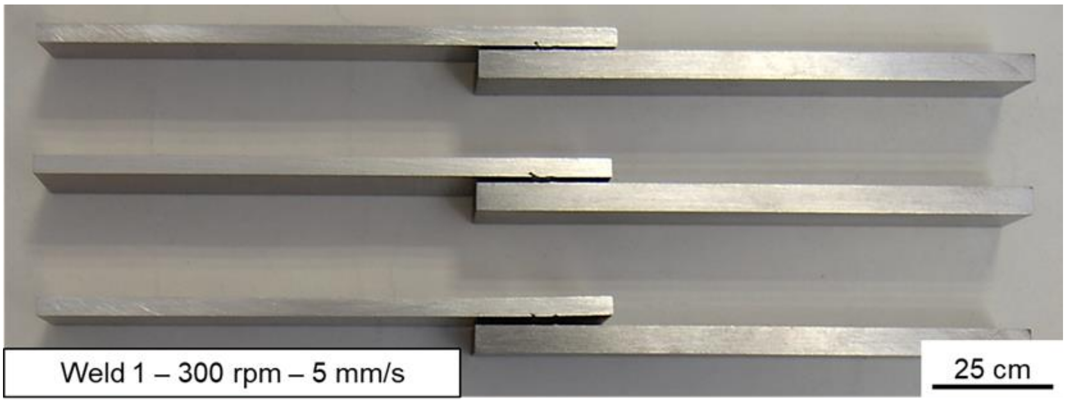

Weld 1 – 300 rpm – 5 mm/s

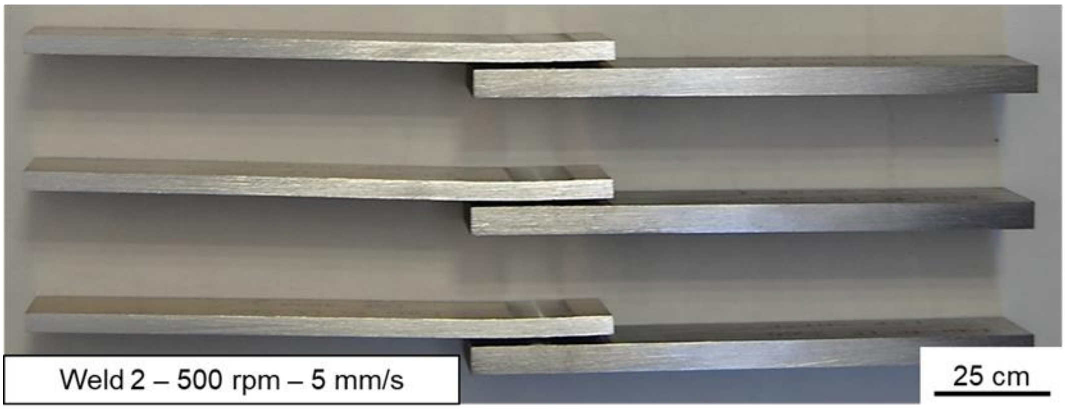

Weld 2 – 500 rpm – 5 mm/s

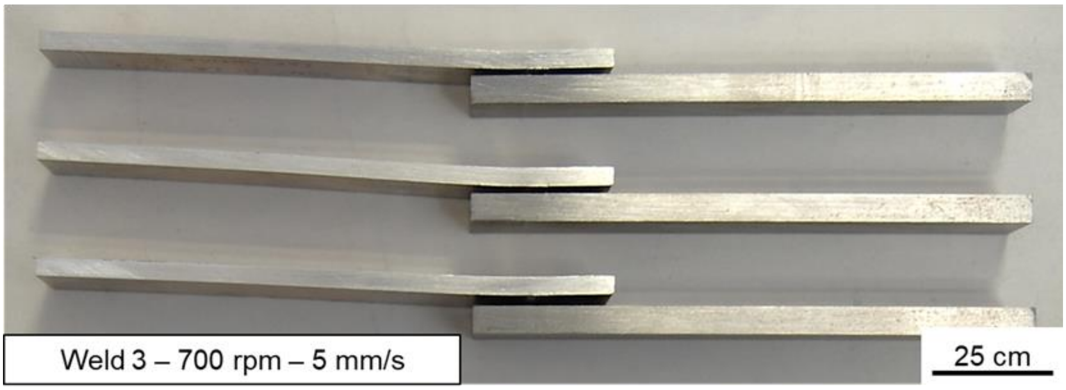

Weld 3 – 700 rpm – 5 mm/s

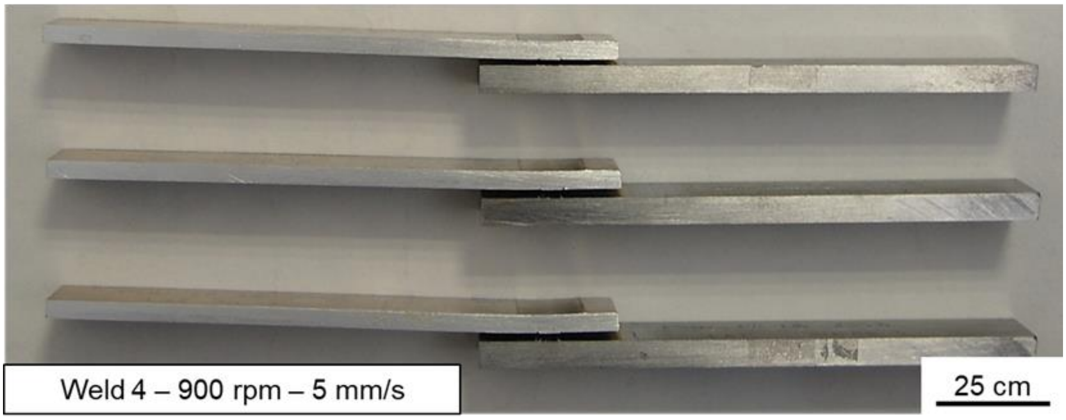

Weld 4 – 900 rpm – 5 mm/s

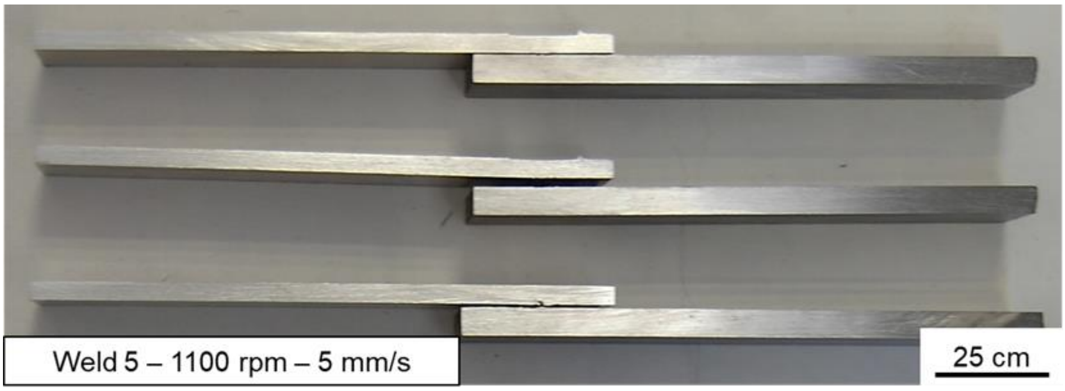
Weld 5 – 1100 rpm – 5 mm/s

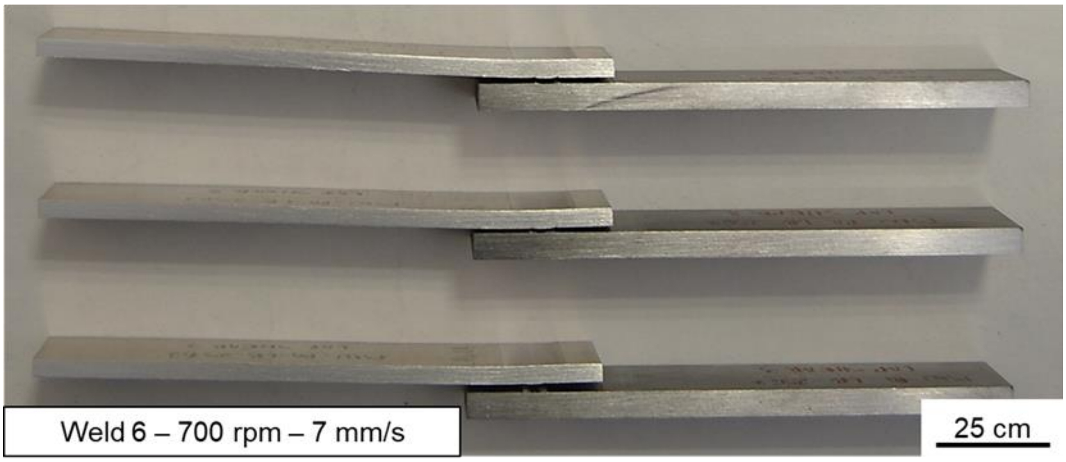
Weld 6 – 700 rpm – 7 mm/s

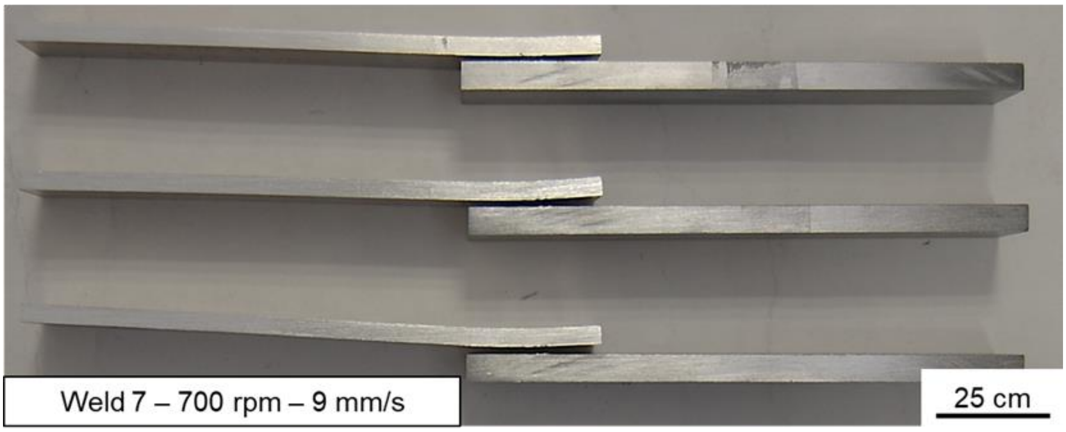
Weld 7 – 700 rpm – 9 mm/s

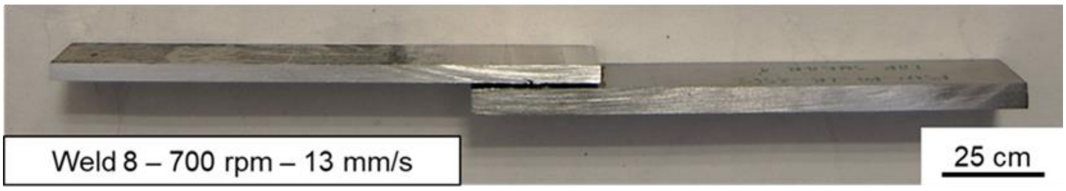
Weld 8 – 700 rpm – 13 mm/s

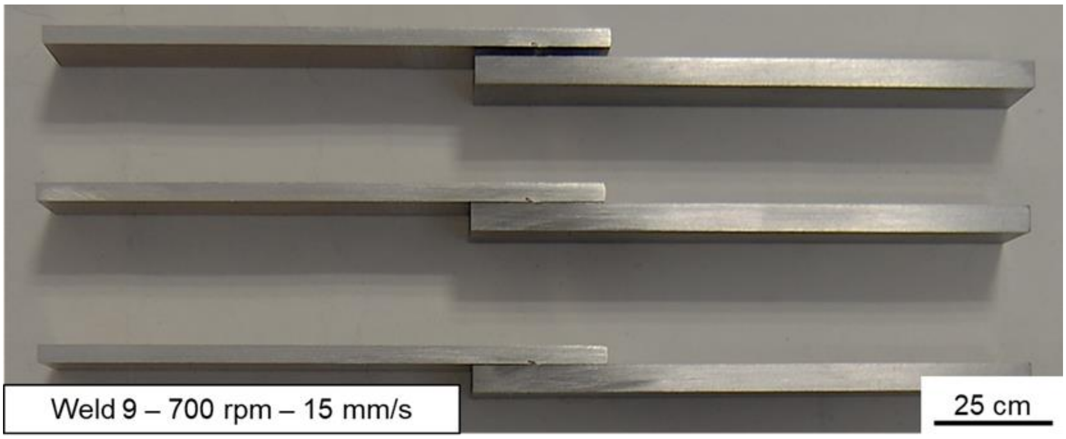
Weld 9 – 700 rpm – 15 mm/s

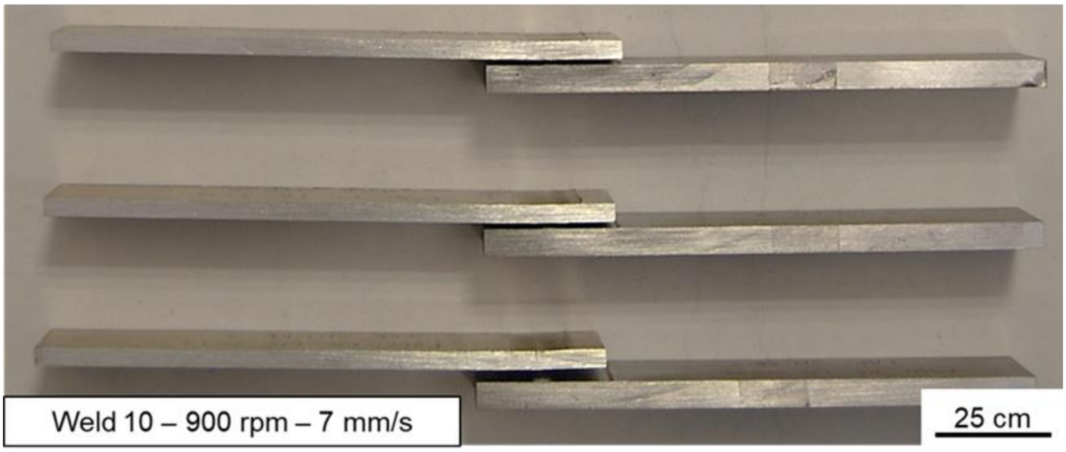
Weld 10 – 900 rpm – 7 mm/s

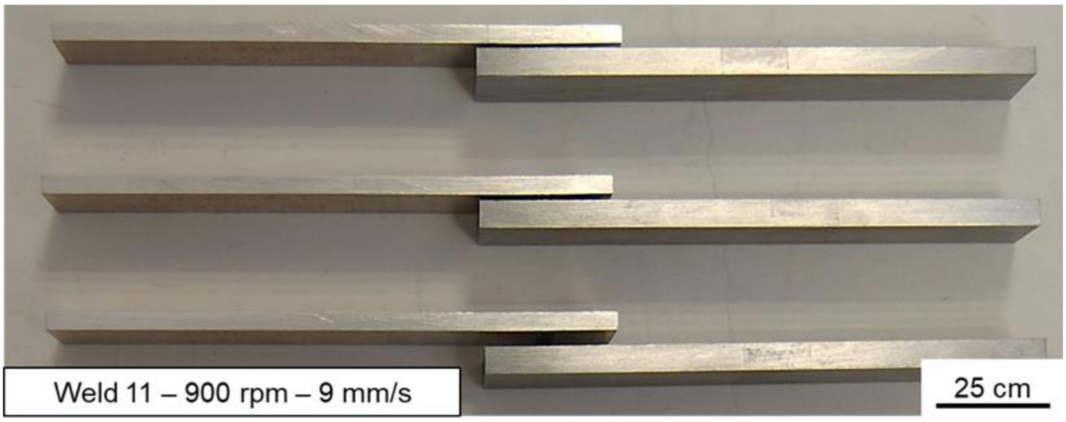
Weld 11 – 900 rpm – 9 mm/s

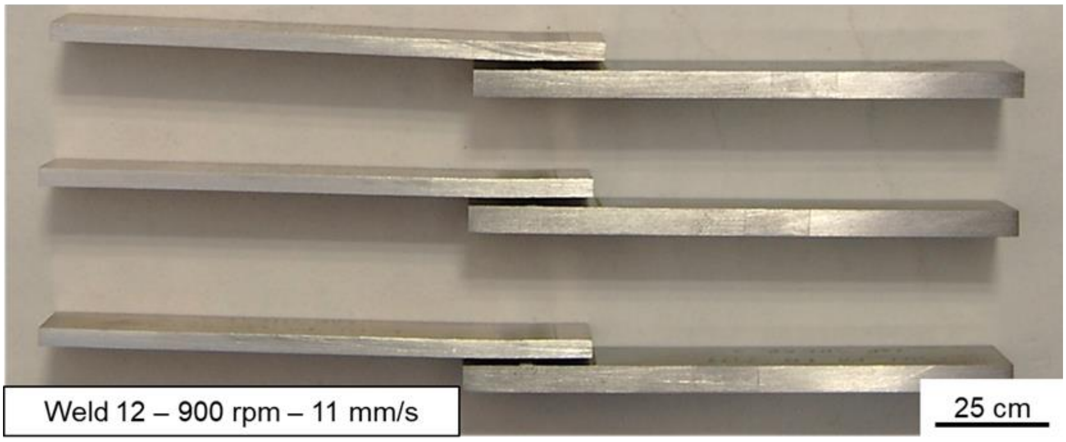
Weld 12 – 900 rpm – 11 mm/s

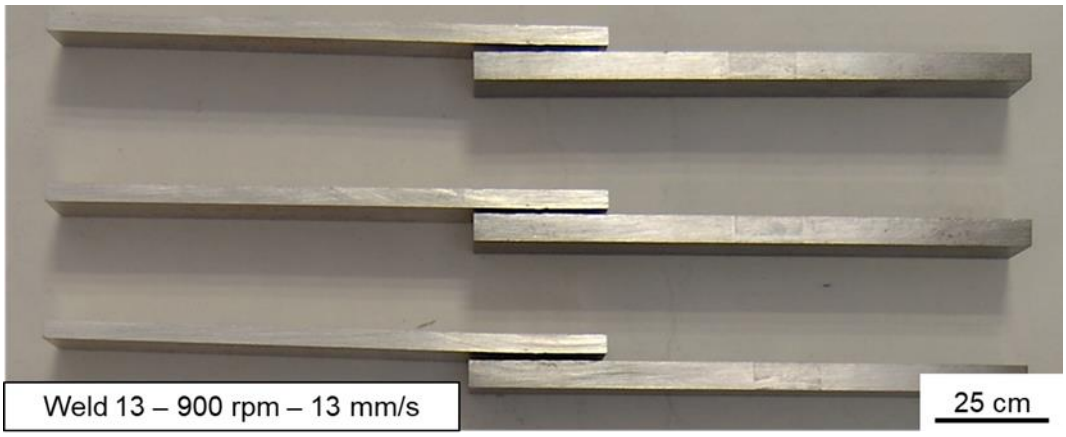
Weld 13 – 900 rpm – 13 mm/s
25 cm

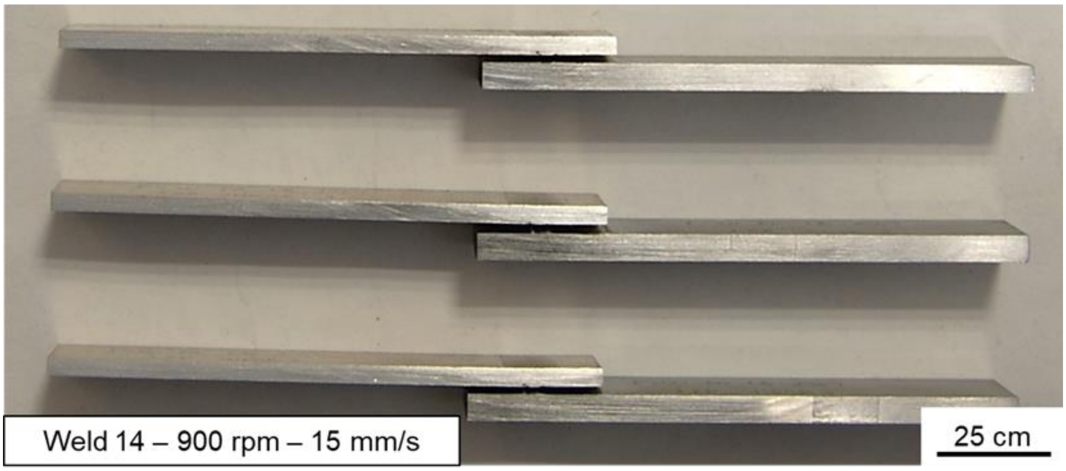
Weld 14 – 900 rpm – 15 mm/s
25 cm